2012

Numerical Simulation Of Conventional Fuels And Biofuels Dispersion And Vaporization Process In Co-flow And Cross-flow Premixers

Xin Gu
University of Central Florida

NUMERICAL SIMULATION OF CONVENTIONAL FUELS AND BIOFUELS DISPERSION AND VAPORIZATION PROCESS IN CO-FLOW AND CROSS-FLOW PREMIXERS

by

XIN GU
B.S. China Agricultural University, 2006
M.S. University of Central Florida, 2009

A dissertation submitted in partial fulfillment of the requirements
for the degree of Doctor of Philosophy
in the Department of Mechanical, Materials and Aerospace Engineering
in the College of Engineering and Computer Science
at the University of Central Florida
Orlando, Florida

Spring Term
2012

Major Professor: Ranganathan Kumar

ABSTRACT

In order to follow increasingly strict regulation of pollutant emissions, a new concept of Lean Premixed pre-vaporized (LPP) combustion has been proposed for turbines. In LPP combustion, controlled atomization, dispersion and vaporization of different types of liquid fuel in the pre-mixer are the key factors required to stabilize the combustion process and improve the efficiency.

A numerical study is conducted for the fundamental understanding of the liquid fuel dispersion and vaporization process in pre-mixers using both cross-flow and co-flow injection methods. First, the vaporization model is validated by comparing the numerical data to existing experiments of single droplet vaporization under both low and high convective air temperatures. Next, the dispersion and vaporization process for biofuels and conventional fuels injected transversely into a typical simplified version of rectangular pre-mixer are simulated and results are analyzed with respect to vaporization performance, degree of mixedness and homogeneity. Finally, collision model has been incorporated to predict more realistic vaporization performance.

Four fuels, Ethanol, Rapeseed Methyl Esters (RME), gasoline and jet-A have been investigated. For mono-disperse spray with no collision model, the droplet diameter reduction and surface temperature rise were found to be strongly dependent on the fuel properties. The diameter histogram near the pre-mixer exit showed a wide droplet diameter distribution for all the fuels. In general, pre-heating of the fuels before injection improved the vaporization performance. An improvement in the drag model with Stefan flow correction showed that a low speed injection and high cone angle improved performance. All fuels achieved complete vaporization under a

spray cone angle of 140°. In general, it was found that cross-flow injection achieved better vaporization performance than co-flow injection. A correlation is derived for jet-A's total vaporization performance as a function of non-dimensional inlet air temperature and fuel/air momentum flux ratio. This is achieved by curve-fitting the simulated results for a broad range of inlet air temperatures and fuel/air momentum flux ratios.

The collision model, based on no-time-counter method (NTC) proposed by Schmidt and Rutland, was implemented to replace O'Rourke's collision algorithm to improve the results such that the unphysical numerical artifact in a Cartesian grid was removed and the results were found to be grid-independent. The dispersion and vaporization processes for liquid fuel sprays were simulated in a cylindrical pre-mixer using co-flow injection method. Results for jet-A and Rapeseed Methyl Esters (RME) showed acceptable grid independence. At relatively low spray cone angle and injection velocity, it was found that the collision effect on the average droplet size and the vaporization performance were very high due to relatively high coalescence rate induced by droplet collisions. It was also found that the vaporization performance and the level of homogeneity of fuel-air mixture could be significantly improved when the dispersion level is high, which can be achieved by increasing the spray cone angle and injection velocity. In order to compare the performance between co-flow and cross-flow injection methods, the fuels were injected at an angle of 40° with respect to the stream wise direction to avoid impacting on the wall. The cross-flow injection achieved similar vaporization performance as co-flow because a higher coalescence rate induced by droplet collisions cancelled off its higher heat transfer efficiency between two phases for cross-flow injections.

ACKNOWLEDGEMENTS

First, I would like to express my sincere gratitude to my advisor, Dr. Ranganathan Kumar, for his tremendous support during my entire PhD career in the last six years. Without his continuous encouragement and guidance on my research, it would not be possible for me to finish my PhD work. He was always there for me when I was stuck in research and got frustrated, so I really appreciate his care from the bottom of my heart. He is such a great mentor to me, and every aspect I have learned from him will help me and is helping me to build up my career.

I would like to thank Dr. Saptarshi Basu, Dr. Louis Chow, Dr. Jayanta Kapat and Dr. Bhimsen Shivamoggi for serving as my Thesis Committee members and providing valuable comments and suggestions for my research. I want to express special thanks to Dr. Saptarshi Basu for last couple of years since he has provided a great deal of guidance and suggestions on my research.

I would like to thank my previous labmate, Xuan Wu, Amit Gupta, Parveen Sachdeva, Navid Aminimanash, Ehsan Yakhshi-Tafti, Luis Zea, Josh Lee, Abhishek Saha and Erick Tijerino. I learned a lot from each of them and they all have been great colleagues and friends as I walk through the PhD road.

I would also like to express my sincere gratitude to my current employer, Exa Corporation, a leading edge CFD company, who has provided me this great opportunity to start my professional career. I want to express special thanks to my manager, Dr. Yong Zhou, and company chief

scientist Dr. Hudong Chen, who has given me a lot of support and encouragement during last year when I was working full-time at Exa and working similar amount of time on my research.

Last, I would like to thank my parents, my father Xingzhi Gu, my mother Fengju Guo, for their endless love and support during my whole life. I would also like to thank my beloved fiancée, Suli Ni, who has always been there with me in the last five years. Their love is the source of my passion, so I would like to dedicate this dissertation to both of my parents and my Suli.

TABLE OF CONTENTS

LIST OF FIGURES

LIST OF TABLES

LIST OF ABBREVIATIONS

a_d	droplet acceleration
B_d	Global Spalding mass transfer number
C_D	Droplet drag coefficient
c_{pg}	Specific heat of gas phase
c_{pl}	Specific heat of liquid phase
$D_{g,i}$	Vapor mass diffusivity of 'i'th species into gas phase
D_l	Liquid mass diffusivity within the droplet
g	gravitational acceleration
$h_{l,i}$	Specific enthalpy of species i in the liquid phase
k_g	thermal conductivity of gas phase
k_{gs}	thermal conductivity of gas phase at the droplet surface
k_l	thermal conductivity of liquid phase
L_i	Latent heat of vaporization of species i
m_d	Droplet mass
$\dot{m}_d$	Droplet vaporization rate
M_{coll}	Number of collisions
M_{cand}	Number of candidate collision pairs
MW_v	Molecular weight of fuel vapor
np	number of parcels
Nu_g	Nusselt number for gas phase
Pr_g	Prandtl Number for gas phase
P_{atm}	Atmosphere pressure on which the fuel boiling temperature is based

P_g Pressure of surrounding gas phase

$P_{gs,i}$ Partial pressure of fuel species i at droplet surface

$P_{sat,i}$ Saturation pressure of fuel species i

qFa Fuel/air momentum flux ratio

r_d Instantaneous droplet radius

Re_d Reynolds number of the droplet exposed to external gas flow

$Sh_{g,i}$ Sherwood number for species i

$Sc_{g,i}$ Schmidt number for species i

$\underline{t}$ Time

$\hat{T}$ Film temperature

T_s Droplet surface temperature

T_g Gas phase temperature

$\mathbf{u}$ Mean gas phase velocity

$\mathbf{u'}$ Turbulent gas phase velocity

$\mathbf{u_d}$ Droplet velocity

$\mathbf{u_F}$ Fuel injection velocity

v_{ls} Liquid velocity at the droplet surface

V_{pj} Volume of droplet 'j'

A_{pj} Surface area of droplet 'j'

$X_{gs,i}$ Vapor mole fraction of species i at droplet surface

$X_{ls,i}$ Liquid mole fraction of species i at droplet surface

$Y_{gs,i}$ Vapor mass fraction of species i at droplet surface

$Y_{ls,i}$ Liquid mass fraction of species i at droplet surface

$Y_{l,i}$ Liquid mass fraction of species i within the droplet

Z	Distance between the centers of two colliding droplets in the direction of their relative velocity
μ_g	Dynamic viscosity of gas phase
ρ_g	Density of the gas phase
ρ_{gs}	Density of the gas phase at the droplet surface
ρ_l	Density of the liquid phase
ρ_{ls}	Density of the liquid phase at the droplet surface

CHAPTER ONE: INTRODUCTION

1.1 Background and Motivation of this Study

One of the biggest crises the world is facing nowadays is the exhaust of the main energy source, fossil fuels. This energy crisis has made the development of alternative energies the top priority. Solar, wind, biomass and geothermal are the most promising alternative sources of energies. In automotive, aero-propulsion and power generation industries, fuels extracted from biomass have gained great attractions to serve as alternative fuels due to their renewable and environmental-friendly nature since they can be obtained from biomass, such as ethanol from corn grain and biodiesel from soybeans. Biomass produced energy has no net CO_2 contribution to the atmosphere since the CO_2 released during the combustion process is captured during biomass growth. According to a research conducted by Hill et al. (2006):

> *Ethanol yields 25% more energy than the energy invested in its production, whereas biodiesel yields 93% more. Compared with ethanol, biodiesel releases just 1.0%, 8.3%, and 13% of the agricultural nitrogen, phosphorus, and pesticide pollutants, respectively, per net energy gain. Relative to the fossil fuels they displace, greenhouse gas emissions are reduced 12% by the production and combustion of ethanol and 41% by biodiesel.*

Bio alcohol (ethanol) and its blends with gasoline have been tested and used as alternative fuels of gasoline IC engines, while biodiesel (Methyl esters of rapeseed oils or soybean oils) and its blends with diesel fuel and jet fuels have been tested in diesel IC engines and jet engines, respectively. Despite the strong dispersion of the published results, there has been proof that their use is a promising solution to the problems originated with the raw vegetable oil due to their higher viscosity, boiling temperature, final temperature of distillation and point of obstruction of cold filter [Tinaut (2005)].

In power generation and aero-propulsion industry, a lot of companies have started to use "drop-in" approach to replace the fossil oil derivative fuels, meaning the biofuels are blended with the traditional fuels and the percentage of the biofuels in the blends will increase step by step.

For most of traditional gas turbines that operate on liquid fuels, including conventional fuels such as gasoline and kerosene, and also renewable fuels such as ethanol and biodiesel, spray diffusion burners are employed. However, the diffusion mode of combustion tends to generate unacceptable contaminates, such as NO_x and particulate matter. The current technology of reducing the NO_x emission is to use the water/stream injection to the burner, since water/stream has a dilution and cooling effects, the temperature in the reaction zone will be lowered and hence reduce the NO_x emission. However, the use of water/stream injection may increase CO emission due to the local quenching effects [Ramotowski et al. (2008)]. Figure 1 shows the level of emission of CO and NO_x as a function of the primary temperature reached in the reaction zone of the combustor [Bellofiore (2006)].

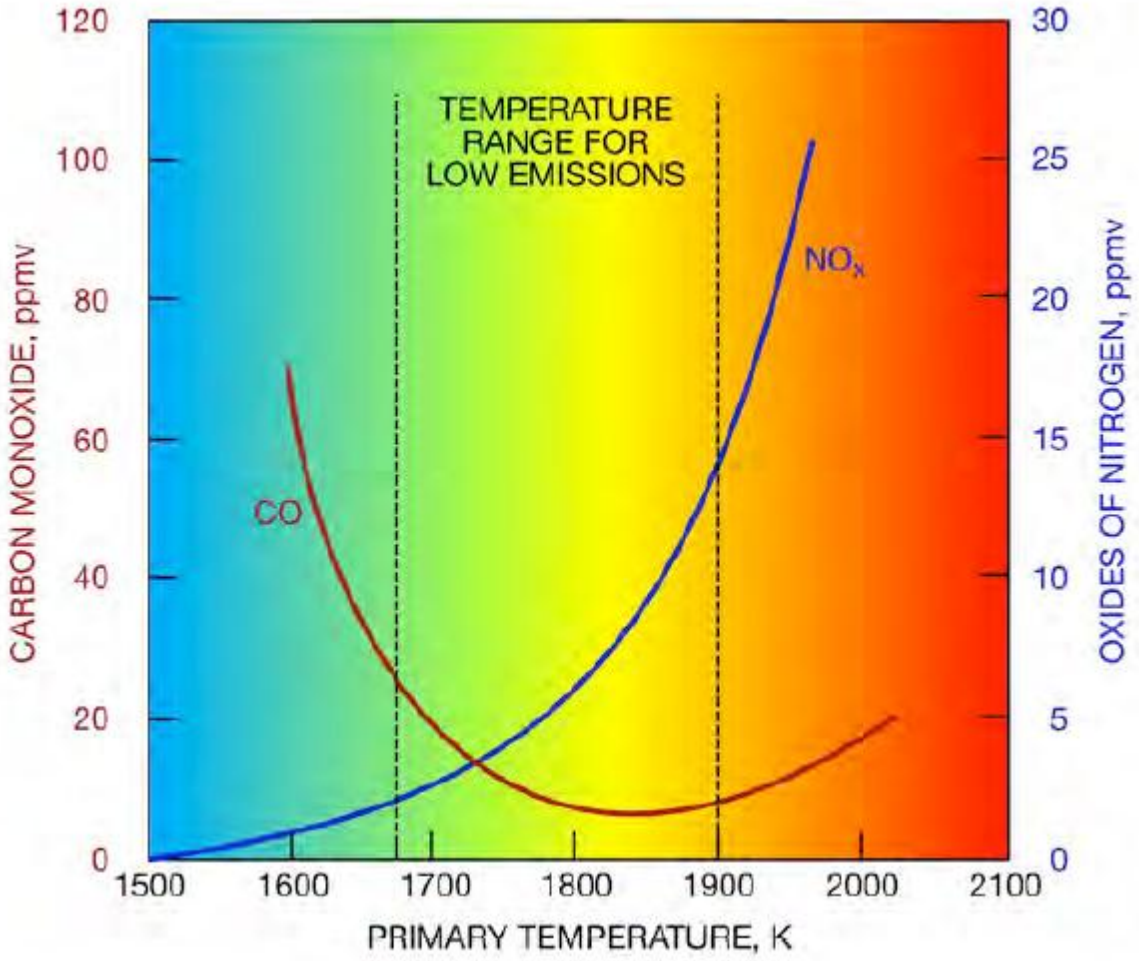

Figure 1: Level of emission of CO and NOx as a function of the primary temperature reached in the reaction zone of the combustor [From Lefebvre (1995)]

As a recent technology, the Lean Premixed and Prevaporized gas turbine is very promising to achieve high efficiency combustion and low NO_x emissions. There are two main features of this technology:

First, "Lean" means by using large amount of air, the high flame temperature in the reaction zone is avoided, hence resulting in the reduction of NO_x. Second, the efficient and stable premixing system is capable of dispersing, evaporating, and mixing the liquid fuel into the high temperature

air-flow in small time and space scale. Thus, the well premixed fuel and air will lead to a higher combustion efficiency. Figure 2 shows the difference between the diffusion combustion flame and the premixed combustion flame.

Figure 2: Liquid fuel spray diffusion flame and typical lean, premixed natural gas flame [From Ramotowski et al. (2008)]

Due to the different properties between biofuels and conventional fuels, such as density, viscosity, surface tension, and vaporization pressure under different temperature, the subsequent biofuel liquid atomization and vaporization characteristics will be different compared to conventional fuels. This will lead to different design of the premixing duct, such as the duct length and different spray control, such as spray velocity and spray angles. The most important of the premixing system design is to satisfy the highest possible effectiveness and reliability. A common technique is to use cross-flow injection, which incorporates one or more plain orifice nozzles that are used to inject liquid fuels perpendicularly into the high temperature and high pressure air flow coming from the compressor.

1.2 Objectives and Approaches

The main objective of this thesis will be the study of both conventional fuels and biofuels dispersion and vaporization process in a pre-vaporization chamber-pre-mixer, which is a scaled down and simplified version of a LPP gas turbine. Different characteristics of biofuel sprays will be compared with the conventional fuels, such as gasoline and Jet-A. The two main biofuels that will be studied in this thesis are ethanol and Rapeseed ethyl esters (RME). The latter is a type of biodiesel which can be blended into diesel fuels and jet fuels.

A two-phase flow solver, KIVA, will be used as the numerical tool to conduct the liquid fuel spray simulations. KIVA is a computer program invented by Amsden et al. (1985) from Los Alamos National Laboratory (LANL), and it can be used to solve transient, three dimensional, chemically reacting fluid flows with sprays.

The latest version of this computer program is KIVA-4, which will be used with some modification in conducting the simulation studies for the thesis. Detailed information of KIVA-4 and its relevant physical sub-models for sprays will be discussed in Chapter 3.

CHAPTER TWO: LITERATURE REVIEW

The use of lean premixed and pre-vaporized liquid fuels to achieve more efficient, less pollutant gas turbines in both aero-propulsion and power generation industry are very promising. Obviously, the premixing design of air-fuel mixture is the key task in the developments of such technology. In this chapter, an overview of the numerical and experimental works in the area of liquid atomization and its sub-processes is presented.

2.1 Analytical Models of Liquid Disintegration

When a continuous liquid jet is injected from a nozzle into the air, the liquid jet becomes very unstable and will breakup into ligaments and eventually into droplets. Probably the earliest significant work is proposed by Rayleigh (1878) in his study of stability analysis for an infinitely long, inviscid column of liquid without the aerodynamic effects. He proposed that the jet breakup is due to the capillary-based instability. The wave growth rate in his analysis is given as:

$$\omega^2 = \frac{\sigma}{\rho_l a^3} \frac{(1-k^2a^2)kaI_1(ka)}{I_0(ka)} \tag{2.1}$$

where a is nozzle orifice radius, k is wavenumber, and $I_1(ka)$, $I_0(ka)$ are modified Bessel functions of the first kind.

Weber (1931) extended Rayleigh's analysis and showed that by including the effect of the liquid viscosity, the breakup rate decreases and the drop size increases. Later, Sterling and Sleicher (1975) extended Rayleigh and Weber's analysis by including the aerodynamic forces on the

liquid surface. Reitz and Bracco (1982) proposed a general dispersion equation for an axisymmetric liquid jet:

$$\omega^2 + 2\nu k^2 \omega \left[\frac{I_1'(\xi)}{I_0(\xi)} - \frac{2kl}{k^2+l^2} \frac{I_1(\xi)}{I_0(\xi)} \frac{I_1'(la)}{I_0(la)} \right] = \frac{\sigma_1 k}{\rho_l a^2}(1-\xi^2)\left(\frac{l^2-k^2}{l^2+k^2}\right)\frac{I_1(\xi)}{I_0(\xi)} + \frac{\rho_g}{\rho_l}\left(U - \frac{i\omega}{k}\right)^2 k^2 \left(\frac{l^2-k^2}{l^2+k^2}\right)\frac{I_1(\xi)}{I_0(\xi)}\frac{K_0(\xi)}{K_1(\xi)} \tag{2.2}$$

where $\xi = ka$, $\nu = \frac{\mu}{\rho_l}$, $l^2 = k^2 + \frac{\omega}{\nu}$

The above Reitz-Bracco equation will recover Rayleigh's result in the absence of viscosity and the gas phase.

2.2 Numerical Modeling of Atomization

2.2.1 Atomization Regime

For both co-flow and crossflow spray injections, they can be divided into three main regimes: 1. Primary breakup regime, where the bulk liquid jet coming from the nozzle meets high speed air, the bulk liquid jet will breakup into pieces of elongated ligaments, and further form relatively large droplets; 2. Secondary breakup regime, where the large droplets breakup into smaller droplets; 3. Vaporization regime, where those atomized small droplets evaporate, diffuse and become mixed with the air stream. Figure 3 shows a schematic of a cross-flow spray by Brinckman et al. (2008).

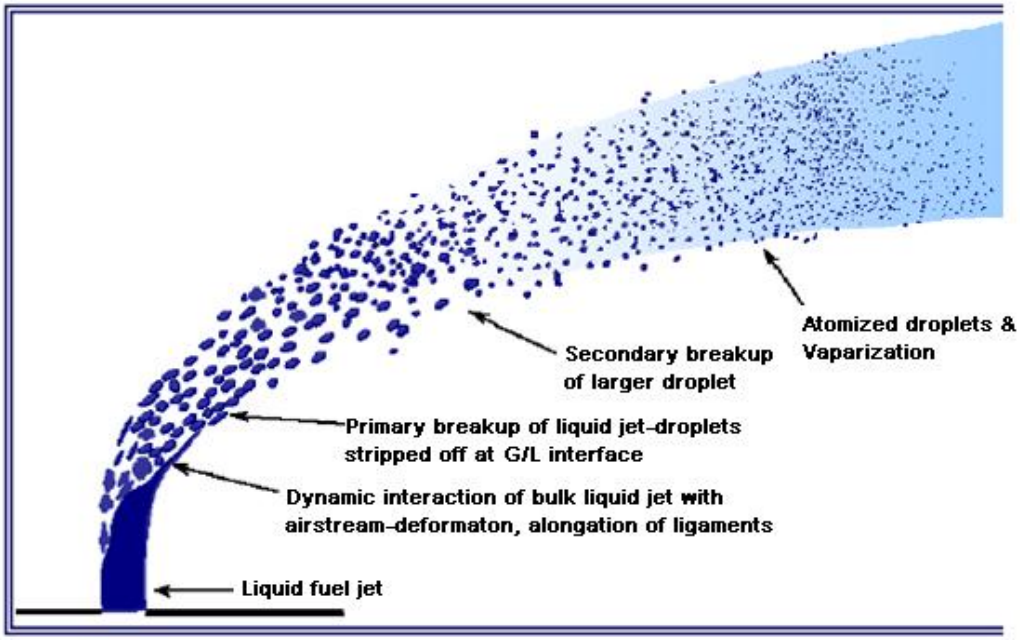

Figure 3: Schematic of liquid jet breakup and vaporization in a gas cross-flow before combustion [From Brinckman et al. (2008)]

2.2.2 DNS Modeling of Atomization

The atomization process is an extremely complicated two-phase flow problem, for example, when the relative velocity between liquid phase and gas phase reaches the order of hundreds of meters per second, droplets with size of a few microns may be produced. Thus, the computational expense to resolve such droplets during the atomizing spray process under the whole domain is very high. Therefore, the Direct Numerical Simulation (DNS) to resolve all time and length scales of atomization is very difficult and nearly impossible even using the stat-of-art supercomputers.

Among the various two-phase flow DNS methods, two principle methods: volume of fluid (VOF) method invented by Hirt & Nichols (1981) and level-set method invented by Sussman et al. (1994) have been widely used and applied to simulate the primary atomization process. These methods have been conducted by several researchers: De Villiers et al. (2004) and Bianchi et al. (2007) employed the VOF concept method, Desjardins et al. (2008) employed a conservative level-set/ghost fluid method, Menard et al. (2007) employed a coupled Level Set/VOF/Ghost Fluid method, and Lebas et al. (2008) employed a so-called ELSA (Eulerian-Lagrangian Spray Atomization Model). A recent review on the current state-of-art modeling of primary atomization was done by Gorokhovski and Herrmann (2008).

To illustrate the difficulty of solving such a complex two-phase systems using a DNS method, Figure 4, a VOF simulation, shows that a single droplet distorts and breaks up under a highly turbulent flow. The gaseous nitrogen enters the domain with a speed of 50 m/s and a droplet with a diameter of 100 microns is placed in the computational domain near the velocity inlet. The Weber number of this simulation is about 347, which means the drop will break up very rapidly. By using a grid of approximate 4 million cells, each of which has a size of 1.5 microns required 81 hours on 8 CPUs with parallel computations [Strakey and Talley (2004)]. As it can be seen, to resolve a single droplet requires such expensive computational resources, thus it is not difficult to imagine the efforts needed in order to fully resolve complex spray systems where millions of droplets are present. However, there are no needs to resolve all time and length scales for such complex systems, where our main interest is its overall large scale characteristics, such as overall droplet size distributions and total vaporization performance.

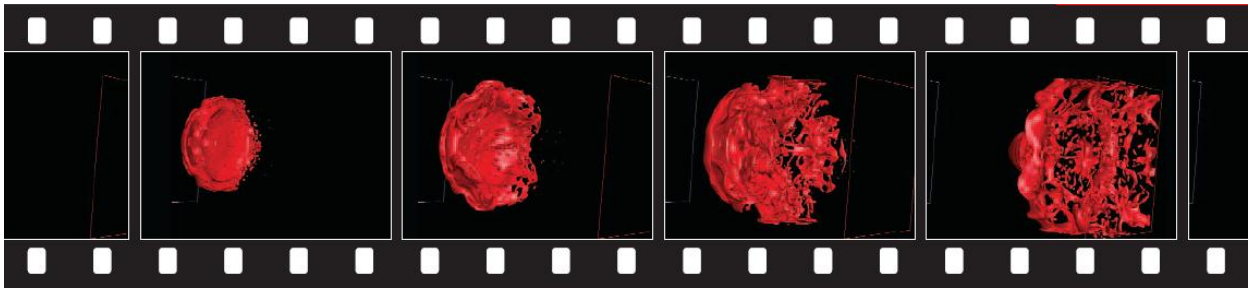

Figure 4: A transient simulation of water droplet breakup with a time between frames of 1.5 micro seconds [From Strakey and Talley (2004)]

2.2.3 Lagrangian Spray and Atomization Modeling

Above DNS methods are among the category of Eulerian methods since they treat the liquid as another continuous phase, however, those methods require extensive CPU resources to track the transient liquid-gas interface. There is another category, called Lagrangian spray and atomization models, and they have been most widely used for more than two decades. In engine spray simulations, such as IC engines and LPP gas turbines, Lagrangian concept of tracking the liquid phase appear to be a natural choice since the liquid fuel only possess a small volume of the domain compared to the gas phase. Under Lagrangian framework of atomization modeling, liquid phase is treated as a discrete second phase. Most of the methods in this category are based on instability theories and analyses, such as the Kelvin-Helmholtz (KH) and Rayleigh-Taylor instability analyses [Reitz and Diwakar (1987), Patterson and Reitz (1998)].

A “Blob” concept of spray was introduced by Reitz and Diwakar (1987) in their diesel spray simulation. In their model, the continuous jet was discretized into a series of “Blobs”, or named parcels. Each parcel consists of a certain number of droplets with same characteristics, such as

diameter, temperature and velocity. The initial diameter of the drop is normally assumed to be equal to the nozzle orifice diameter, and then the droplets interactions and aerodynamic breakup are calculated based on some experimental correlations. The concept of parcel efficiently reduces the computational cost of the spray simulation. For example, if you have N droplets in your computational domain, the number of possible collision pairs is approximately $0.5N^2$. By tracking parcels, each of which represents 100 droplets, the cost of collision calculation will be reduced by a factor of 10^4.

Reitz (1987) further proposed a blob breakup model, in which new drops with radius r are formed from a parent drop with radius *a* when breakup happens:

$$r = B_0\Lambda, \quad for\ B_0\Lambda \le a \tag{2.3a}$$

$$r = \min\left\{\left(\frac{3\pi a^2 U}{2\Omega}\right)^{0.33}, \left(\frac{3a^2\Lambda}{4}\right)^{0.33}\right\}, \quad for\ B_0\Lambda > a \tag{2.3b}$$

where Λ and Ω are the wavelength and wave growth rate. Due to mass loss during the breakup, the radius change rate of parent drop can be expressed as:

$$da/dt = -(a-r)/\tau, \quad r \le a \tag{2.4}$$

where τ is the breakup time, with

$$\tau = \frac{3.726 B_1 a}{\Omega\Lambda} \tag{2.5}$$

where constant B_1 has been given different values depending on the injector characterization, such as $B_1 = 20$ by Reitz (1987), $B_1 = 1.73$ by Liu et al. (1993).

Another widely used droplet breakup model is the Taylor Analogy Breakup (TAB) model by O'Rourke and Amsden (1987). Their method is based on Taylor's analogy (1963) between an oscillating and distorting droplet and a spring mass system. The restoring force of the spring is analogous to the surface tension force of a droplet, the external force on the mass is analogous to the aerodynamic force, and the damping force is analogous to the droplet viscous force. When the dimensionless distortion exceeds unity, the parent droplets will break up into a distribution of child droplets. The limitation of this method is determined by the Weber number, which is defined:

$$We_c = \frac{\rho U_{rel}^2 \overline{D}}{\sigma} \tag{2.6}$$

where U_{rel} is the relative velocity between two parcels, and $\overline{D}$ is the arithmetic mean diameter of the two colliding parcels. The TAB method is appropriate for low Weber number sprays, and a critical value is about 100.

The blob concept of Lagrangian spray method has been successfully used in the crossflow atomization simulations by several researchers [Rachner et al. (2002); Madabhushi (2003); Khosla and Crocker (2004); Barata (2007)]. The Lagrangian spray and atomization approach was implemented in the KIVA program. More detailed information and review on this approach will be discussed in Chapter 3.

2.3 Experimental Investigations of Spray Atomization Process

The process of jet disintegration has been experimentally studied for more than 100 years. Savart (1833) supplied the first quantitative data related to jet disintegration. He found that if the jet diameter is constant, then the continuous liquid jet length is proportional to the jet velocity; or if the jet velocity is constant, the length of the continuous liquid jet is proportional to its diameter. Some early significant investigations on the jet breakup process were done by Rayleigh (1878), Weber (1931), Tyler (1933), and Ohnesorge (1936). Many researchers have shown that the spray characteristics are influenced by a lot of parameters, such as the injection nozzle internal flow physics, injection velocity, physical and thermodynamic states of both liquid and gas phases (Reitz and Bracco (1986)). In this section, emphasis is focused on the experimental investigation of liquid/spray jet injection into a crossflow and the subsequent jet breakup/atomization process.

The first work of liquid jet injection into a crossflow was done by Chelko (1950), during his investigation of the behavior of a water jet injected into a high velocity airstream. He focused on what he called the penetration of the jets, which refer to a curve line, roughly describing the trajectory of the liquid jet. With the advanced optical device applied in the experiments, accurate droplets size and distribution data become available. Quantitative droplet flow field is usually measured by Particle Image Velocimetry (PIV) arrangement, based on a laser sheet double pulse illumination. Laser Doppler-Phase Doppler Anemometry (LD-PDA) system is usually used to provide the information of droplet size distribution. Rachner et al. (2002) utilized Phase Doppler Anemometry and a time-resolved shadowgraph technique with Mie-scattering laser light sheet to gain quantitative information regarding jet penetration, fuel displacement and droplet size distribution in a study of kerosene spray in a crossflow air stream under high pressure and

ambient temperature. Cavaliere et al. (2003) used a tomographic visualization technique to capture the spray morphology. They also employed a shadowgraphic technique to obtain the water jet trajectories in crossflow premixing duct under various crossflow velocities and jet injection velocities. Sedarsky et al. (2010) used PIV, high-speed shadowgraphy (HSS) and ballistic imaging to observe the breakup of a liquid jet in a crossflow of air under a variety of conditions.

Near nozzle region of liquid atomization has not been well understood because the near field is surrounded by a dense fog of droplets, which envelop the continuous jet in the near nozzle region. This makes it extremely difficult to acquire and interpret spray structures quantitatively in dense spray region using conventional techniques with visible light or lasers. The recently developed experimental techniques such as X-ray and ballistic imaging have provided new insights into spray structures. Powell et al. (2001) at Argonne National Laboratory, used X-ray absorption techniques to make quantitative, time-resolved measurements in the near nozzle region. Linne et al. (2005) used a time-gated ballistic imaging instrument to obtain high spatial resolution, single-shot images of the liquid core in a water spray issuing into a gaseous crossflow under different Weber numbers. Their advanced high-resolution results reveal a new-nozzle spray structures such as droplets, voids, and ligaments. Since the ballistic imaging instrument is a fairly new technique, more details are needed. The review of this technique are provided by Linne et al. (2009).

A very detailed and recent review on the special topic of the liquid jet injection into a gaseous crossflow was provided by Bellofiore (2006) in his Ph.D. thesis. In his study, water and Jet-A were used as the injection liquid in a crossflow premixing duct under real LPP gas turbine operating conditions, which means the pressure of the crossflow air is up to 2MPa, and temperature is up to 600 Kelvin. He also employed a shadowgraphic technique to analyze the jet spray trajectories, while using PIV and PDA systems to detect the droplet velocity field and spatial size distributions.

All the works discussed above are about the continuous liquid jet injecting into a crossflow air, which plays a major role as the liquid atomizing force. Only a few works in the existing literature have employed an atomizer before the liquid is injected into the crossflow, meaning the liquid is already atomized into droplets and then those droplets are sprayed into the crossflow. Chin et al. (1986) studied the evaporation history of a spray of droplets injected into a crossflow. The authors developed a code to predict the volume fraction of vaporized fuel as a function of downstream distance. Flat-fan sprays were employed under an experimental study that was conducted on sprays into a crossflow (Phillips and Miller, 1999; Phillips et al., 2000). In their experimental studies, the spray field was characterized in terms of its volumetric flux, its droplet size, and velocity characteristics. Whereas Phillips and Miller (1999) investigated the flow field of a single flat-fan spray injected into a crossflow. Phillips et al. (2000), studied the effect of an overlapping series of flat-fan sprays on the flow of the droplets and air. In the Phillips et al. (2000) study, a bubble tracing method was used to visualize the crossflow interaction with the spray. Results showed that the crossflow air could not penetrate the spray under a weak

crossflow velocity of 0.75 m/sec, but did penetrate the spray at moderate crossflow velocities of 3.0 m/sec. It should be noted that the crossflow velocities encountered in gas turbine spray applications are typically one to two orders of magnitude higher than these velocities. Leong et al. (2000) employed an air-blast atomizer to spray the droplets into a crossflow air at elevated pressure. Their experimental test matrix was designed to fall within the range of practical operating conditions of the aircraft engines, and Jet-A was used since it is fuel for the aircraft engines. They used Phase Doppler Interferometry (PDI) to measure the scattering of lights by particles passing through a probe volume in order to calculate their size and velocities. In a recent study by Bai et al. (2009), they used a PIV system and an image-processing technique to investigate centrifugal sprays injected into a gas crossflow at various angles under ambient pressure and temperature. Their investigated gas Reynolds number vary from 12900 to 45000, and three injection angle were used.

CHAPTER THREE: METHODOLOGY

KIVA-4 program is capable of solving transient, turbulent, two-phase chemically reacting flow in both subsonic and supersonic range. In this chapter, the governing equations for gas-phase, liquid sprays and vaporization model will be introduced. Next, the structure of KIVA-4 program, mesh generation, boundary condition and important input parameters will be presented.

3.1 The Governing Equations

3.1.1 The Continuous Phase

There could be several species in the gas phase since KIVA is capable of solving the species transport equation. The continuity equation for species m is:

$$\frac{\partial \rho_m}{\partial t} + \nabla \cdot (\rho_m \mathbf{u}) = \nabla \cdot \left[\rho D \nabla (\frac{\rho_m}{\rho}) \right] + \dot{\rho}_m^c + \dot{\rho}^s \delta_{ml} \tag{3.1}$$

where ρ_m is the density of species m, ρ is the total density, and $\mathbf{u}$ is the velocity. Single species diffusion coefficient D is assumed with Fick's diffusion law. $\dot{\rho}_m^c$ is the source term due to chemical reaction, $\dot{\rho}^s$ is the source term due to the spray, and δ is the Dirac Delta function. Summing up Equation 3.1 over all species, the total fluid density equation becomes:

$$\frac{\partial \rho}{\partial t} + \nabla \cdot (\rho \mathbf{u}) = \dot{\rho}^s \tag{3.2}$$

The momentum equation for the fluid mixture is:

$$\frac{\partial (\rho \mathbf{u})}{\partial t} + \nabla \cdot (\rho \mathbf{u}\mathbf{u}) = -\frac{1}{a^2} \nabla p - A_0 \nabla (\frac{2}{3} \rho k) + \nabla \cdot \boldsymbol{\sigma} + \mathbf{F}^s + \rho \mathbf{g} \tag{3.3}$$

where p is the pressure, a is the dimensionless quantity used in conjunction with the Pressure Gradient Scaling (PGS) method [Ramshaw et al. (1985)]. PGS method is used to enhance computational efficiency in low Mach number flows where the pressure is nearly uniform. If the PGS method is used, a will vary with time, otherwise, a=1. The constant A_0 is zero in laminar flows and unity for turbulent flows. $\mathbf{F}^s$ is the rate of momentum gain due to the spray. The viscous stress tensor is in Newtonian form:

$$\boldsymbol{\sigma} = \mu\left[\nabla\mathbf{u} + (\nabla\mathbf{u})^T\right] + \lambda\nabla\cdot\mathbf{u}\mathbf{I} \tag{3.4}$$

The internal energy equation is:

$$\frac{\partial(\rho I)}{\partial t} + \nabla\cdot(\rho\mathbf{u}I) = -p\nabla\cdot\mathbf{u} + (1-A_0)\boldsymbol{\sigma}:\nabla\mathbf{u} - \nabla\cdot\mathbf{J} + A_0\rho\varepsilon + \dot{Q}^c + \dot{Q}^s \tag{3.5}$$

where $\underline{I}$ is the specific internal energy, $\mathbf{J}$ is the heat flux vector due to heat conduction and enthalpy diffusion:

$$\mathbf{J} = -K\nabla T - pD\sum_m h_m\nabla(\rho_m/\rho) \tag{3.6}$$

where T is the temperature and h_m is the specific enthalpy for species m.

When one of the turbulent models are in use, two additional transport equations are solved for the turbulent kinetic energy k and its dissipation rate ε:

$$\frac{\partial(\rho k)}{\partial t} + \nabla\cdot(\rho\mathbf{u}k) = -\frac{2}{3}\rho k\nabla\cdot\mathbf{u} + \boldsymbol{\sigma}:\nabla\mathbf{u} + \nabla\cdot\left[\left(\frac{\mu}{\mathrm{Pr}_k}\right)\nabla k\right] - \rho\varepsilon + \dot{W}^s \tag{3.7}$$

$$\frac{\partial(\rho\varepsilon)}{\partial t} + \nabla\cdot(\rho\mathbf{u}\varepsilon) = -\left(\frac{2}{3}c_{\varepsilon 1} - c_{\varepsilon 3}\right)\rho\varepsilon\nabla\cdot\mathbf{u} + \nabla\cdot\left[\left(\frac{\mu}{\mathrm{Pr}_k}\right)\nabla\varepsilon\right] + \frac{\varepsilon}{k}\left[c_{\varepsilon 1}\boldsymbol{\sigma}:\nabla\mathbf{u} - c_{\varepsilon 1}\rho\varepsilon + c_s\dot{W}^s\right] \tag{3.8}$$

These are standard k - ε equations with some extra terms. Source term $(c_{\varepsilon 3} - 2/3c_{\varepsilon 1})\nabla \cdot \mathbf{u}$ accounts for length scale change when there is a velocity dilatation, $\dot{W}^s$ arises due to the spray. The transport coefficients in above equations are:

$$\begin{aligned} \mu &= (1.0 - A_0)\rho\upsilon_0 + \mu_a + \frac{A_0 c_\mu \rho k^2}{\varepsilon} \\ \lambda &= -\frac{2}{3}\mu \\ K &= \frac{\mu c_p}{\mathrm{Pr}} \\ D &= \frac{\mu}{\rho Sc} \end{aligned} \tag{3.9}$$

Since the current Lagrangian-Eulerian approach used two-way coupling between the discrete droplet phase and continuous gas phase it is important to introduce the source terms contributed to the gas phase from the spray. They are comprised of two parts: inter-phase transport and evaporation of droplet phase. The spray source terms for mass, momentum and energy equations of the continuous gas phase are:

$$\dot{\rho}^s = -\int f \rho_l 4\pi r_d^2 \dot{r}_d du_d dr dT_d dy d\dot{y} \tag{3.10}$$

$$\mathbf{F}^s = -\int f \rho_l \left[\frac{4}{3}\pi r_d^3 (\mathbf{a_d} - \mathbf{g}) + 4\pi r_d^2 \dot{r}_d \mathbf{u} \right] du_d dr dT_d dy d\dot{y} \tag{3.11}$$

$$\dot{Q}^s = -\int f \rho_l \left\{ \frac{4}{3}\pi r_d^3 \left[(\mathbf{a_d} - \mathbf{g}) \cdot (\mathbf{u}_d - \mathbf{u} - \mathbf{u}') + \dot{h}_d \right] + 4\pi r_d^2 \dot{r}_d (I_d + \frac{1}{2}|\mathbf{u}_d - \mathbf{u}|^2) \right\} du_d dr dT_d dy d\dot{y} \tag{3.12}$$

where f is the droplet probability distribution function (PDF), which is function of droplet position, r, velocity, u_d, droplet temperature, T_d, droplet distortion from sphericity, y, and the distortion rate, $\dot{y}$.

3.1.2 The Liquid Phase

In order to calculate the mass, momentum and energy exchange between the spraying phase and the gas phase, the distribution of drop sizes, velocities, and temperatures must be accounted for. In numerous real spray situations where the droplet Weber number is high, droplet oscillations, distortions, and breakup must be considered. Droplet collisions and coalescences were also found to be important in many sprays (O'Rourke (1981); Bracco (1985)). A mathematical formulation of sprays to describe those complex physical processes was given by Williams (1985). In his formulation, the droplet probability distribution function, f, was defined with ten independent variables in addition to time: three components of droplet displacement $\vec{\mathbf{x}}$, three velocity components $\vec{\mathbf{v}}$, equilibrium radius, temperature T_d, distortion from sphericity y, and the time rate of change $dy/dt = \dot{y}$. Droplets break up only if $y > 1.0$ (O'Rourke and Amsden (1987)).

The time evolution of f is obtained by solving the spray equation:

$$\frac{\partial f}{\partial t} + \nabla_{\mathbf{x}} \cdot (f\mathbf{v}) + \nabla_{\mathbf{v}} \cdot (f\mathbf{F}) + \frac{\partial}{\partial r}(fR) + \frac{\partial}{\partial T_d}(f\dot{T}_d) + \frac{\partial}{\partial y}(f\dot{y}) + \frac{\partial}{\partial \dot{y}}(f\ddot{y}) = \dot{f}_{coll} + \dot{f}_{br} \qquad (3.10)$$

where $\mathbf{F}$, R, $\dot{T}_d$ and $\ddot{y}$ are the time rate of change of velocity, radius, temperature and oscillation velocity $\dot{y}$ of an individual droplet, respectively. The term $\dot{f}_{coll}$ and $\dot{f}_{br}$ are source terms due to droplet collisions and breakups. The detailed mathematical formulation of collision, breakup sources terms, collision outcome criteria, post-collision calculation, droplet acceleration due to aerodynamic drag, and gravitational force. Droplets trajectories calculations are given in detail in Amsden et al. (1989).

3.1.2.1 Equations of Motion for Discrete Droplet Phase

The equation of motion for a single spherical droplet is given by:

$$\mathbf{a}_d = \frac{d\mathbf{u}_d}{dt} = \frac{\mathbf{u} + \mathbf{u}' - \mathbf{u}_d}{\tau} + \mathbf{g} \tag{3.11}$$

where τ is the dynamic relaxation time of the droplet, which is defined as:

$$\tau^{-1} = \frac{3}{8}\frac{\rho_g}{\rho_l r_d} C_D \left|\mathbf{u} + \mathbf{u}' - \mathbf{u}_d\right| \tag{3.12}$$

where C_D is the viscous drag coefficient, which is defined as:

$$C_D = \begin{cases} \dfrac{24}{\mathrm{Re}_d}\left(1 + \dfrac{1}{6}\mathrm{Re}_d^{2/3}\right), & \mathrm{Re}_d \le 1000 \\ 0.424, & \mathrm{Re}_d > 1000 \end{cases} \tag{3.13}$$

with droplet Reynolds number defined as:

$$\mathrm{Re}_d = \frac{2\rho_g \left|\mathbf{u} + \mathbf{u}' - \mathbf{u}_d\right| r_d}{\mu_g(\hat{T})} \tag{3.14}$$

where μ_g is the dynamic viscosity of air, which is calculated at the average film temperature defined by $\hat{T} = (T_g + 2T_s)/3$.

3.1.2.2 Boundary Conditions for Discrete Droplet Phase

For a spherically symmetric droplet with only variations in radial direction, the interface mass conservation condition for each vaporizing fuel species *i* can be written as:

$$\rho_{ls}(v_{ls}-\dot{r}_d)(Y_{gs,i}-Y_{ls,i})+\rho_{ls}D_l\left.\frac{\partial Y_i}{\partial r}\right|_{ls}+\rho_{gs}D_{g,i}Sh_{g,i}\frac{Y_{gs,i}-Y_{g\infty,i}}{2r_d}=0 \tag{3.15}$$

Summing Eq.(3.15) over all the fuel species, the rate of change of droplet radius can be obtained:

$$\dot{r}_d=v_{ls}-\frac{\rho_{gs}}{2\rho_{ls}r_d}\frac{\sum_{ifuel}D_{g,i}Sh_{g,i}(Y_{gs,i}-Y_{g\infty,i})}{1-\sum_{ifuel}Y_{gs,i}} \tag{3.16}$$

where $Y_{g\infty,i}$ is the average vapor mass fraction of fuel species *i* within the computational cell traversed by the droplet. $Sh_{g,i}$ is the Sherwood number for fuel species *i* and is given by:

$$Sh_{g,i}=\left(2.0+0.6\,\mathrm{Re}_d^{1/2}\,Sc_{g,i}^{1/3}\right)\frac{\ln(1+B_d)}{B_d} \tag{3.17}$$

where $Sc_{g,i}=\frac{\mu_g(\hat{T})}{(\rho_g D_{g,i})(\hat{T})}$ is the Schmidt number, and $B_d=\frac{\sum_{ifuel}Y_{gs,i}-\sum_{ifuel}Y_{g\infty,i}}{1-\sum_{ifuel}Y_{gs,i}}$ is the global Spalding mass transfer number for vaporizing species.

The interface condition on droplet surface temperature is determined by the energy balance equation:

$$-\sum_{ifuel}L_i\rho_{ls}\left[(\dot{r}_d-v_{ls})Y_{ls,i}+D_l\left.\frac{\partial Y_i}{\partial r}\right|_{ls}\right]=k_{gs}\frac{T_{g\infty}-T_s}{2r_d}Nu_g-k_l\left.\frac{\partial T}{\partial r}\right|_{ls} \tag{3.18}$$

where the first term on the right hand side is the heat flux to the droplet interface from the gas side and the second term is the heat flux to the droplet interface from the liquid side.The difference between the two terms gives the net heat flux at the interface, which should be equal to the heat flux due to the vaporization, which is represented by the term on the left hand side of Eq. (3.18). The Nusselt number is calculated by the Ranz-Marshall correlation [Faeth (1977)]:

$$Nu_g = \left(2.0 + 0.6\,\mathrm{Re}_d^{1/2}\,\mathrm{Pr}_g^{1/3}\right)\frac{\ln(1+B_d)}{B_d} \tag{3.19}$$

where $Pr_g = \frac{\mu_g(\hat{T})c_{pg}(\hat{T})}{K_g(\hat{T})}$ is the gas Prandtl number. Note that the second term on the right hand side of equation 3.19 cannot be neglected even for very small Reynolds numbers. For example, the air Prandtl number is approximately 0.7 for a large range of temperatures, at Re_d=10, $0.6Re^{0.5}Pr^{1/3}$~1.7; at Re_d=1, $0.6Re^{0.5}Pr^{1/3}$~0.5.

3.1.2.3 One-dimensional Equations for Discrete Droplet Phase

Continuity, species transport, and energy equations are solved within each droplet with the assumption that those properties only change in the radial direction:

$$\frac{\partial \rho_l}{\partial t} + \frac{1}{r^2}\frac{\partial}{\partial r}\left(r^2 \rho_l v_r\right) = 0 \tag{3.20}$$

$$\frac{\partial\left(\rho_l Y_{l,i}\right)}{\partial t} + \frac{1}{r^2}\frac{\partial}{\partial r}\left(r^2 \rho_l v_r Y_{l,i}\right) = \frac{1}{r^2}\frac{\partial}{\partial r}\left(r^2 \rho_l D_l \frac{\partial Y_{l,i}}{\partial r}\right) \tag{3.21}$$

$$\frac{\partial\left(\rho_l T\right)}{\partial t} + \frac{1}{r^2}\frac{\partial}{\partial r}\left(r^2 \rho_l v_r T\right) = \frac{1}{c_{pl} r^2}\frac{\partial}{\partial r}\left(r^2 k_l \frac{\partial T}{\partial r}\right) + \frac{\rho_l D_l}{c_{pl} r^2}\sum_i\left[\frac{\partial}{\partial r}\left(r^2 h_{l,i}\frac{\partial Y_{l,i}}{\partial r}\right) - h_{l,i}\frac{\partial}{\partial r}\left(r^2 \frac{\partial Y_{l,i}}{\partial r}\right)\right] \tag{3.22}$$

To solve for ρ_l, v_r, $Y_{l,i}$, T, an additional equation for average liquid density is needed and can be written in terms of mass fraction of each species and their density:

$$\rho_l = \left(\sum_{ifuel} Y_{l,i}/\rho_{l,i}\right)^{-1} \tag{3.23}$$

More details on the numerical algorithms to solve the above 1-D liquid phase equations can be found in [Amsden et al. (1989)].

Once the 1-D liquid phase equations are solved, the mass fraction of each vaporizing species can be determined using Raoult's law for relatively low ambient pressures. Raoult's law states that:

$$p_{gs,i} = X_{ls,i} p_{sat,i}(T_s) \tag{3.24}$$

where $P_{gs,I}$ is the partial pressure for fuel species i at the droplet surface in the gas phase, $P_{sat}(T_s)$ is the saturation pressure for fuel species i at droplet surface temperature, T_s. $X_{ls,I}$ is the mole fraction of fuel species i at the droplet surface in the liquid phase, which can be calculated by:

$$X_{ls,i} = \frac{Y_{ls,i} / MW_i}{\sum_{ifuel} Y_{ls,i} / MW_i} \tag{3.25}$$

$$Y_{gs,i} = \frac{X_{gs,i} MW_i}{\sum_i X_{gs,i} MW_i} = \frac{p_{gs,i} MW_i}{\sum_i p_{gs,i} MW_i} \tag{3.26}$$

3.2 KIVA Program Structure

In this section, the structure of KIVA program and boundary conditions will be discussed. There have been five versions of KIVA program, KIVA [Amsden et al. (1985)], KIVA-II [Amsden et al. (1989)], KIVA-3 [Amsden (1993)], KIVA-3V [Amsden (1997)], and KIVA-4 [Torres (2007)], which is the most up-to-date version.

The first KIVA program developed by LANL was specially designed for the IC engine spray and combustion simulation, all the input parameters were related to the IC engine parameters, such as rpm, crank shaft angels and etc. In response to many users outside the automotive industry, a number of other features were incorporated into KIVA-II, such as gravitational terms, the options to calculate with purely Eulerian or Lagrangian meshes, an inflow and outflow boundaries, which are often used during gas turbine spray and combustion simulations. However, inflow boundary can only be applied at the bottom of the logical mesh and outflow boundary can only be applied at the right or top of the logical mesh. But the modular structure of the KIVA program and an alphabetical epilogue allows one to find the definitions and uses of FORTRAN variables within the code, modifications of the code, such as generalization of inflow/outflow boundary conditions, become easier than it appears to be.

3.2.1 How to use KIVA

As shown in Figure 5, there are three steps when you use KIVA-4 to run a simulation. First, one needs to generate a grid file named otape17 which is readable by the KIVA main program. Along with the KIVA-4 program, there is a parametric grid generator named k3prep, which can generate a moderate complex KIVA grid. For very complicated geometries, one needs to use the commercial mesh generation software, ICEM-CFD, which is capable of writing a KIVA format grid file. After you get an otape17 file, rename it to itape17, and use the grid converter along with KIVA-4 to generate the grid file named kiva4grid which can be read by KIVA-4 main program. Second, one needs to prepare the input file named itape5, which contains all the information for the specified simulations. For non-IC engine simulations, one needs to set

rpm=0.0, and set squish=the height of the mesh in z-direction, irez=0, etc. But of course, one can modify the KIVA program to delete all the IC engine-related parameters. In the last step, some software which is capable of reading KIVA output files need to be used to post-process the simulated data. Available softwares are Tecplot, GMV, Ensight and Fieldview. Certainly, one can write a code to convert the output data in such a format which is readable by preferable post-processing software, such as Tecplot.

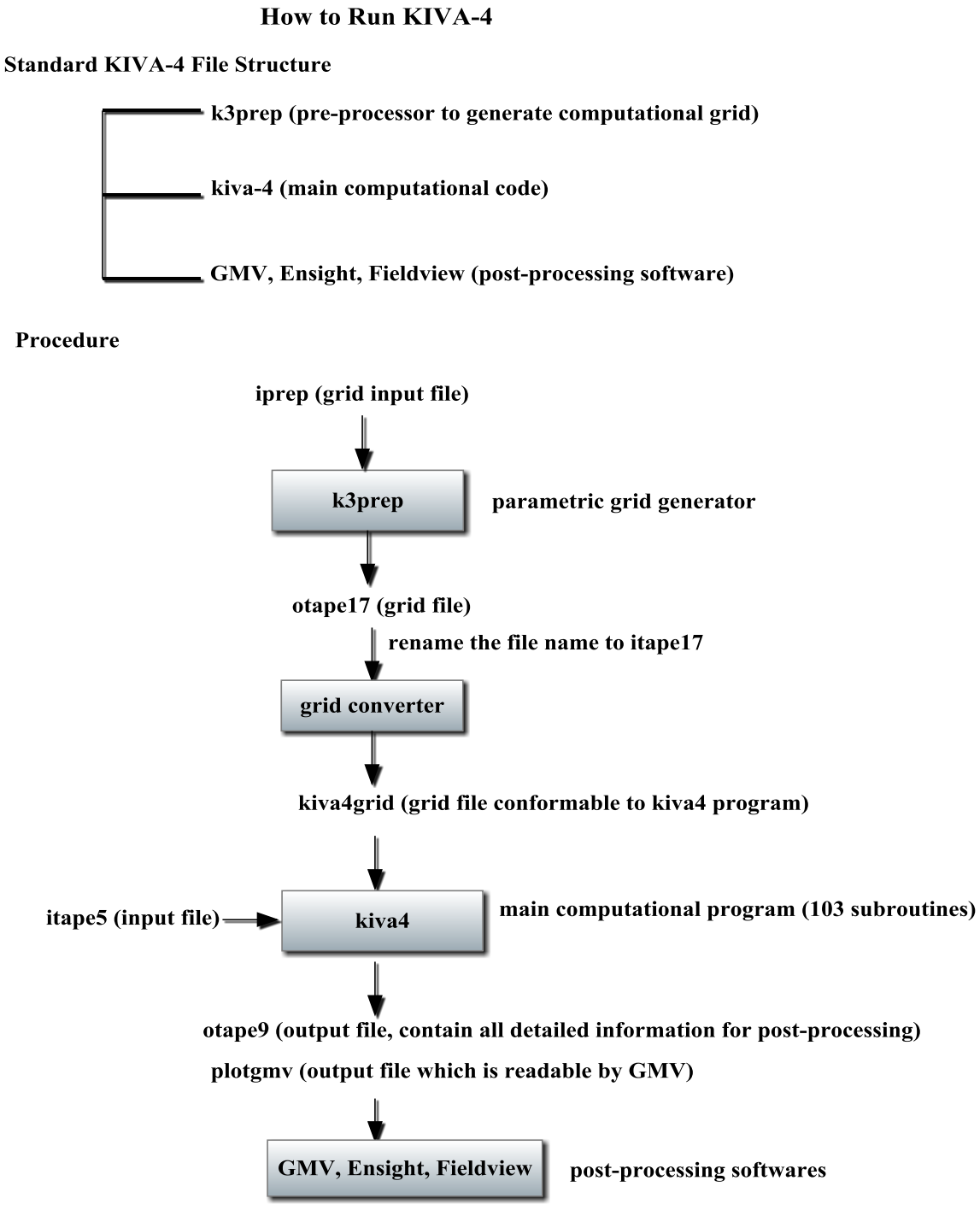

Figure 5: KIVA-4 program structure

3.2.2 Boundary Conditions in KIVA

In addition to inflow and outflow boundaries, other physical boundary conditions, such as solid wall boundary, periodic boundary, pressure inlet and outlet, and dynamically moving boundary conditions are available in KIVA. The dynamically moving boundary condition is specially designed for IC engine simulations where the piston is moving up and down.

For solid wall boundaries, there are several types depending on velocity and temperature boundary conditions. Velocity boundary conditions on solid wall can be free slip, no slip or turbulent law-of-the-wall. Temperature boundary conditions can be adiabatic walls or fixed temperature walls.

Velocity boundary conditions on rigid walls are introduced either by imposing the value of velocity on walls or the value of the wall stress $\sigma_w = \boldsymbol{\sigma} \cdot \mathbf{n}$, where $\mathbf{n}$ is the unit normal to the wall. On no slip walls, the gas velocity is set equal to the wall velocity:

$$\mathbf{u} = v_{wall}\mathbf{k} \tag{3.27}$$

where the wall is assumed to be moving with speed v_{wall} in the $\mathbf{k}$ direction. The wall stress is determined implicitly through Equation (3.3). On free-slip and turbulent law-of-wall conditions the tangential components are determined by matching to a logarithmic profile:

$$\frac{v}{u^*} = \begin{cases} \frac{1}{\kappa}\ln\left(c_{lw}\zeta^{7/8}\right) + B & \zeta > Rc \\ \zeta^{1/2} & \zeta < Rc \end{cases} \tag{3.28}$$

where $\zeta = \rho y v / \mu_{air}(T)$ is the Reynolds number based on the gas velocity relative to the wall, and $v = \left|\mathbf{u} - v_{wall}\mathbf{k}\right|$, which is evaluated a distance y from the wall, and u^* is the shear speed, which is related to the tangential components of the wall stress by:

$$\boldsymbol{\sigma}_w - (\boldsymbol{\sigma}_w \cdot \mathbf{n})\mathbf{n} = \rho (u^*)^2 \frac{\mathbf{v}}{v} \tag{3.29}$$

where $\mathbf{v} = \mathbf{u} - v_{wall}\mathbf{k}$. It is assumed that y is small enough to be in the logarithmic region or the laminar sub-layer region of the turbulent boundary layer. The Reynolds number Rc defines the boundary between these two regions. The constant κ, c_{lw}, Rc and B are related to the k-ε model constant by:

$$\kappa = \sqrt{c_\mu^{1/2}\left(c_{\varepsilon 2} - c_{\varepsilon 1}\right)\mathrm{Pr}_\varepsilon} \text{ and } B = Rc^{1/2} - 1/\kappa \ln(c_{lw} Rc^{7/8}) \tag{3.30}$$

For commonly accepted k-ε constants, $B = 5.5, c_{lw} = 0.15, \kappa = 0.4234$ and R_c=114.

CHAPTER FOUR: VALIDATION OF VAPORIZATION MODEL

In this chapter, the vaporization model will be validated with some existing experimental data. An accurate vaporization model is crucial for this study since its main topic is to predict the vaporization performance for liquid fuel sprays in the pre-mixer. Traditionally, the validation of the vaporization model is done by comparing with single droplet vaporization experiments, during which the diameter and temperature of the vaporizing droplet are recorded.

4.1 Validation of Numerical Results with Experiments at Low Temperatures

In this section, a few cases have been setup and compared with the experimental data of D*ä*if et al. (1999), who performed a single droplet vaporization experiment with relatively low convective air temperature. In their experiments, a single droplet was suspended from a permanent holder in a thermal wind tunnel equipped with a video recording system and an infrared camera. The droplets underwent vaporization in a hot convective air flow in the wind tunnel with velocity range of 3.1~3.4 m/s and temperature range of 341 K~390 K. The droplet diameter reduction and surface temperature data was reported. The initial droplet diameters were varied in the range of 1.0~1.5 mm. In our simulation, all the cases are setup with the same initial conditions as reported by D*ä*if et al. (1999). Unlike in a spray environment, the far field fuel vapor mass fraction was considered to be zero since there are no other droplets vaporizing in the neighborhood, and velocity and temperature of the external air were held constant during the simulations. Moreover, in order to maintain the same physical conditions as done in the experiments, the droplet velocity was maintained at zero.

Figures 6 and Figure 7 show the comparisons between the simulations and the experiments for single droplets in both pure (heptane and decane) and blended forms (mixture of heptane and decane at three different concentrations). The computational parameters for all cases are listed in Table 2. The transient changes of diameter of both blended and pure droplets show very good agreement with the experiments. For single-component droplet vaporization from figure 6, the droplet diameter square reduces linearly with time, which is consistent with the famous D^2 law for single-component droplet vaporization under low convective temperatures. However, for multi-component droplet vaporizations, the droplet diameter square may not reduce linearly with time. For example, in figure 7b, the droplet diameter regression shows two phases: the first phase shows a larger linear regression slope which indicates the evaporation of the heptane species and the second phase shows a smaller linear regression slope which corresponds to the evaporation of the decane species. This was not evident in figure 7a because the heptane component quickly evaporated due to the its low concentration (21.3%) and its high vaporization rate. This indicates that the diameter regression slope represents mostly the vaporization of decane, which illustrates the same slope and vaporization time scale as the pure decane vaporization depicted in figure 6. Torres et al. (2003) also conducted similar comparisons to test KIVA vaporization model. However, in their simulation, thermal expansion induced a diameter increase at the initial stage of the decane droplet evaporation. This is caused by decane's slow vaporization rate and the variable liquid density. In the initial stage, decane's droplet temperature increases quickly due to slow vaporization rate which will cause a density decrease, resulting in a diameter increase. In the current model a constant density model for decane droplet was used. The temperature data compares fairly well with the experimental work with a maximum deviation of 8 K. The

deviations from the simulation data to the experimental data are possibly due to property variations and uncertainties in the boundary conditions.

Table 1: Summary of experiment conditions for all pure and binary mixture droplets of D*ä*if et al. (1999) experiments

Binary concentration	Pure Heptane	Pure Decane	H-D (75%-25%)	H-D (21.3%-78.7%)
Initial droplet diameter (mm)	1.052	1.386	1.334	1.486
Initial droplet temperature (K)	290	290	294	294
Crossflow velocity (m/s)	3.2	3.1	3.1	3.1
Crossflow Temperature (K)	356	348	348	348

(%-%) is the volumetric concentration for heptane and decane in the binary droplet

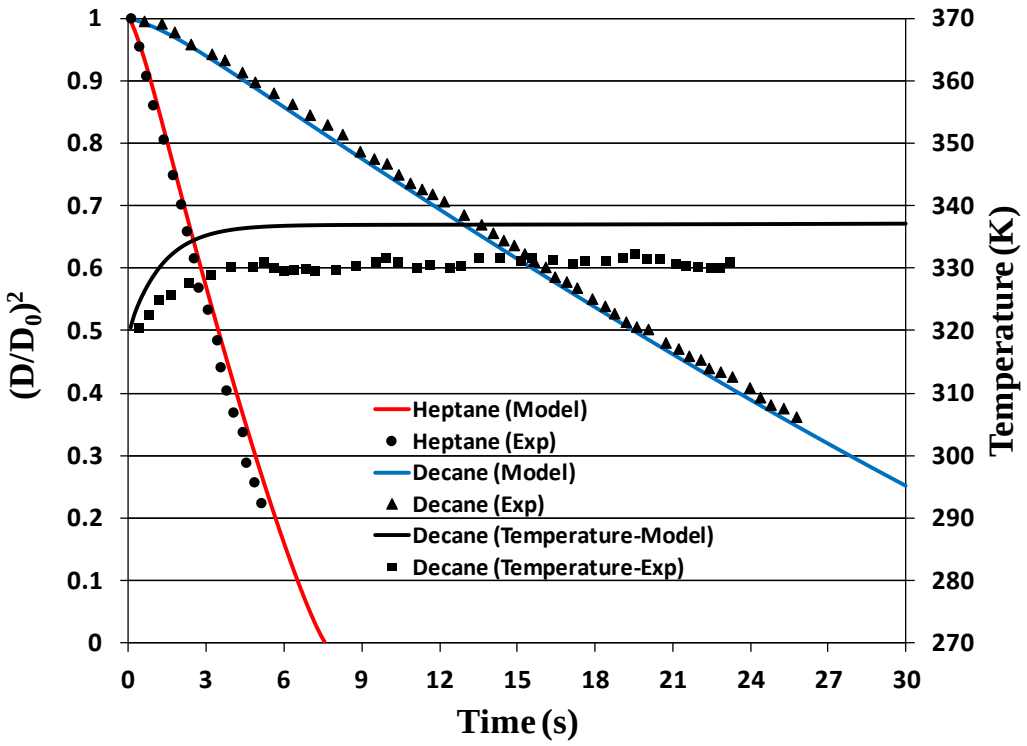

Figure 6:. Comparisons between the model and the experiment data for pure heptane and decane droplet

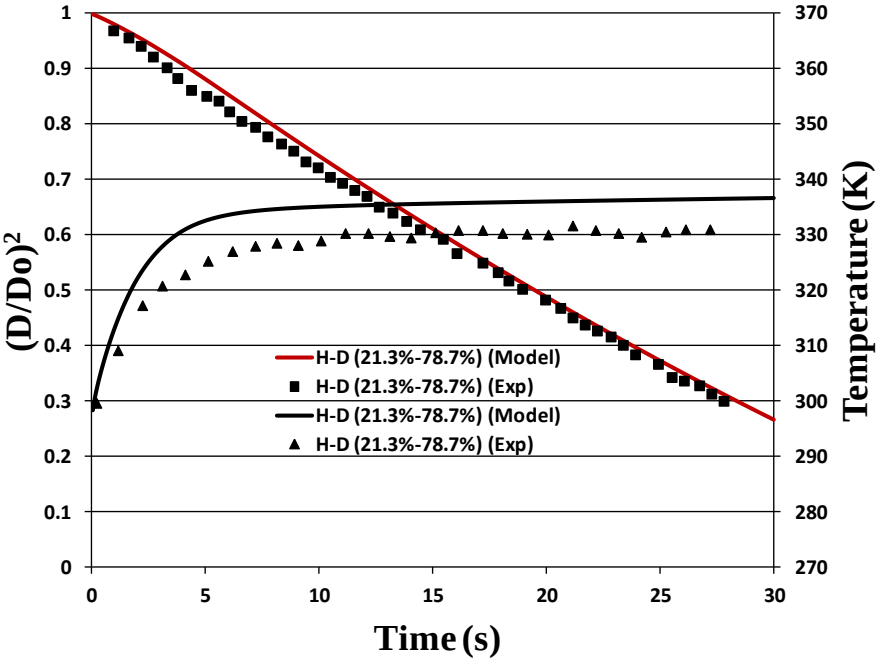

(a)

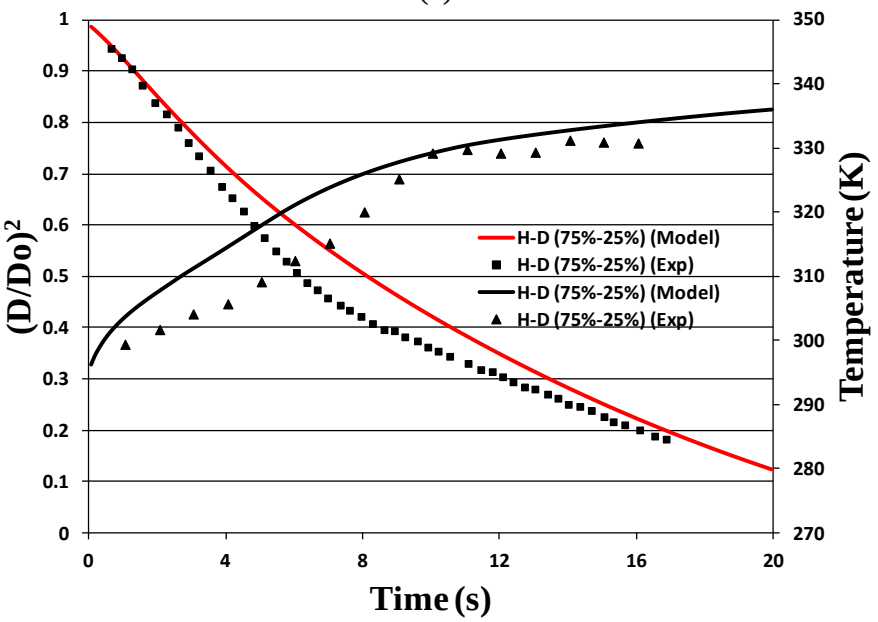

(b)

Figure 7:. Comparisons between the model and the experiment data for binary mixture of heptane and decane droplet at different volumetric concentrations, a) binary droplet with higher concentration of decane b) binary droplet with higher concentration of heptane (H-D is short for Heptane-Decane)

4.2 Validation of Numerical Results with Experiments at High Temperatures

In the previous section, all the validation cases of single droplet vaporization were conducted under low convective temperatures. Miller et al. (1998) stated that non-equilibrium effects become significant when droplet diameters less than 50 micron are vaporizing in convective air with temperatures higher than the fuel boiling temperature. However, the non-equilibrium effects are found to be negligible for droplet diameter larger than 1 micron within KIVA's vaporization framework. In order to validate KIVA's vaporization model for high convective air temperature situations, a single decane droplet is vaporized at 1000 K convective air temperature with a velocity of 1 m/s. The initial diameter and temperature of the decane droplets are 2 mm and 315 K, respectively. Figure 8 shows good comparisons between the current model and the original experimental data from Wong and Lin (1992). Both the current model and Miller's non-equilibrium model show good comparison for the 2mm droplet case with Wong and Lin's experimental data.

The differences between the classical equilibrium model and Miller's non-equilibrium model are summarized as follows: First, for the classical equilibrium model, the gas properties are evaluated by the well-known "1/3 rule", where the film temperature is used instead of the absolute gas temperature. Since the surface temperature of the droplet is constantly changing, the film temperature is updated at every time step. The fuel vapor mass fraction at the droplet surface is calculated based on the droplet instantaneous surface temperature. Thus, the vaporization rate will not over predict since the Sherwood number is lower based on the film temperature compared to its value based on the free stream gas temperature. On the other hand,

in Miller's non-equilibrium model, they used an alternative approach in which the properties of both vapor and gas are evaluated only once at the beginning of each simulation. They assumed that the droplet surface temperature would quickly reach the wet bulb temperature which is appropriate to evaluate vapor properties. They used a correlation to evaluate the wet bulb temperature which is a function of the liquid fuel boiling temperature and free stream gas temperature. Their gas properties are evaluated based on the free stream gas temperature. Since the classical equilibrium model and the non-equilibrium model predict vaporization rates in a similar manner for the 2 mm droplet, the classical equilibrium model was used for all subsequent spray cases for which the droplet diameter was maintained constant at 80 μm.

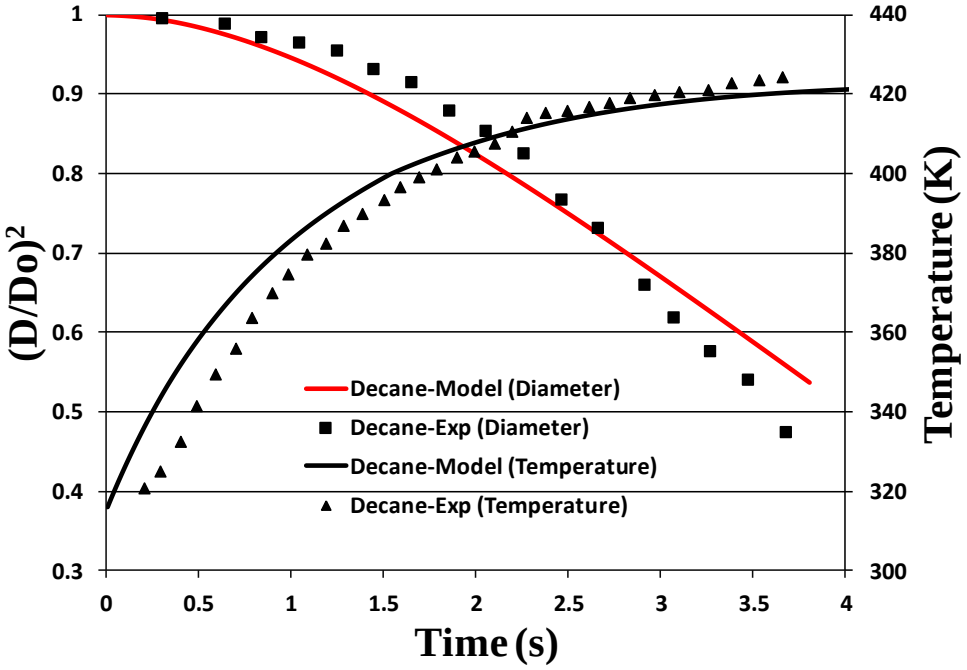

Figure 8: Comparisons between the model and the experiment data for single decane droplet vaporization under high convective air temperature (1000 K)

CHAPTER FIVE: SIMULATION RESUTLS FOR RECTANGULAR SHAPE PRE-MIXER

In this chapter, the simulatied results will be presented for all liquid fuels spray in a typical rectangular shape pre-mixer. The main assumption is that the droplet-droplet interactions are negligible for the particular problem of concern since the droplets will be sparsely distributed in space for lean fuel-air sprays and the incoming air temperature is extremely high such that droplet-droplet interactions on the total vaporization performance is negligible . This chapter will be organized as follows: the first section will describe the crossflow injection methods that are used for the fuel sprays with the original drag model implemented in KIVA to compare the results for the different fuels through extensive analysis; the second section, will consider the crossflow injection for all the fuels using an improved drag model with Stefan flow correction at low Reynolds numbers for comparison between the two methods; the third section will introduce the co-flow injection simulations with the same conditions as crossflow injections; the last section will present results for comparison between co-flow injections and crossflow injections, and the conclusions that are drawn.

5.1 Crossflow Simulation Results

5.1.1 Introduction

Since the trend toward reducing the size and weight of gas turbine engines requires a more compact combustor, increased emphasis is placed on decreasing the mixing length while still achieving a well premixed air and fuel mixture for low-pollutant emissions. Atomizing the liquid

fuel before its injection into a crossflow reduces the mixing length by the distance that would have been associated with the time required for liquid breakup. By injecting the spray transversely rather than coaxially into the incoming flow allows the air flow to take advantage of the dynamic mixing induced by the jet-crossflow interaction [Chin et al. (1986)]. In this study, the fuel will be atomized before delivering into the pre-mixer chamber. Thus, when the droplets meet the high speed and high temperature crossflow air, they will breakup into smaller droplets and vaporize very quickly.

5.1.2 Computational Setup

Four different types of liquid fuels are investigated here. Two of them are bio-fuels (ethanol and RME), where ethanol is considered as a substitute for gasoline and RME is categorized in the family of biodiesels which can be blended into jet fuels. RME has already been tested in blends with Jet-A fuel as potential surrogate fuel for the aviation industry [Dagaut et al. (2007)]. Most of the fuels studied here except ethanol are comprised of more than one species with different transport properties. In order to avoid numerical complexity, averaged properties are used and tabulated in Table 3. Since the fuel vapor pressure is an important parameter for the liquid fuel vaporization process, the fuel vapor pressure for different fuels is plotted versus temperature in Figure 9. The properties of Jet-A are taken from the tabulated data within the KIVA source code while those of ethanol, gasoline and RME are provided from reference [Saha et al. (2010)]. It can be seen that the vapor pressure is a monotonically increasing function of temperature for all the fuels. Vapor pressures of gasoline and ethanol are higher than those of jet-A and RME, indicating that gasoline and ethanol are more volatile fuels in nature.

Table 2: Properties of fuel

Fuel Name	Ethanol	Gasoline	Jet-A	RME
Molecular Mass (g/mole)	46	113	167	300
Density (kg/m^3)	790	751	808	880
Thermal Conductivity at 300K (W/m-K)	0.166	0.115	0.114	0.182
Latent heat (J/Kg)	904000	317700	322200	254000
Dynamic viscosity at 300K (Pa-s)	0.00105	0.000489	0.00117	0.00389
Boiling Temperature at 1 atm (K)	351.3	375	465	653
Wet Bulb Temperature under 800 K (K)	328	346	438	589

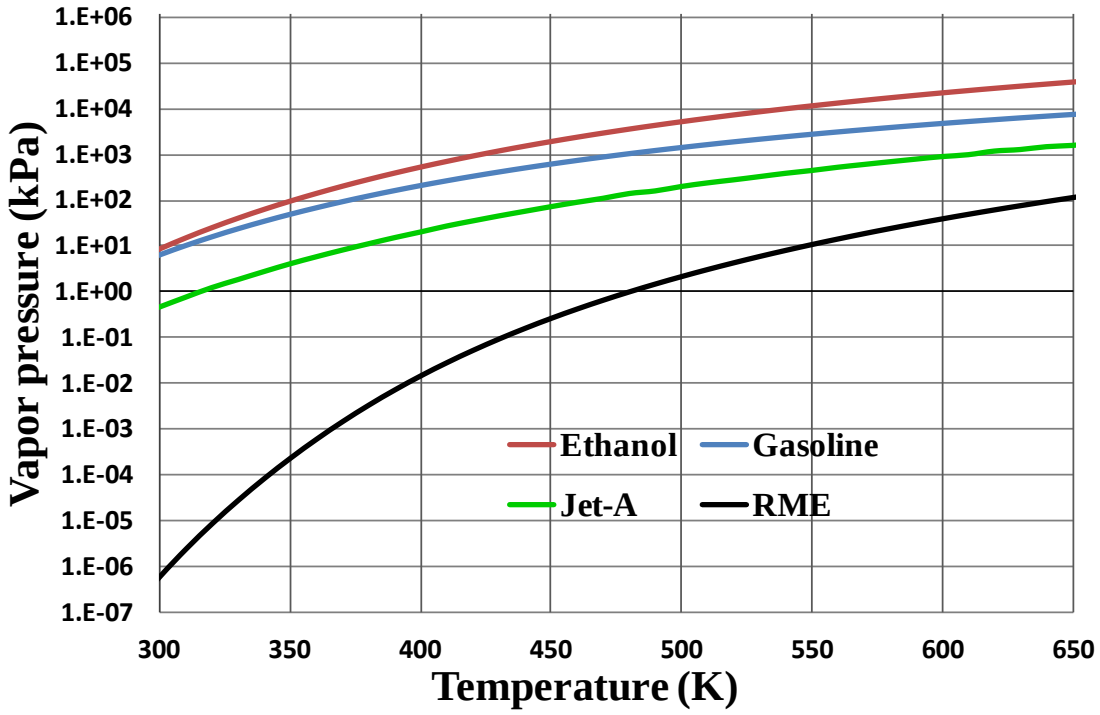

Figure 9: Vapor pressures of different fuels

The computational domain in Figure 10 represents a typical pre-mixer with a length of 300 mm and a cross section of 60mm x 60mm. A uniform grid of 15x15x75 is used for all the cases. The pre-mixer has six bounding surfaces with the following set of boundary conditions: the left side is assigned as velocity inlet boundary condition with fixed crossflow velocity and the right side is pressure outlet boundary condition, and all other sides of the domain are assigned law-of-wall boundary conditions. The air is introduced into the pre-mixer at a constant velocity and temperature of 10 m/sec and 800 K respectively. An Eulerian-Lagrangian unsteady particle tracking method is implemented in KIVA. The turbulent k-ϵ model is used for the gas phase flow solver. The flow field quickly reaches a quasi-steady state in less than 0.01 s with a time step size of 10^{-5} s. Figure 10 also shows the quasi-steady state gas phase velocity in the crossflow direction at two cross-sectional planes of Z=100 mm and Z=250 mm respectively.

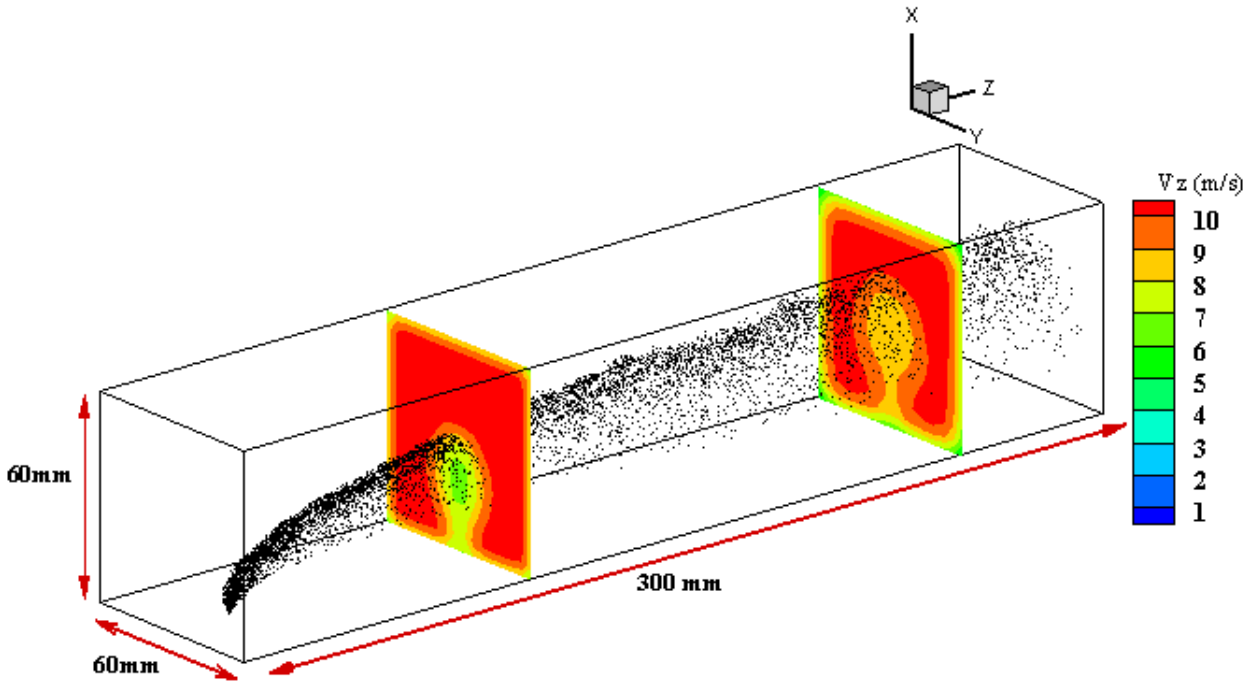

Figure 10: 3-D view of Computational domain with converged velocity field

The fuel droplets are injected transversely with a spray cone angle of 70 degrees 0.01 sec after the start of the simulation. The simulation will reach a quasi-steady state after 0.05 sec which means that the droplets injected at 0.01 secs will reach the exit of the pre-mixer after 0.05 secs resulting in a total residence time of 0.04 secs. The injector is located at the bottom surface of the pre-mixer chamber at a distance of 2 cm downstream of the air inlet. By testing a series of injection velocities from 1 m/s to 6 m/s, an optimum injection velocity of 3.5 m/s was determined. The droplets trajectories for all three tested injection velocities are shown in Figure 11. A summary of flow conditions is listed in Table 4. In this study, the typical size of the droplets being considered are 80 μm in diameter. All the simulation cases were run at atmospheric pressure. In order to achieve better droplet dispersion and vaporization performance, a high value of turbulent intensity (20% of the mean crossflow kinetic energy) was used for all the simulations reported here.

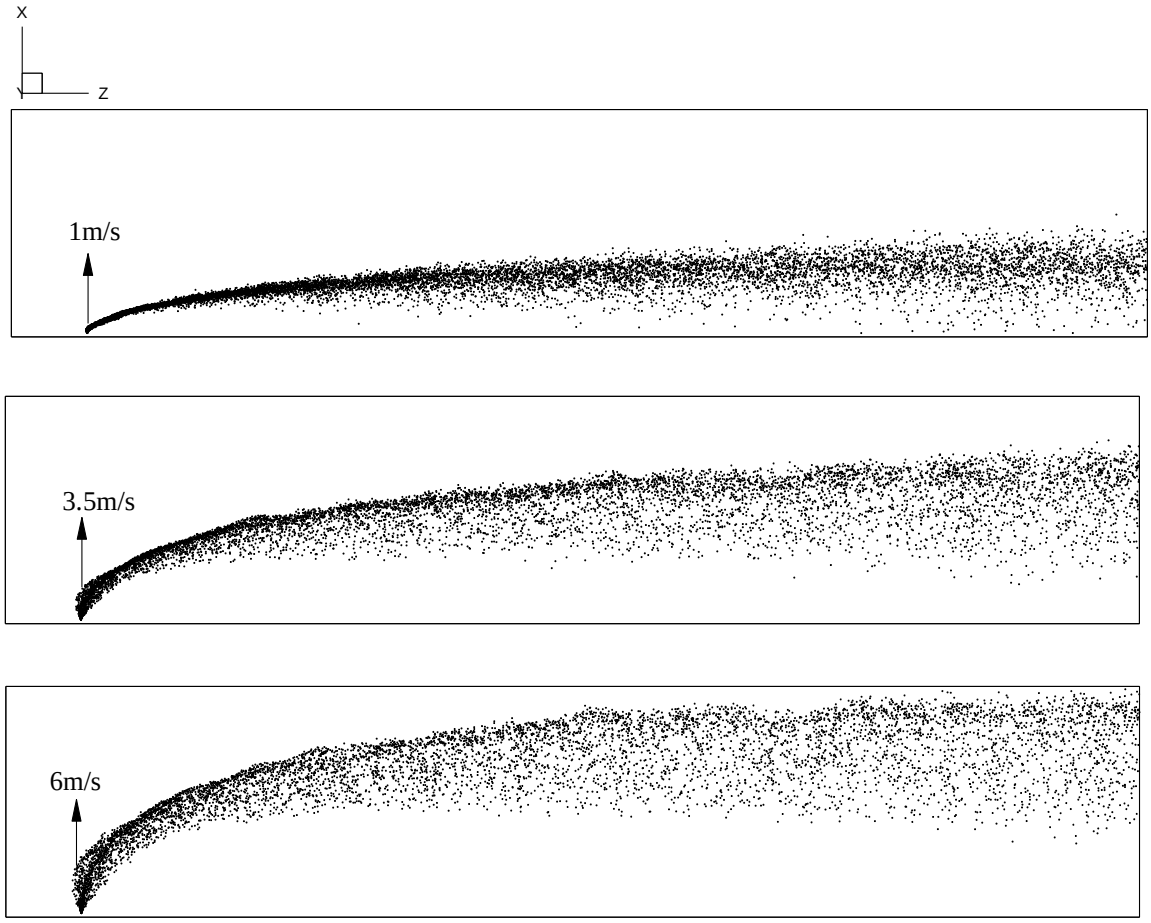

Figure 11: Parallel projection of jet-A droplets trajectories onto X-Z plane at different injection velocities

Table 3: Summary of flow conditions

Initial droplet diameter (μm)	Crossflow velocity (m/s)	Crossflow temperature (K)	Crossflow turbulent intensity	Droplet injection velocity (m/s)	Spray cone angle (degree)	Fuel mass flow rate (g/s)
80	10	800	0.2	3.5	70	0.918

5.1.3 Single Drop Injection into the Pre-mixer

Prior to the spray simulation, single droplet injections for all the different fuels are simulated in order to test their lifetime scale and temperature rise. Figure 12a shows gasoline having a lifetime of 18 millisecond, ethanol 34 millisecond, Jet-A 35 millisecond, and RME 45 millisecond. Results indicate gasoline is the most volatile fuel, which can be simply explained by its high vapor pressure. Figure 12b shows the temperature change for all fuels with time. All of them reach an equilibrium temperature after a period of time during the vaporization process. This equilibrium temperature is called “wet bulb temperature”, by analogy to a psychrometer [Faeth (1977)]. This can be explained as follows: when the droplet at room temperature is injected into a hot convective environment, initially the surface temperature of the droplet increases quickly like a cold body suddenly placed into a hot furnace. With the sudden increase of surface temperature, the vapor pressure of the droplet will increase, resulting in an increase in fuel vapor concentration at the droplet surface, which will in turn speed up the vaporization process. This has two effects: first, the increase of the vaporization rate with more fuel vapor diffusing outward into the air will lower the heat transfer rate into the droplet from the air side; second, the total heat consumed by the droplet as latent heat of vaporization will increase due to higher rate of vaporization. This slows down the increase of the droplet surface temperature. At a certain point of time, the heat consumed by the droplet as latent heat will be balanced by the total heat transferred to the droplet from the surrounding gas phase (convective environment). Hence the droplet temperature will remain at a constant value which is its wet bulb temperature [Faeth (1977)].

One interesting observation from Figure 12a is that gasoline vaporizes much faster than ethanol. From Figure 9, at the same temperature, ethanol has a higher vapor pressure than gasoline, which should result in ethanol vaporizing faster than gasoline. However, the heat of vaporization of ethanol (904 KJ/Kg) is almost three times higher than that of gasoline (317.7 KJ/Kg) [Table 2], indicating that ethanol needs three times more heat than gasoline to vaporize the same amount of mass. Thus, the temperature rise of ethanol is much slower compared to gasoline in the same convective environment. Figure 12b shows that the wet bulb temperature of gasoline is 346 K while that of ethanol is 328 K. The vapor pressure of gasoline at 346 K is 44.7 KPa, which is higher than the vapor pressure of ethanol at 328 K (37 KPa). For the rest of the fuels, the wet bulb temperatures are much higher compared to gasoline and ethanol since their vaporization rates are much lower due to their low vapor pressures. The wet bulb temperatures of jet-A and RME are around 438 K and 589 K, respectively. This phenomenon has also been reported by Saha et al. (2010) in some details for single droplets involving different fuel blends.

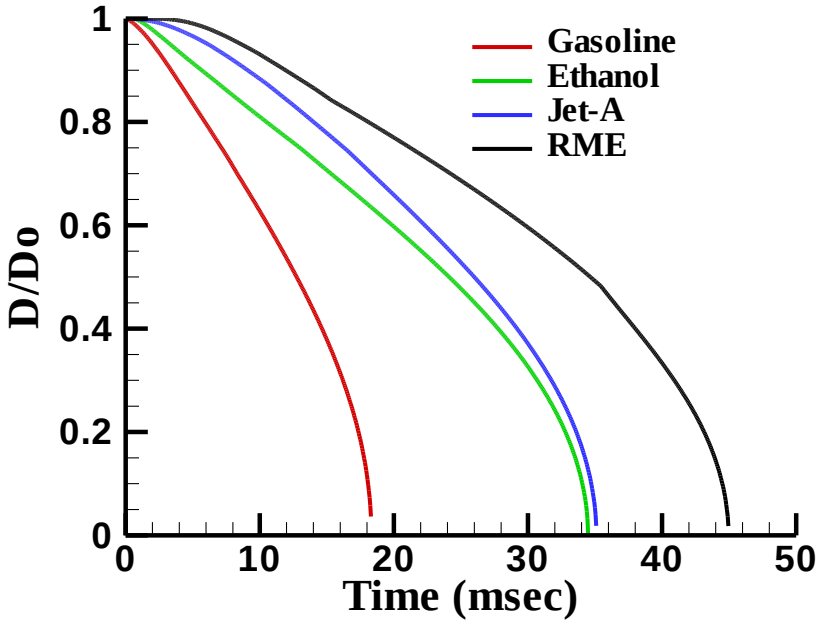

a)

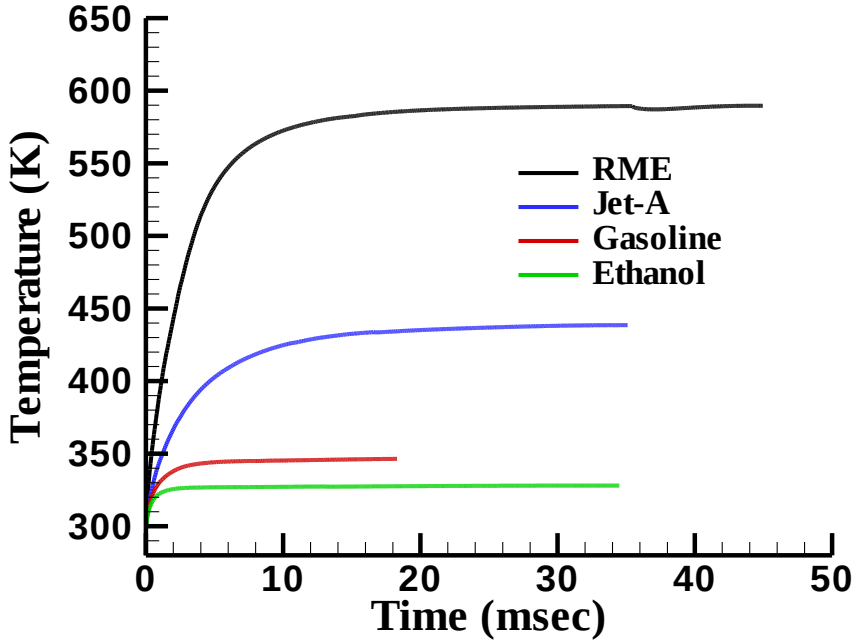

b)

Figure 12: Single droplet injection into the pre-mixer with initial temperature of 293 K a) Diameter reduction vs time b) Surface temperature rise vs time.

5.1.4 Mono-dispersed Spray Simulation at Low Injection Temperature

In this section, the spray simulation results are presented for all the fuels with the same initial injection temperature of 293 K. In order to show the statistical behavior of the droplets during a spray, the average droplet diameter and temperature are calculated by equally dividing the pre-mixer into 40 zones along Z direction from the injection port to the exit. From the definition of Sauter-Mean-Diameter (SMD) for a single droplet, $D_{32} = 6\frac{V_p}{A_p}$, the SMD within each zone can be calculated as:

$$SMD_{spray} = 6\sum_{j=1}^{n} V_{pj} / \sum_{j=1}^{n} A_{pj} \tag{5.1}$$

The average droplet surface temperature is calculated by:

$$T_{s\_spray} = \sum_{j=1}^{n} T_{sj} A_{pj} / \sum_{j=1}^{n} A_{pj} \tag{5.2}$$

Figure 13 and 14 compare the averaged droplet vaporization behavior within the spray to the single droplet vaporization along the crossflow direction for ethanol/ gasoline, and jet-A/RME respectively. As observed from Figure 13a, the SMD reduction of ethanol droplets was 52.8% of the initial diameter size near the exit of the pre-mixer, while gasoline droplets are fully vaporized. Figure 14a shows that the SMD of jet-A and RME droplets reduced to 48.4% and 63.5% of its initial size, respectively. From the comparisons it can clearly be seenthat the SMD for the spray is larger than the diameter of single droplet injection at any point in time, indicating a decrease of

vaporization rate for a spray. This can be explained as follows. First, the temperature of the crossflow air is largely reduced in the spray zone due to the low temperature of the fuel droplet cloud, thus the heat transfer rate to each droplet within the spray will be much lower compared to single droplet injection. So the temperature rise of each individual droplet will be correspondingly lower, resulting in a lower vaporization rate. Second, the vapor mass fraction in the neighborhood (Y_∞) is almost zero for single droplet injection, while the vapor mass fraction in the neighborhood (Y_∞) within the spray has the same order of magnitude compared to the surface vapor mass fraction. This will result in a decrease of vapor concentration gradient, which in turn lowers the vapor diffusion rate. The Spalding mass transfer number for each individual droplet within the spray will be much lower compared to single droplet injection. Thus, from Eq. (7), the vaporization rate will decrease for a spray. Figures 13b and Figure 14b also show a decrease of the droplet wet bulb temperature, which is a function of the free stream temperature. This is corroborated by the fact that the free stream temperature around the droplet is less than 800 K.

One more aspect to compare the vaporization performance for different fuels is by looking at the fuel vapor mass fraction contour plots along the pre-mixer. Figure 15 is a comparison of vapor mass fraction between gasoline and ethanol sprays in the vertical plane of symmetry (y=0). It can be seen that the maximum value of the gasoline vapor mass fraction is 0.3, which is much higher than that of ethanol. The scatter plot shows that all the gasoline droplets are fully vaporized prior to the exit, indicating that the current length of the pre-mixer is suitable for gasoline injection without pre-heating.

Due to the nature of mono-dispersed spay, each individual droplet within the spray was expected to experience similar vaporization process. However, large deviations of the droplet diameter and surface temperatures are found from droplet to droplet within the spray. The droplets located in the center of spray are shielded by the neighboring droplets, thus reducing the heat transfer at the spray core compared to the droplets at the periphery. Figure 16 shows the droplet size and surface temperature distribution of the spray for jet-A. From the Y-Z plane view (Figure 16a), one can clearly see a symmetrical temperature distribution from the center of spray, with a gradual increase in droplet temperature from the center to the periphery. The droplets at the periphery quickly reach the wet bulb temperature within 60 mm from the injection port while the droplets in the middle take about 100 mm to reach the wet bulb temperature. The temperature difference among the droplets indicates that the vaporization rate for each individual droplet will be different. This can be observed in Figure 16b, which shows a large variation in droplet diameter distribution. Similar observations can be made from other fuels as well. The only difference is that a different fuel type will register different deviations of temperature and diameter from the middle of the spray cone to the periphery mainly due to the different wet bulb temperatures and vapor pressures.

To quantitatively show the large distribution of droplet size due to the spray cone, Figure 17 plots the histogram of the droplet diameter distributions for ethanol, jet-A and RME in the primary zone of interest, i.e., near the exit, which is defined from cross-section plane z = 28cm to plane z = 30cm. This plot also shows how well the injected droplets are vaporized right before they exit the pre-mixer. The gasoline spray is not shown since its droplets are fully vaporized

upstream of the exit of the pre-mixer. In Figure 17, the bin range of the histogram is defined from zero to the maximum diameter existing in the zone for different fuels, which is about 62 microns, and each bin size is 2 microns. The frequency is normalized by the total droplet count within the zone of interest for each fuel. As seen from the diameter histogram, ethanol and jet-A both have a diameter range from 12 micron to 54 micron, while RME has a diameter range from 40 micron to 62 micron. The large range of diameter distributions near the pre-mixer exit indicates the vaporization performance is far from desired and significant improvement is needed.

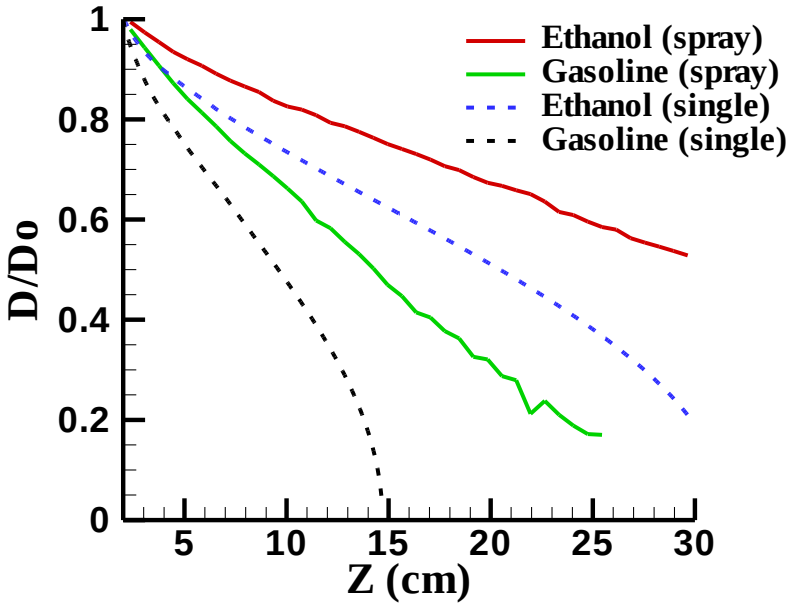

a)

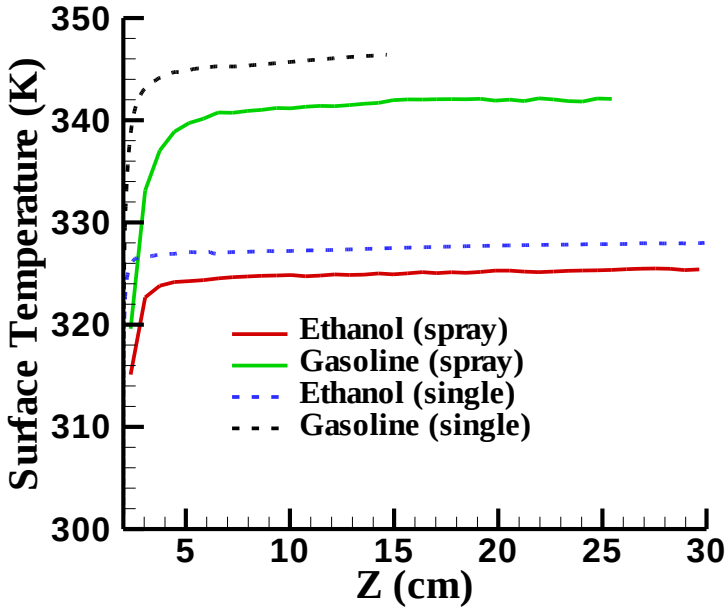

b)

Figure 13: Comparisons between single droplet vaporization and spray vaporization for ethanol and gasoline (a) Diameter reduction along Z (b) Surface temperature rise along Z

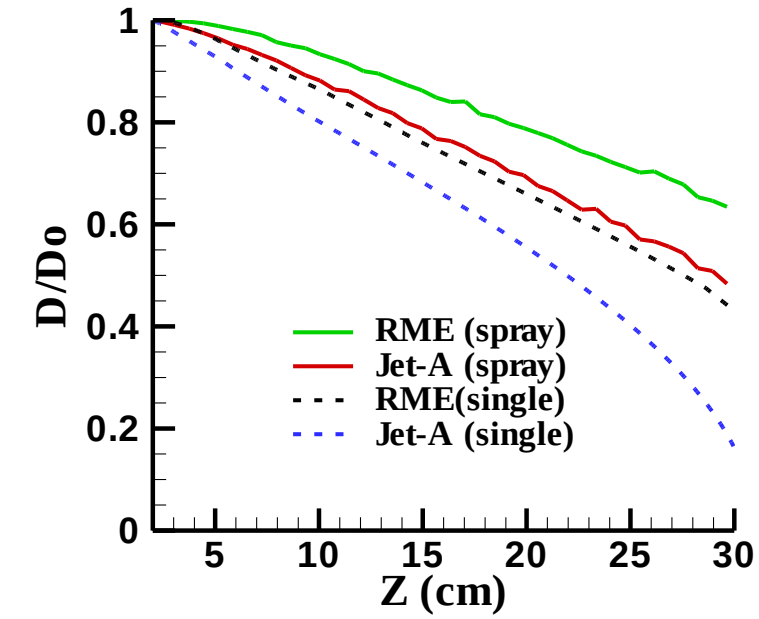

a)

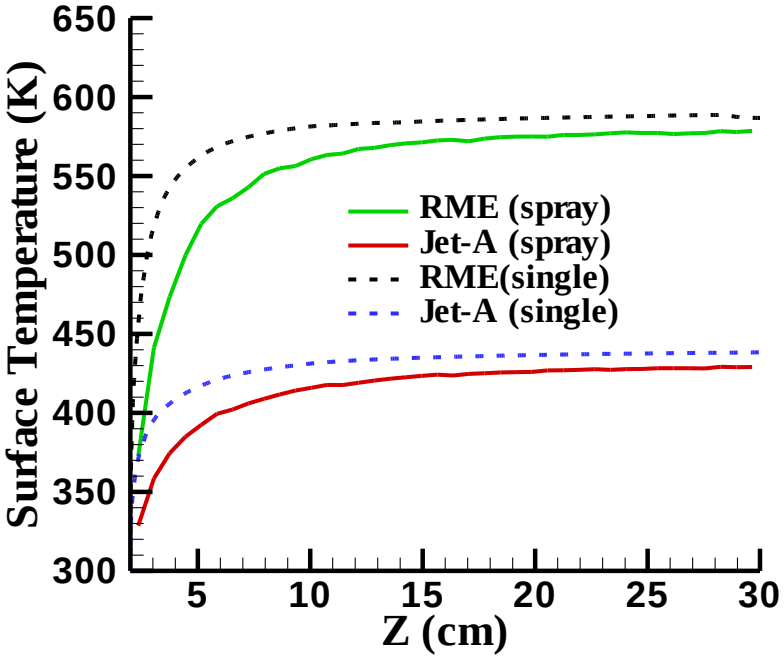

b)

Figure 14: Comparisons between single droplet vaporization and spray vaporization for jet-A and RME (a) Diameter reduction along Z (b) Surface temperature rise along Z

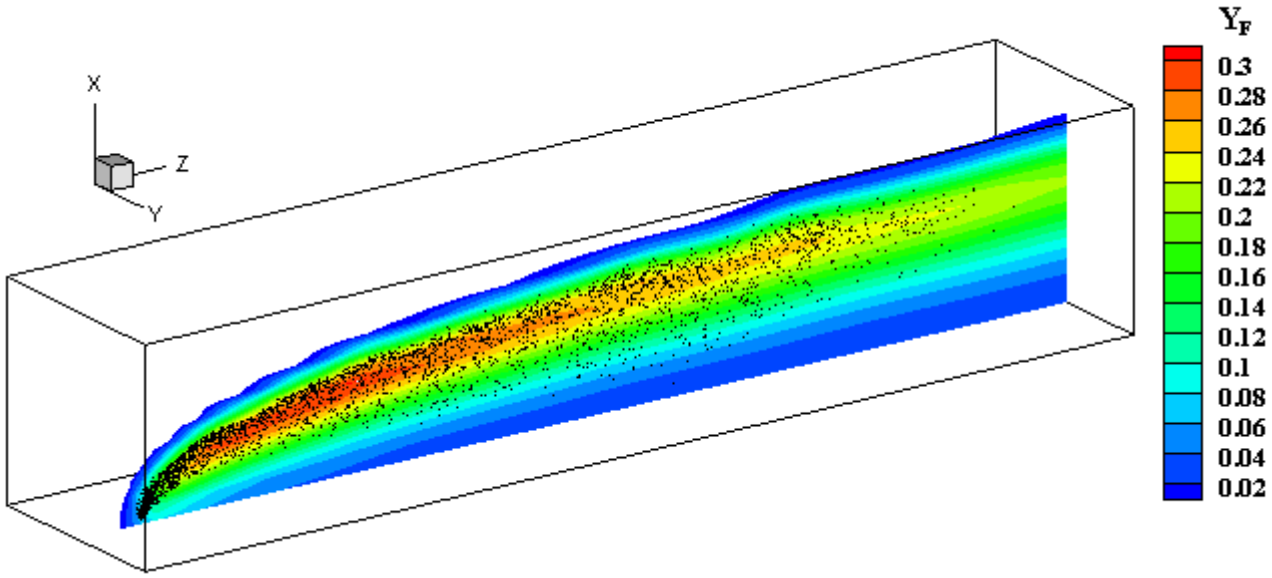

a)

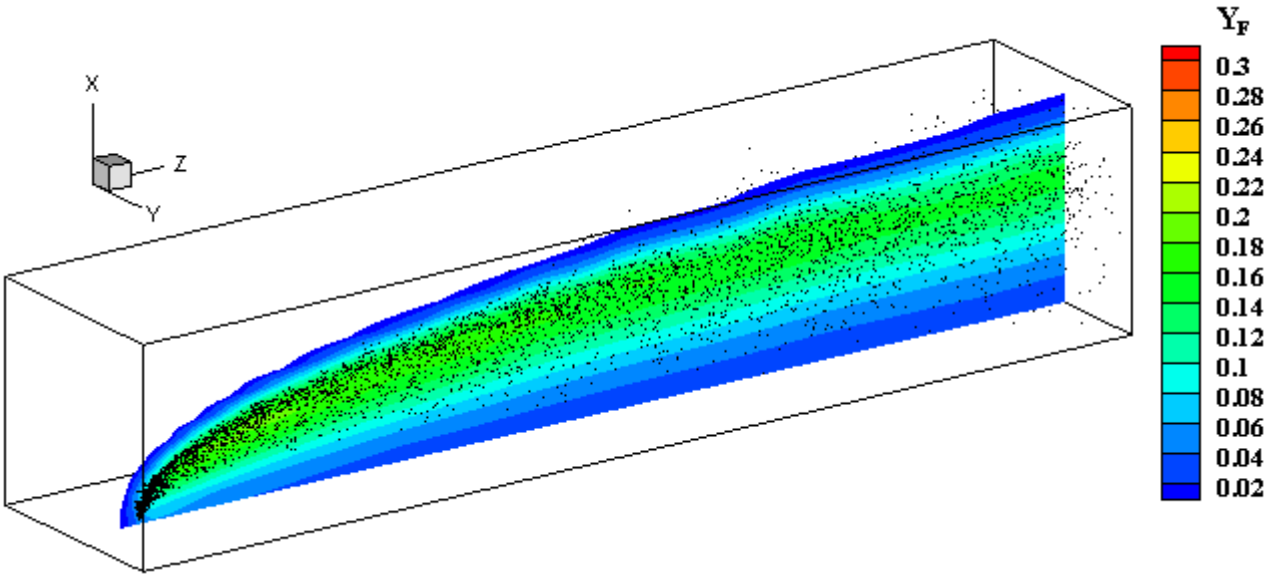

b)

Figure 15: Gasoline and ethanol vapor mass fraction contour plots at the symmetrical plane of y=0 with initial temperature of 293 K, a) Gasoline b) Ethanol (Note: The portion where vapor mass fraction is less than 0.02 is not shown)

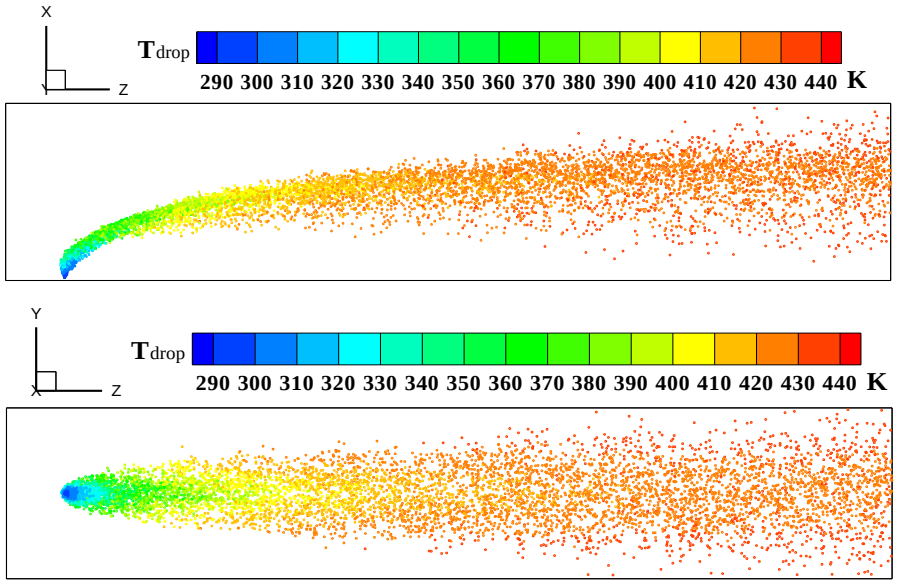

a)

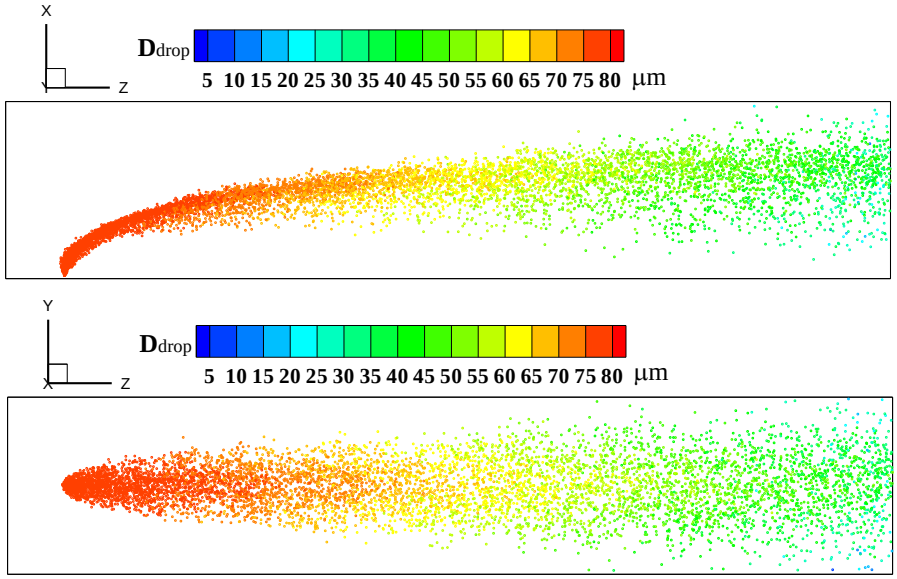

b)

Figure 16: Jet-A fuel spray simulation with initial injection temperature of 293 K a) Droplets temperature distribution along the pre-mixer b) Droplets diameter distribution along the pre-mixer projected onto X-Z and Y-Z planes (The droplet size plotted in the figures does not represent the actual droplet size)

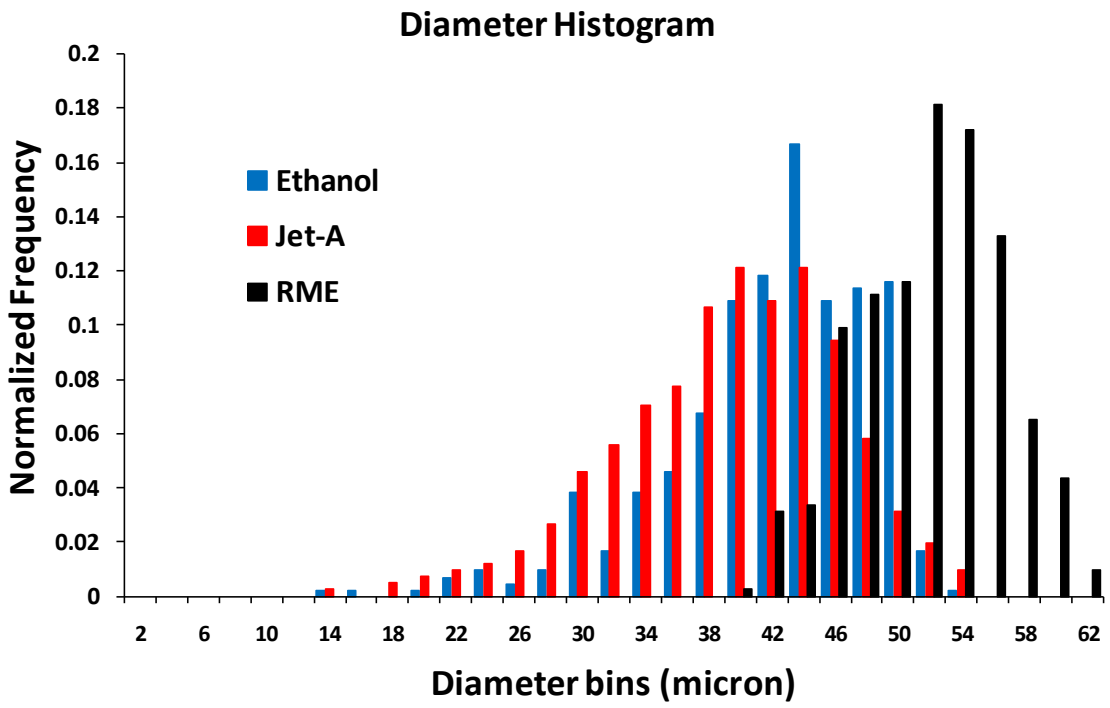

Figure 17: Droplet diameter histogram in the primary zone of interest (from plane z=28cm to z=30cm). All cases presented here are at initial injection temperature at 293 K.

5.1.5 Spray Simulation with Pre-heating of Fuel

In this section, Ethanol, Jet-A and RME are pre-heated to nearly their wet bulb temperature in order to maximize their vaporization performance. The pre-heat temperatures for each fuel are listed in Table 5. Wet bulb temperature is chosen because the droplet temperature will quickly drop down to the wet bulb temperature even when the pre-heating temperature is higher. At the wet bulb temperature, the vapor concentration at the surface is very high which will induce a high vaporization rate. Figure 18 shows SMD and surface averaged temperature of the droplets in a similar manner as reported in Figure 13 and 14. As observed from Figure 18a, SMD of jet-A droplet reduced to 18.6% of the initial diameter size near the exit of pre-mixer, while diameter of RME and ethanol droplets reduced to 31.3% and 48.2% of their initial sizes, respectively. The pre-heating of ethanol did not reduce the average droplet size exiting the pre-mixer significantly due to its low wet bulb temperature and very high latent heat of vaporization. Figure 18b shows that the average surface temperature of the droplet remains almost constant as they traverse through the pre-mixer length, which is an expected behavior.

Table 4: Summary of pre-heating temperature for all the fuels

Fuel Name	Ethanol	Gasoline	Jet-A	RME
Pre-heating Temperature (K)	323	N/A	423	583

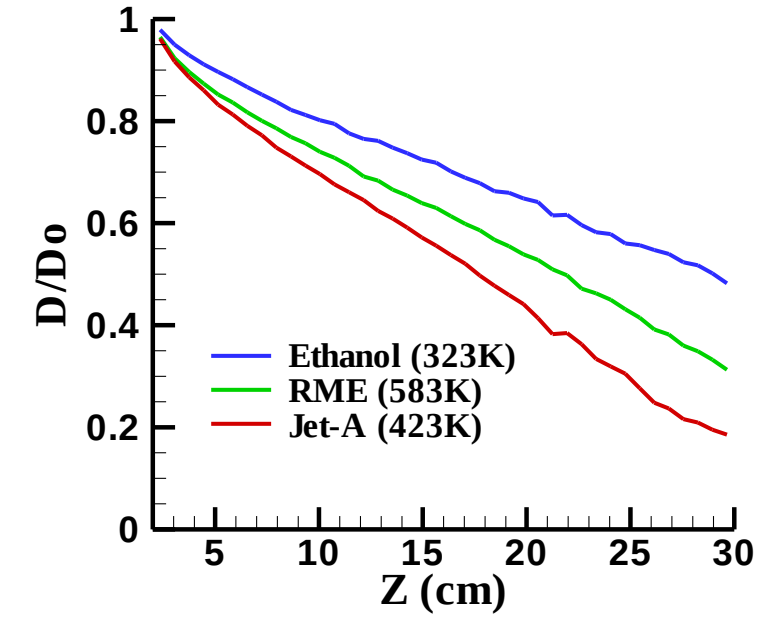

a)

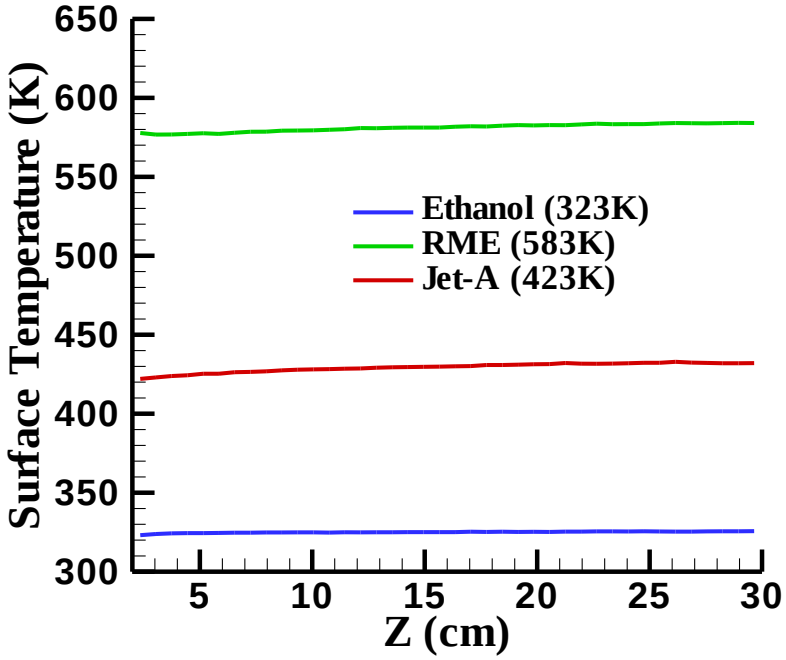

b)

Figure 18: SMD and surface averaged temperature plots of the pre-heated droplets along pre-mixer

In order to show the improvement of fuel vaporization from cold injection to pre-heated injection, the vapor mass fraction distribution for Jet-A is presented in Figure 19. Figure 19a and 19b compare the vapor mass fraction of Jet-A at the plane of symmetry (y=0) with and without pre-heating. Figure 19a shows that the vapor concentration is very small initially after injection coined as "pre-heating" period in the previous section, while Figure 19b shows a much higher vapor concentration especially near the injection port and then gradually decreases along the chamber. This is because initially the spread of the spray is very low and the vaporization rate is very high, so the fuel vapor is highly concentrated within a small spray zone. Further downstream of the pre-mixer, the fuel vapor diffuses outward from the spray center, causing a gradual decrease of the fuel vapor concentration, which aids in achieving better homogeneity. Although not shown here, RME is expected to experience similar vaporization process as jet-A. The only difference would be that the RME is expected to experience a longer pre-heating period for cold injection due to its even lower vapor pressure compared to Jet-A.

In a similar manner as reported in Figure 17, Figure 20 shows the diameter distribution histogram of pre-heated fuel droplets within the primary zone of interest. The bin range for pre-heated droplets is set the same as in Figure 17 for comparison purpose. As it can be seen from Figure 20, jet-A has a diameter range of 0 micron to 24 micron, while RME has a diameter range of 2 micron to 36 micron and ethanol has a diameter range of 12 microns to 52 microns. The jet-A vaporization performance has been significantly improved in the sense of smaller and more uniform droplet diameter distribution, while further improvement of RME and ethanol

vaporization would still be needed because the boiling temperature of RME and latent heat of ethanol are very high.

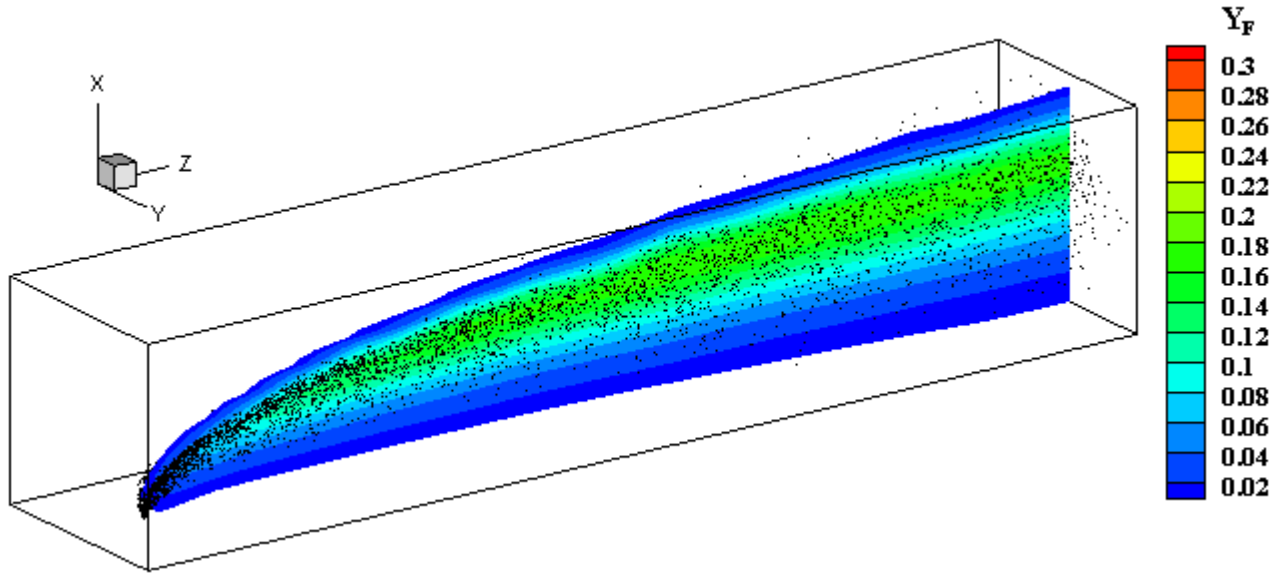

a)

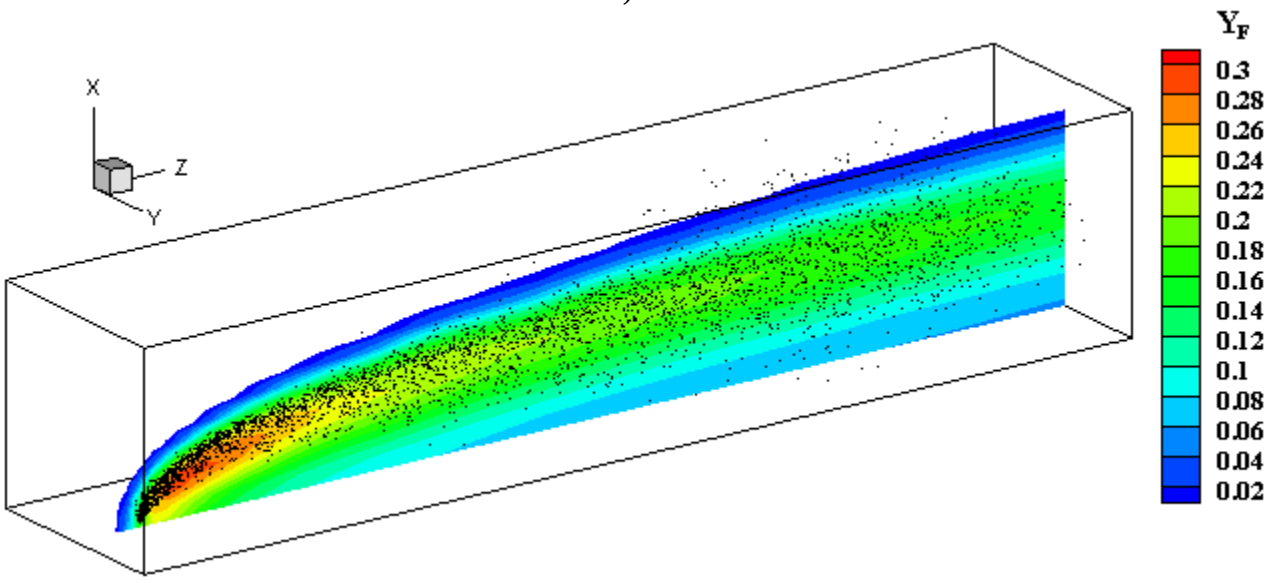

b)

Figure 19: Vapor mass fraction contour plot for jet-A fuel injection at plane of y=0, a) initial injection temperature of 293 K b) initial injection temperature of 423 K (Note: The portion of which vapor mass fraction is less than 0.02 is cutoff)

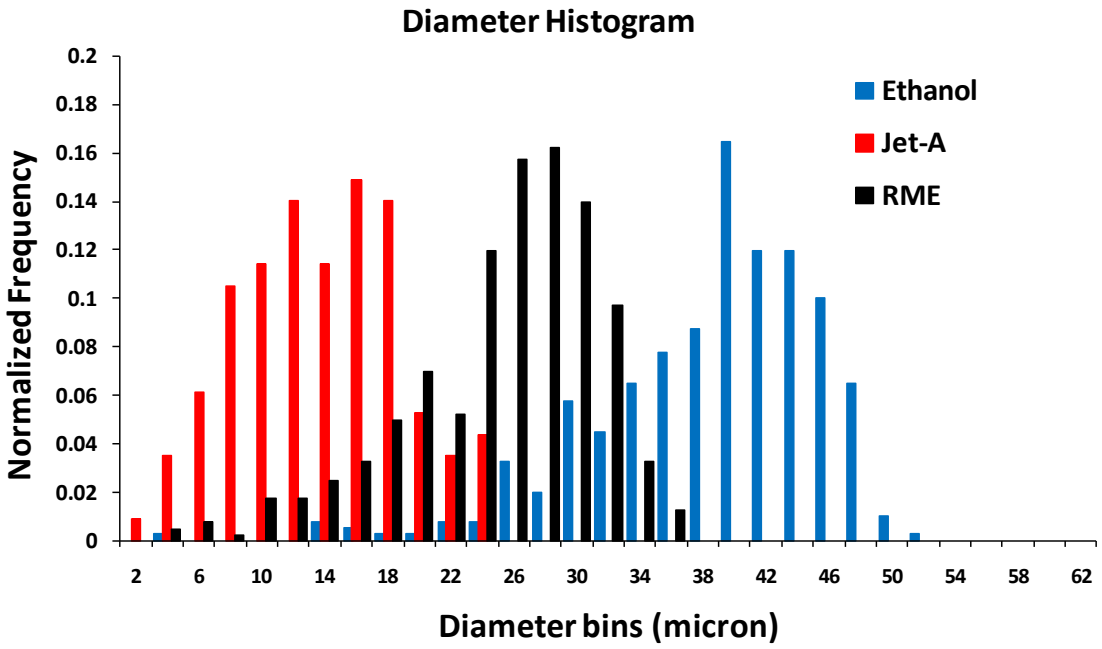

Figure 20: Droplet diameter histogram for pre-heating cases

So far, quantification of the vaporization performance for each fuel has not been done yet. To achieve this, the fuel vapor mass flow rate at the outlet is calculated since it indicates how much percentage of the liquid fuel has been vaporized through the pre-mixer chamber. The fuel vapor mass flow rate at the outlet can be calculated as:

$$\dot{m}_{fv} = \sum_{c} \rho^{c} v_{z}^{c} A^{c} \tag{5.3}$$

where index *c* represents each computational cell at the outlet. Most of the variables, such as density, pressure and temperature are all cell-centered in KIVA-4. But velocities in KIVA-4 solver are all nodal values. Thus, the cell-centered value for V_z is calculated by averaging over all the neighboring nodes for each cell.

The fuel vapor mass flow rate at the pre-mixer outlet is plotted for all the fuels with Figure 21a showing the results of cold injections and Figure 21b showing the results of pre-heated injections. Since gasoline is fully vaporized at the pre-mixer exit, the vapor mass flow rate at various cross-sectional planes were monitored and found that gasoline is approximately fully vaporized at z=22cm, which is 8cm away from pre-mixer exit. For cold injections, the vapor mass flow rate for ethanol, jet-A and RME are 0.8 g/s, 0.82 g/s and 0.7 g/s, meaning 87%, 89% and 76% of liquid fuels have been vaporized through the pre-mixer, respectively. For pre-heated injections, the vapor mass flow rate for ethanol, jet-A and RME are 0.82 g/s, 0.92 g/s and 0.9 g/s, meaning 89%, 100% and 98% of liquid fuels have been vaporized through the pre-mixer, respectively. Thus, pre-heating the fuels improved the vaporization performance for ethanol, jet-A and RME by 2%, 11% and 22%, respectively. The improvement for ethanol is very small since the pre-

heating temperature is only 30 K higher than cold injection temperature. Its vaporization performance could be further improved by increasing the spray cone angle which will be discussed in later sections.

To quantify the homogeneity of the vapor mass fractions in the current application in order to provide reference for future improvement, a so-called “unmixedness” parameter is calculated at the pre-mixer exit plane, which is the cross-section plane of z=300mm. The unmixedness parameter is defined as the standard deviation of vapor mass fraction divided by the averaged vapor mass fraction within the plane of interest. The ideal value of unmixedness should be zero, meaning perfect homogeneity. The values of unmixedness for cold injection of gasoline, ethanol, jet-A and RME are 1.1, 1.08, 1.1 and 1.2, respectively. And the values of unmixedness under pre-heated injection for ethanol, jet-A and RME are 1.14, 1.16 and 1.12, respectively. This shows that the extent of inhomogeneity for all the fuels both under cold injection and pre-heated injection are very similar. Although the standard deviation of the preheated droplets increases, so does the average value since more vapor fraction is generated by the preheated droplets. This gives similar normalized value of unmixedness of vapor mass fraction as in the unheated case.

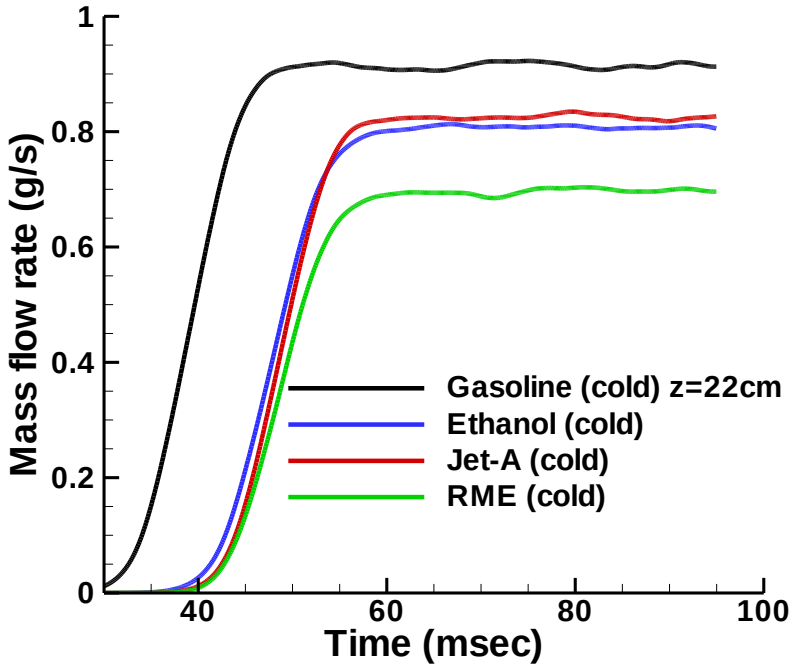

a)

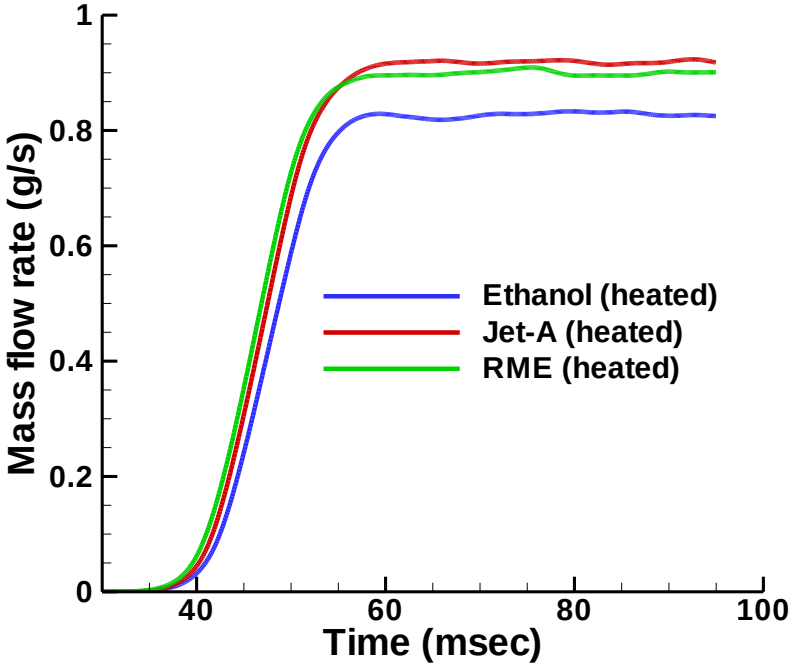

b)

Figure 21: Fuel vapor mass flow rate monitored at the pre-mixer outlet a) cold injection b) pre-heated injection

5.2 Modified Drag Model with Stefan Flow Correction

In this section, a modified drag model was implemented into KIVA-4 code to compare with the original drag model implemented in KIVA-4. This drag model incorporated the Stefan flow correction for regimes where strong evaporation will reduce the drag coefficient for the vaporizing droplet as proposed by Renksizbulut and Yuen (1983). This drag model is valid for low droplet Reynolds number in the range of $Re_d<30$ [Sirignano (1999)]. For current pre-mixer applications, the droplet Reynolds number is very small [O(10) initially], and hence this modified drag model is very suitable. The new drag coefficient is given as:

$$C_D = \frac{24}{\mathrm{Re}_d(1+B_d)} \tag{5.4}$$

where B_d is the Spalding transfer number.

5.2.1. Crossflow Results and Discussions

To show the change of the droplets dispersion caused by the Stefan flow correction on the droplet drag modeling the same computational conditions are maintained throughout the simulations using the corrected drag model. Jet-A was used to show the difference. Figure 22a shows the droplets dispersion using the previous drag model, while Figure 22b shows the droplets dispersion using the corrected drag model. A difference can be seen in droplets dispersion between two drag models since Figure 22b shows that a large portion of the spray hits the wall with the corrected drag model. The reason is quite obvious since droplets with reduced drag would penetrate further with the same initial injection velocity. Since spray impact on the wall is not desired the injection velocity was then lowered to 2m/s. The spray dispersion is

shown in Figure 22c. As seen from Figure 22c, it can be seen that the spray is not well dispersed as the previous results since the injection velocity is lowered. In order to enhance the heat transfer between the two phases to improve the fuel vaporization performance, one needs to fully take advantage of the pre-mixer's space and spread the spray as much as possible. Thus, the spray cone angle was gradually increased until a value was found where the spray would not hit the wall. The maximum spray cone angle found was 140° under current spray conditions. Figure 23a and Figure 23b show the droplets dispersion projected onto the X-Z plane and Y-Z plane, respectively. The Y-Z plane projected view shows that the spray is nearly impinging onto the wall which constrains the spray cone angle within 140°. From Figure 23, it can also be seen that the droplets become very sparse downstream in the pre-mixer due to complete evaporation of most of the droplets droplets.

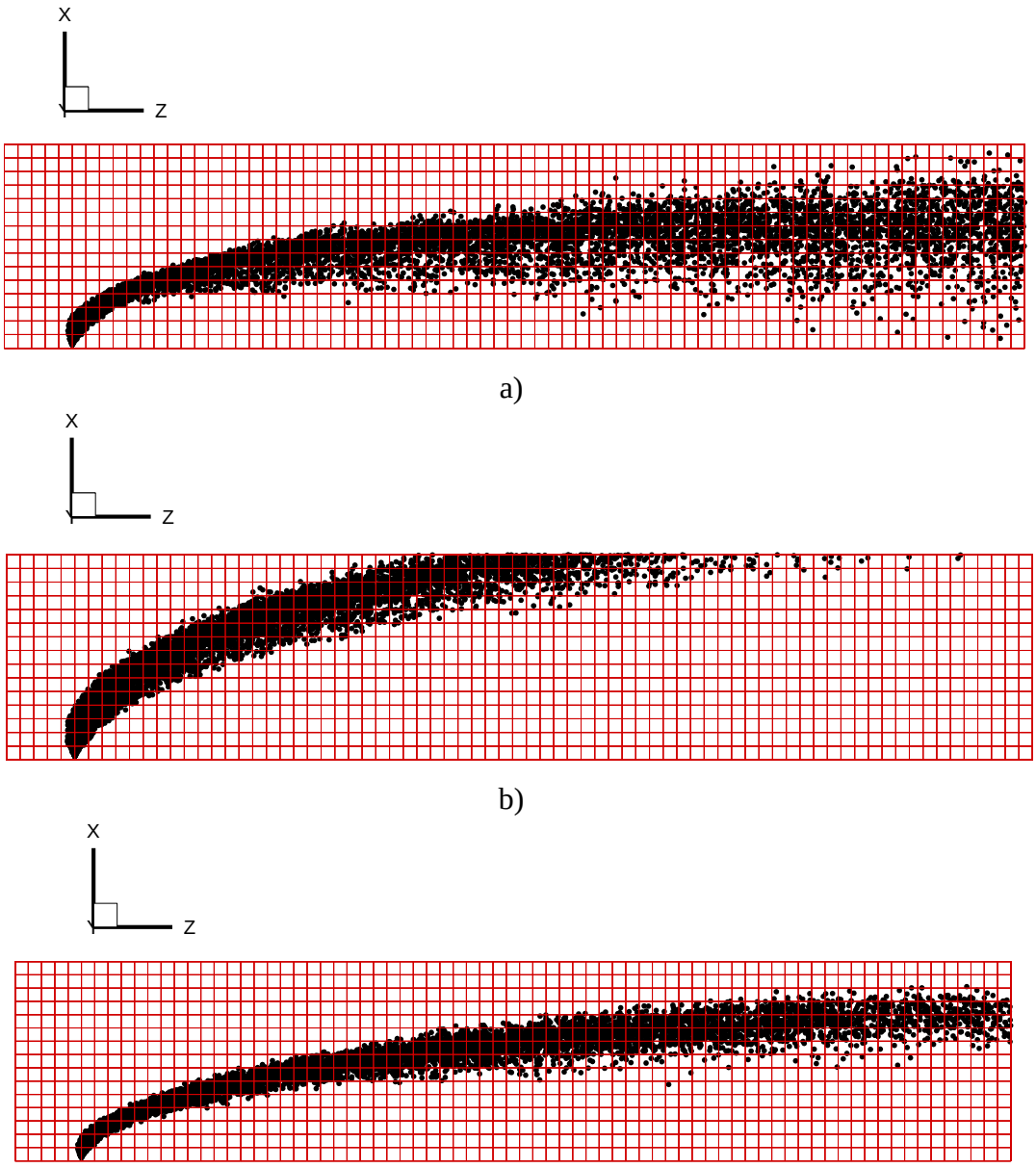

Figure 22: Jet-A spray dispersions a) Old drag model with 3.5m/s injection velocity b) Modified drag model with 3.5m/s injection velocity c) Modified drag model with 2m/s injection velocity

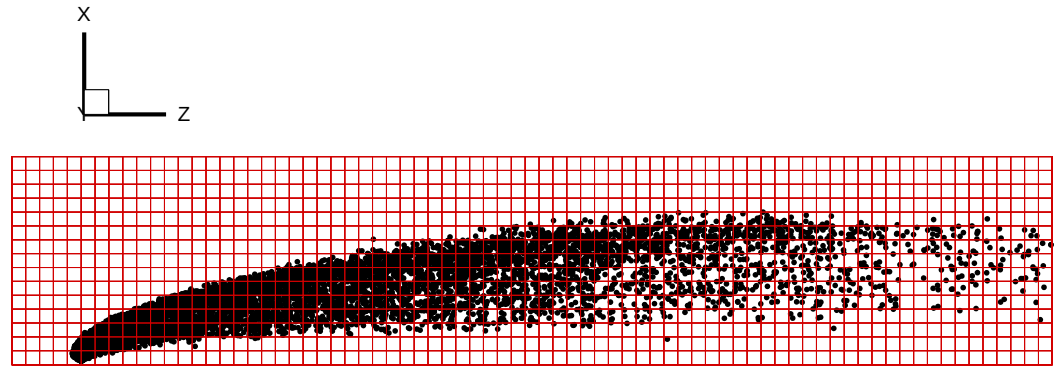

a)

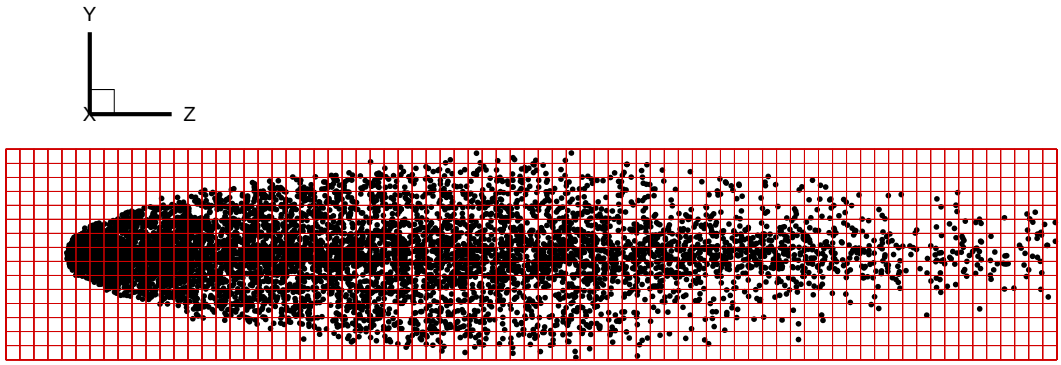

b)

Figure 23: Jet-A spray dispersions with the spray cone angle of 140° and 2m/s injection velocity a) projection view onto XZ plane b) projection view onto YZ plane

To quantitatively show the advantage of large spray cone angles over small spray cone angles, the fuel vapor mass flow rate was calculated at the outlet for all the fuels at both spray cone angles. The vapor mass flow rate of gasoline was monitored at various cross-sections since it was expected to achieve complete vaporization much earlier than other fuels, and it was found to achieve complete vaporization approximately 22cm, which is 8cm away from the pre-mixer exit. Figure 24a and 24b shows the fuel vapor mass flow rate at the spray cone angle of 70° and 140°, respectively. For spray cone angle of 70°, the vapor mass flow rate for ethanol, jet-A and RME are 0.85 g/s, 0.91 g/s and 0.81 g/s, meaning 92%, 99% and 88% of liquid fuels have been vaporized through the pre-mixer, respectively. For spray cone angle of 140°, the vapor mass flow rate for ethanol, jet-A and RME are 0.9 g/s, 0.92 g/s and 0.88 g/s, meaning 98%, 100% and 97% of liquid fuels have been vaporized through the pre-mixer, respectively.

Thus, by increasing the spray angle from 70° to 140°, the vaporization performance for ethanol and RME is improved by 6% and 9%, respectively. Since jet-A fuel already achieved complete vaporization at 70° of spray cone angle right at the pre-mixer outlet, it was expected that jet-A fuel can be fully vaporized before reaching the pre-mixer exit at the higher spray cone angle of 140°.

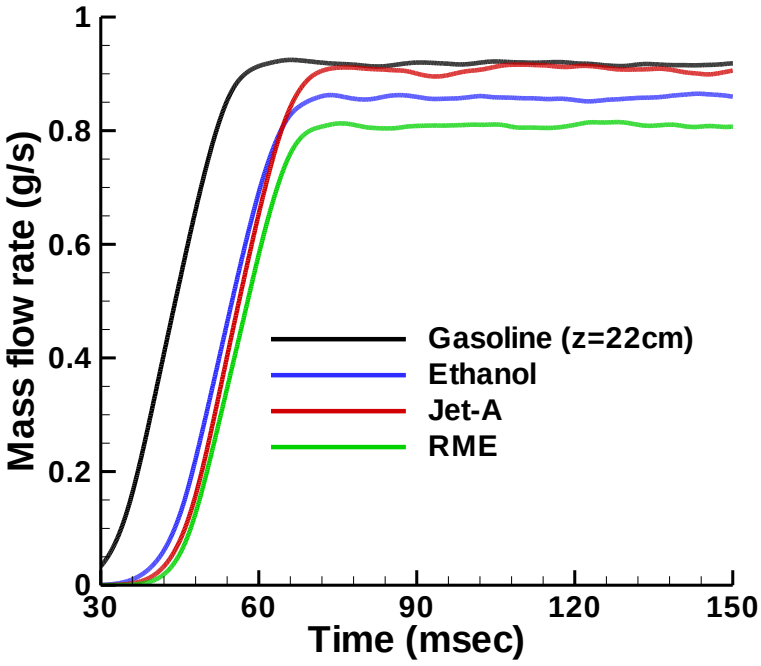

a)

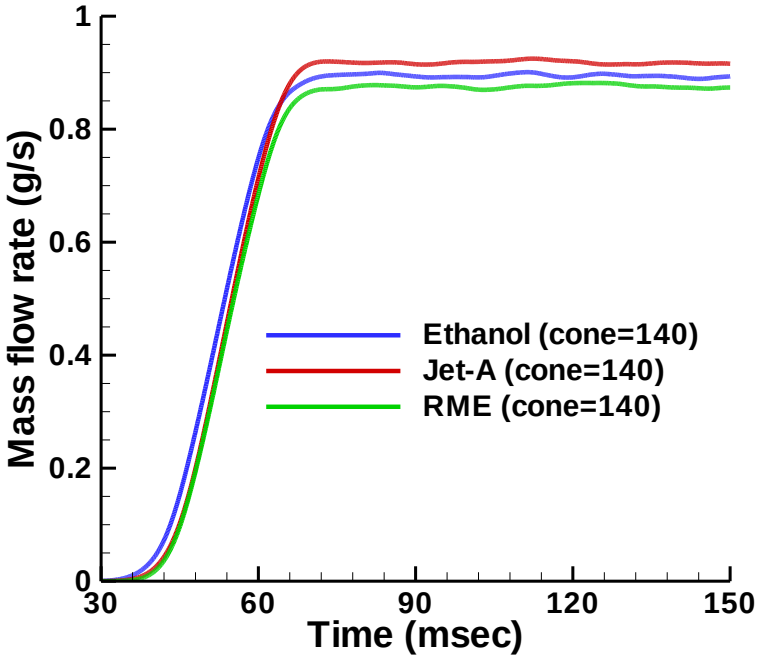

b)

Figure 24: Fuel vapor mass flow rate monitored at the pre-mixer outlet a) spray cone angle of 70° b) spray cone angle of 140°

Another aspect is to see how the spray dispersion levels have changed the droplet size and number distribution along the pre-mixer. The normalized SMD, total number of droplets and average surface temperature are calculated for each zone and plotted along the z-axis, which are shown in Figure 25. As it can be seen, the SMD for all the fuels are relatively lower at the larger spray cone angle of 140° compared to the SMD at the smaller spray cone angle of 70°, which is expected due to the more efficient heat transfer between the two phases at higher spray angle. Also, direct evidence is from the average surface temperature of the spray, which is plotted in Figure 25c for both spray cone angles. The average surface temperature is relatively higher at the larger spray cone angle, leading to a relatively higher vaporization rate. From Figure 25a, it was noticed that the normalized SMD of all the fuels did not decrease to zero. For example, the normalized SMD for RME at spray cone angle 140° decreased from 1 to 0.5 along the pre-mixer, which is still a relatively large value. However, from Figure 25b, the total number of droplets decreased dramatically, meaning that most of the droplets have been vaporized when reaching the pre-mixer exit. Even though the SMD of the spray leaving the pre-mixer is still relatively large most of the liquid fuel has been fully vaporized through the pre-mixer. One interesting phenomenon shown in Figure 25a is that the diameter reduction curve for ethanol crossed over with Jet-A for both spray cone angles. The diameter regression rate for Jet-A exceeded ethanol at some location. This can be explained as follows: near the injection port, both fuels are injected at the same temperature at which time ethanol has a vapor pressure around 6 kPa while Jet-A is 0.3 kPa . So ethanol has a much higher vaporization rate compared to Jet-A initially. However, since ethanol has a much higher latent heat of vaporization than Jet-A, the temperature rise of ethanol is much lower than Jet-A, where Figure 25c shows that Jet-A quickly reached its wet bulb

temperature, which is much higher than that of ethanol. The vapor pressure of Jet-A at its wet bulb temperature is around 40 kPa, which is much higher than the vapor pressure (26kPa) of ethanol at its wet bulb temperature. This explains why the vaporization rate of Jet-A would exceed ethanol.

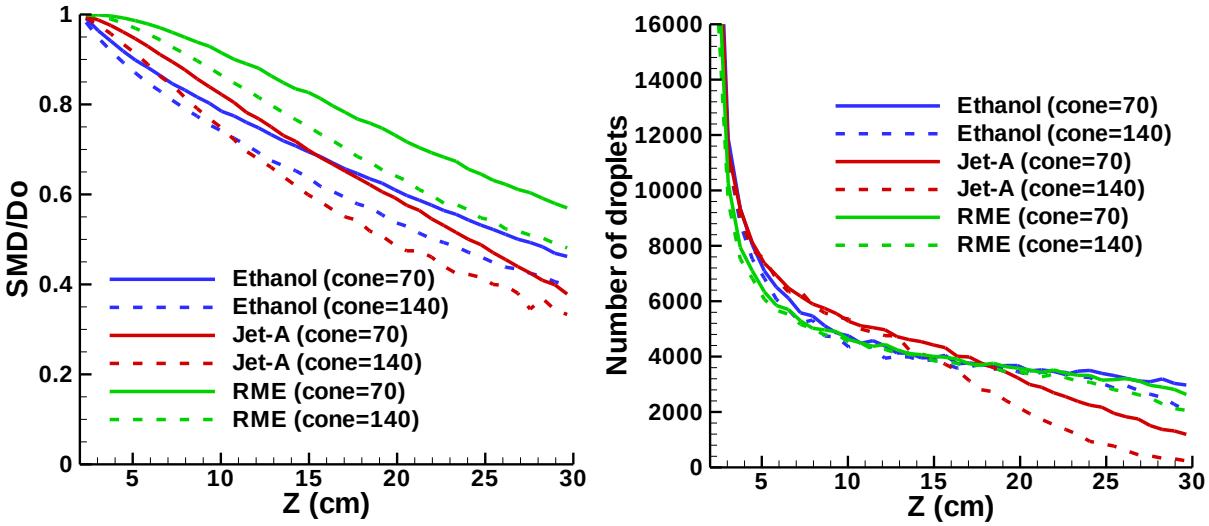

a) b)

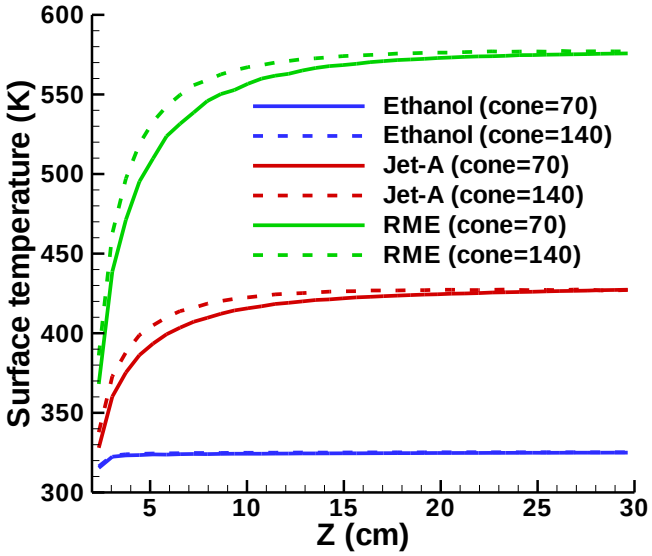

c)

Figure 25: Compare spray characteristics between spray cone angle of 70° and 140° a) SMD/D_o b) Number of droplets c) Average surface temperature

5.2.2. Co-flow Results and Discussions

So far, crossflow injections of different liquid fuels into a rectangular pre-mixer has been studied extensively in various aspects, such as droplet size and number distributions, droplets dispersion, vaporization performance, improvement of vaporization performance by pre-heating the liquid fuels prior to their injection, etc. In this section, in order to show the advantage of crossflow injection method, results are presented for the simulation of another common injection method, co-flow injection where the liquid fuels are injected co-axially with the air into the pre-mixer. All the parameters for co-flow injection are maintained to be the same as crossflow injection for later comparisons in next section.

First, in order to make sure that the spray will not hit the wall at the same spray cone angles as crossflow injection, the co-flow injection at both spray cone angles are simulated and the corresponding droplets dispersions are shown in Figure 26. RME was used to represent the fuel dispersions for co-flow injection. Figure 26a and 26b show the projected view of droplets dispersion onto X-Z plane at spray cone angle of 70° and 140°, respectively. From Figure 26b, the spray is almost hitting the wall, showing a similar dispersion level as crossflow injection at the large spray cone angle of 140°.

Next, the fuel vapor mass flow rate is presented to show the vaporization performance for each fuel. Figure 27a and 27b shows the results for spray cone angle of 70° and 140°, respectively. For spray cone angle of 70°, the vapor mass flow rate for ethanol, jet-A and RME are 0.79 g/s, 0.84 g/s and 0.69 g/s, meaning 85%, 91% and 75% of liquid fuels have been vaporized through

the pre-mixer, respectively. For spray cone angle of 140°, the vapor mass flow rate for ethanol, jet-A and RME are 0.86 g/s, 0.9 g/s and 0.81 g/s, meaning 93%, 98% and 88% of liquid fuels have been vaporized through the pre-mixer, respectively. Thus, by increasing the spray angle from 70° to 140°, the vaporization performance for ethanol, jet-A and RME have been improved by 8%, 7% and 13%, respectively. Since gasoline quickly reached complete vaporization at the pre-mixer exit, its vapor mass flow rate is only plotted at the 70° spray cone angle, where it shows that 97% of liquid gasoline has been vaporized at 22cm.

To complete the quantitative study on co-flow injections, the normalized SMD and total number of droplets are also plotted, which are shown in Figure 28. As expected, the SMD for all the fuels are relatively lower at the larger spray cone angle of 140° compared to the SMD at the smaller spray cone angle of 70°. The average surface temperature was also seen to be relatively higher at the larger spray cone angle, leading to a relatively higher vaporization rate.

So far, most of the fuels have achieved very good vaporization performance at the larger spray cone angle of 140° except RME, for which the vaporization still needs to be improved. Thus, pre-heating of RME has been done to improve its vaporization performance. A series of pre-heating temperatures are tested and found that pre-heating the fuel to 493K allowed RME to achieve complete vaporization when reaching the pre-mixer exit. To show the effects of different pre-heating temperatures on RME's vaporization performance and droplet size distributions, the results at three different initial injection temperatures are compared and shown in Figure 29. The RME vapor mass flow rate with pre-heating temperature of 393k and 493K are 0.86 g/s and 0.91

g/s, meaning 93% and 99% of liquid RME have been vaporized through the pre-mixer, respectively. Comparing this with 88% vaporization performance seen without pre-heating, an average of 5% improvement in vaporization performance per 100 K increase in initial injection temperature was seen. To visualize the effect of pre-heating on the droplet vaporization, the fuel vapor mass fraction contour plot is presented for all three levels of injection temperatures in Figure 30. As shown in Figure 30a, one can see that the vapor mass fraction is extremely lower near the injection port where the average droplet temperature is very low indicating an extremely low vapor pressure (O(1.0E-3) pa). By pre-heating the fuel to 493K prior to injection, the vapor mass fraction near the injection port is highly improved due to the higher fuel vapor pressure (O(1000) pa) at higher temperatures.

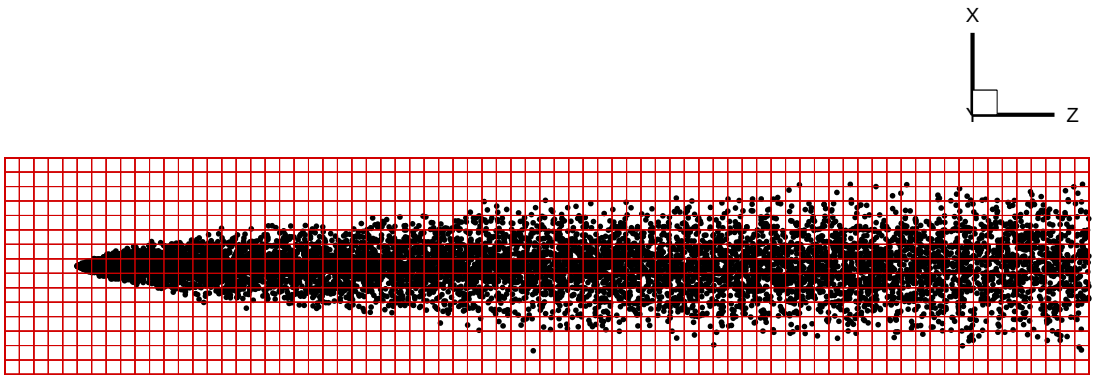

a)

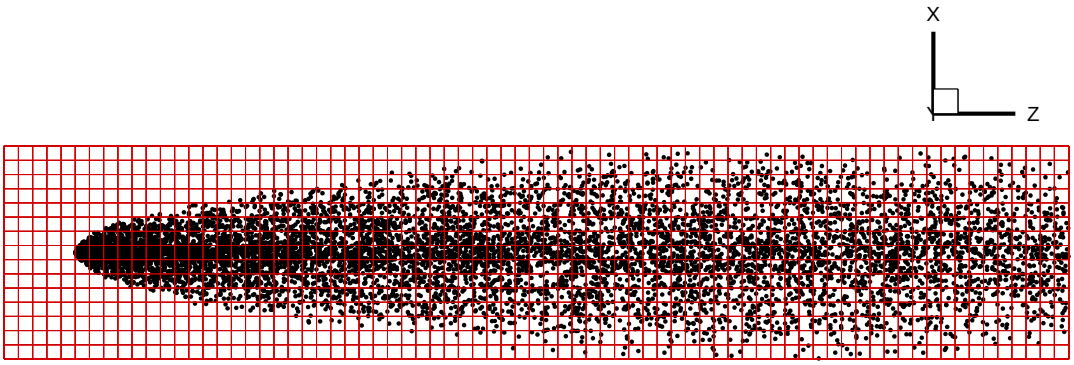

b)

Figure 26: RME spray dispersions for co-flow injections a) spray cone angle of 70° b) spray cone angle of 140°

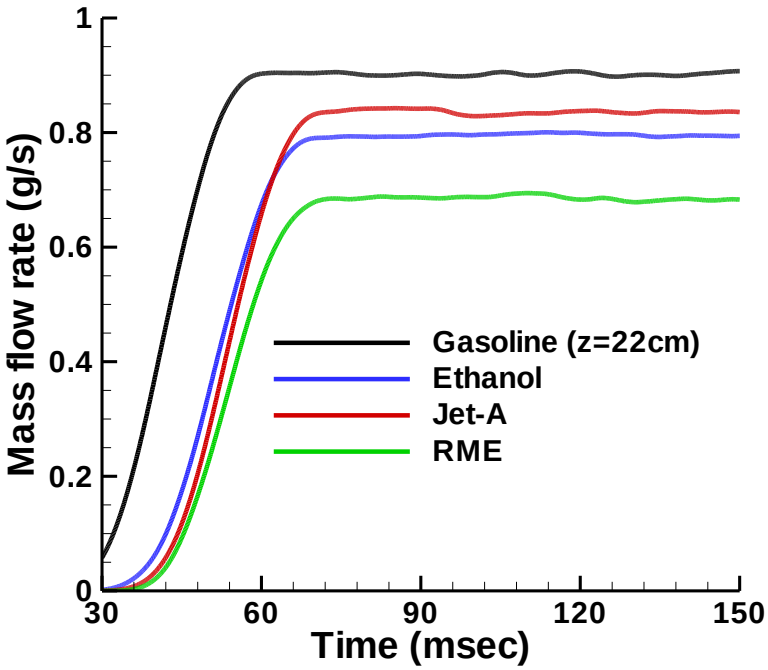

a)

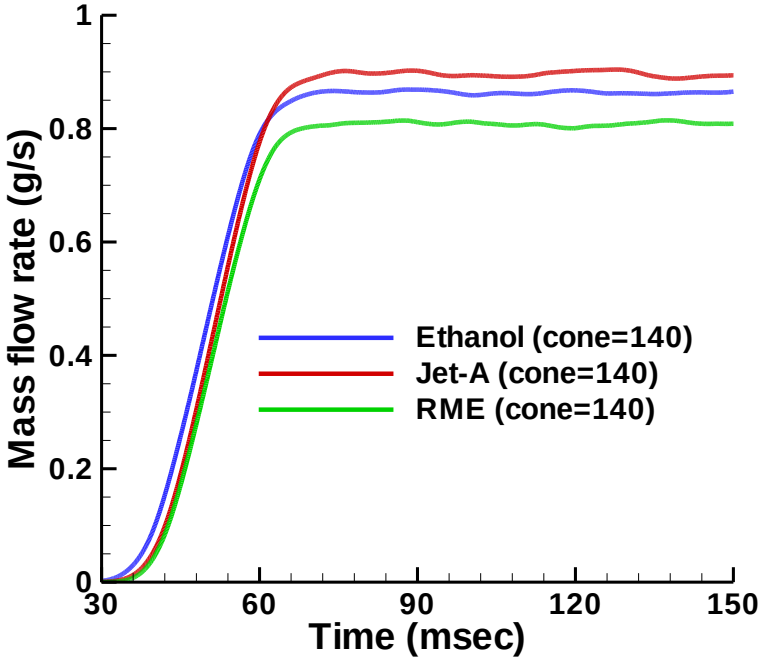

b)

Figure 27: Fuel vapor mass flow rate monitored at the pre-mixer outlet a) spray cone angle of 70° b) spray cone angle of 140°

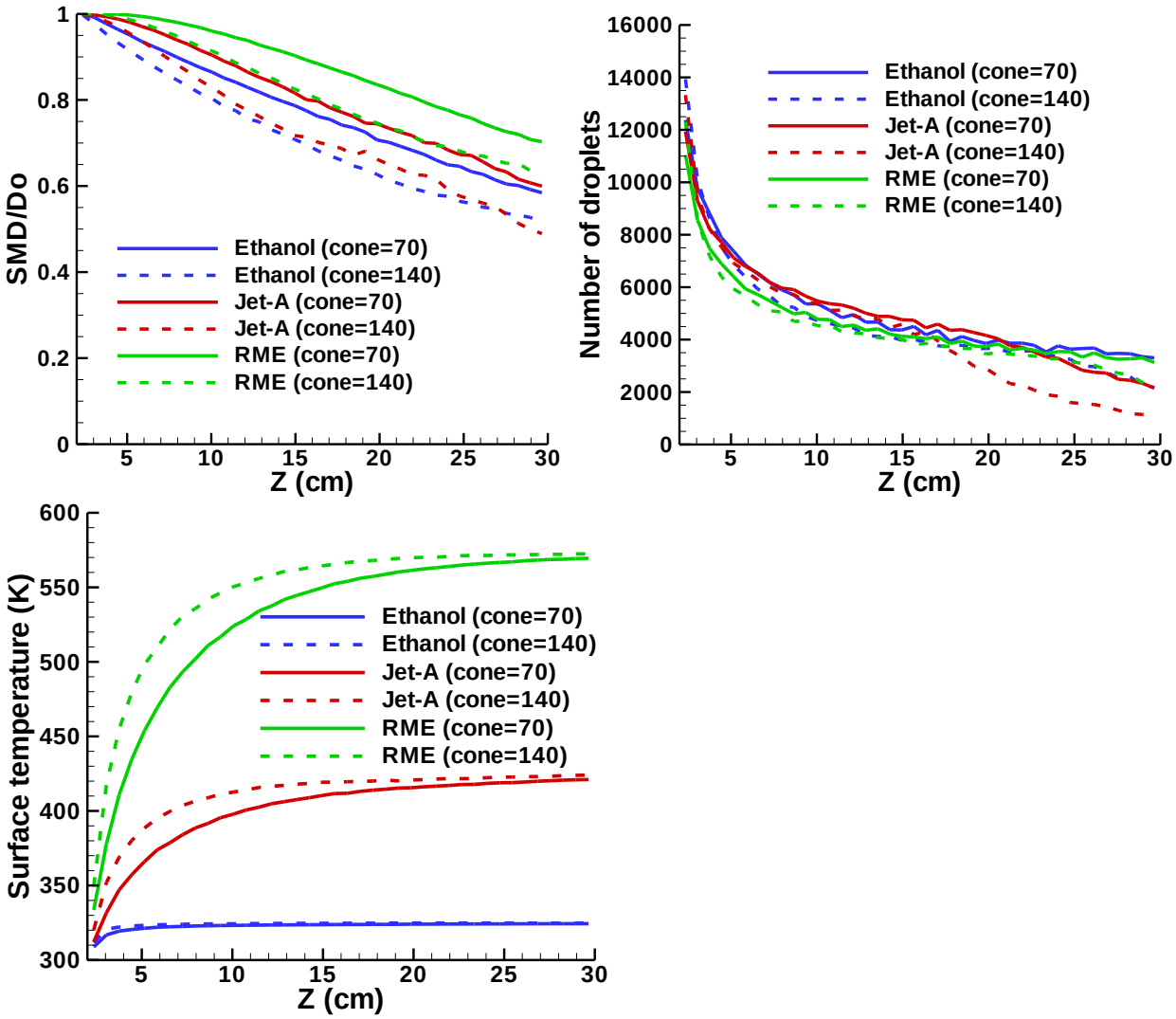

Figure 28: Compare spray characteristics between spray cone angle of 70° and 140° a) SMD/D_o b) Number of droplets c) Average surface temperature

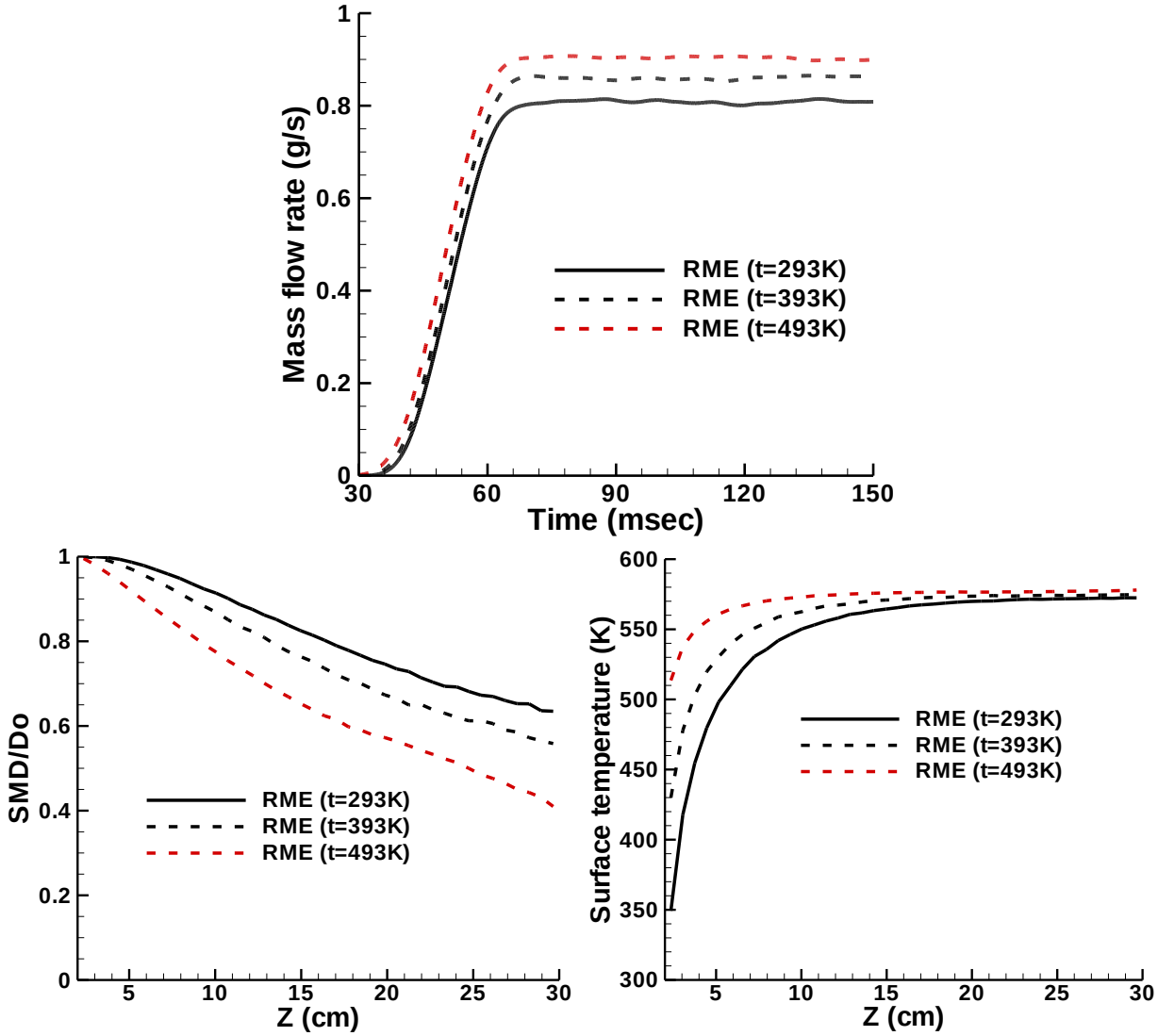

Figure 29: Compare RME spray characteristics at three different injection temperatures a) fuel vapor mass flow rate at pre-mixer outlet b) SMD/D_o c) Average surface temperature

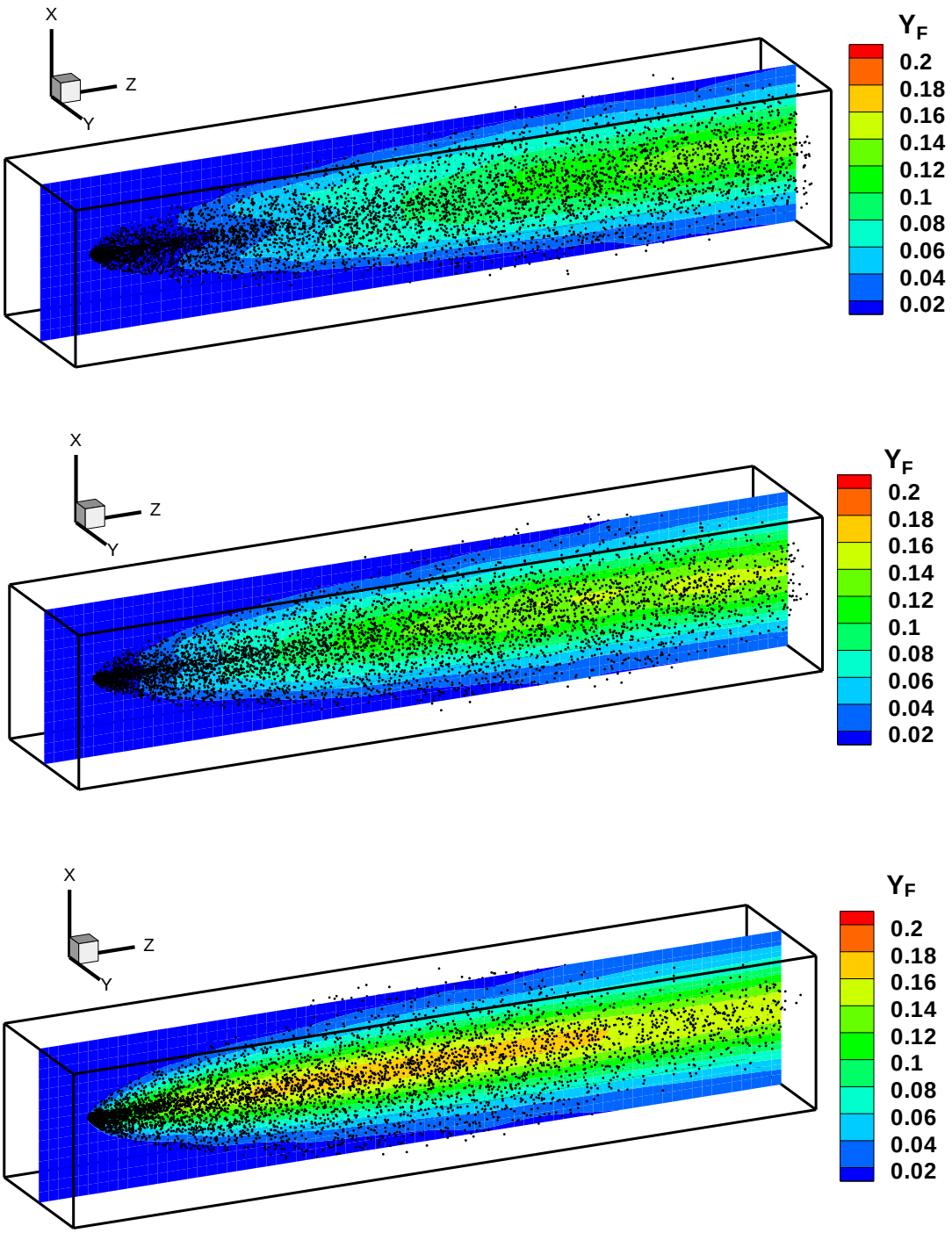

Figure 30: RME fuel vapor mass fraction contour plot at different injection temperatures a) 293K, b) 393K, c) 493K

5.2.3 Compare Crossflow Performance with Co-flow Performance

So far, the crossflow injections using the Stefan flow corrected drag model and studied the co-flow injections under the same spray conditions have been looked at. In this section, the vaporization performance for crossflow injection and co-flow injection are compared at the optimum spray cone angle of 140° for all the fuels except gasoline, which is fully vaporized far before reaching the pre-mixer exit for both injection methods. The fuel vapor mass flow rate is plotted in Figure 31, which shows crossflow injection is better than co-flow injection in vaporizing the fuels under current pre-mixer configuration. The vaporization performance for co-flow injections of ethanol, jet-A and RME are 93%, 98% and 88%, respectively; for crossflow, they are 98%, 100% and 97%, respectively. For RME, crossflow injection achieved 97% vaporization performance, which is 9% higher than co-flow injection, showing that pre-heating is not necessary for crossflow injection.

The direct evidence of better vaporization performance using crossflow injection methods can be observed from Figure 32b. It shows the average droplet surface temperature is higher for crossflow than co-flow, which results in a relatively higher vapor pressure and then promotes the droplet vaporization rate. For ethanol, the vaporization performance is similar for both injection methods because of its low wet bulb temperature. As explained earlier, the latent heat of vaporization for ethanol is very high such that its wet bulb temperature is very low. Thus, even though crossflow is more efficient in transferring the heat from the gas phase to the droplet phase, the droplet temperature rise is only slightly higher for crossflow injection than co-flow injection such that the vaporization performance is similar. For jet-A, there is little difference in the

vaporization performance between the two injection methods because jet-A achieves complete vaporization before reaching pre-mixer exit for crossflow injection. Thus, in order to show the advantage of crossflow than co-flow injection in vaporizing jet-A, a comparison is need to compare Jet-A's vapor mass flow rate at a different cross-section other than the outlet. However, the results from RME clearly show the advantage of crossflow injection than co-flow injection in vaporizing the liquid fuel.

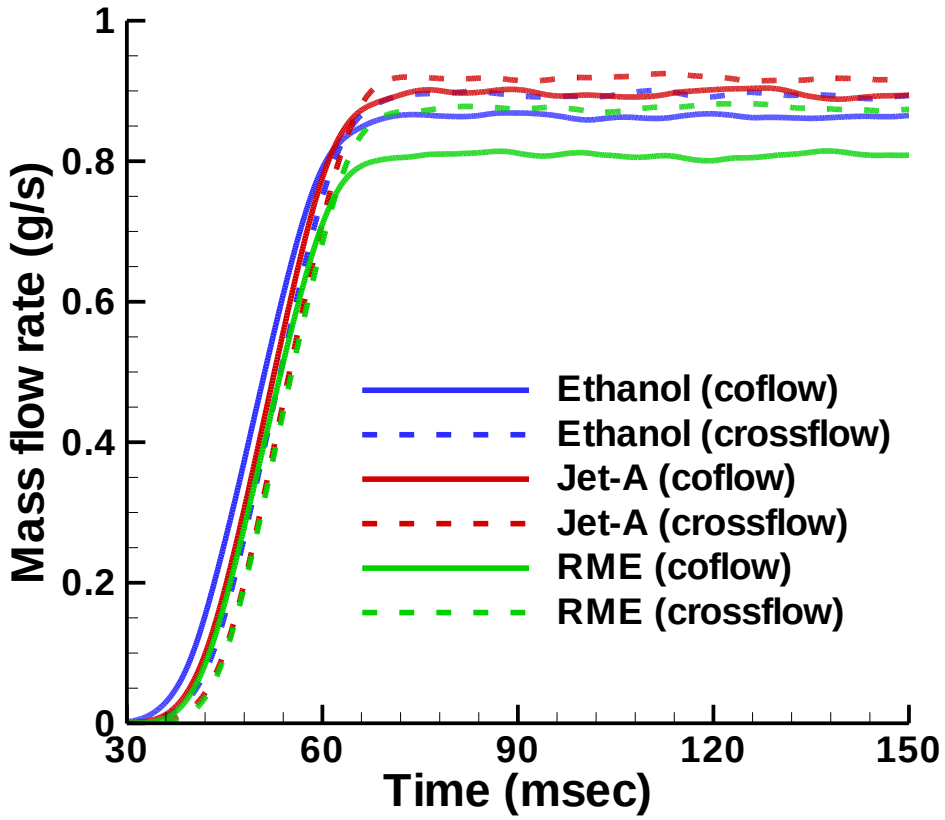

Figure 31: Compare the vaporization performance between co-flow injection results and crossflow injection results

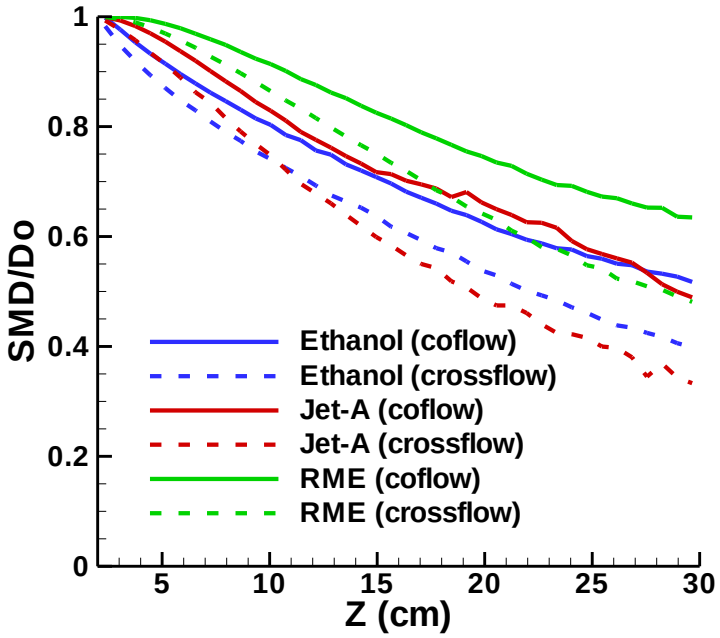

a)

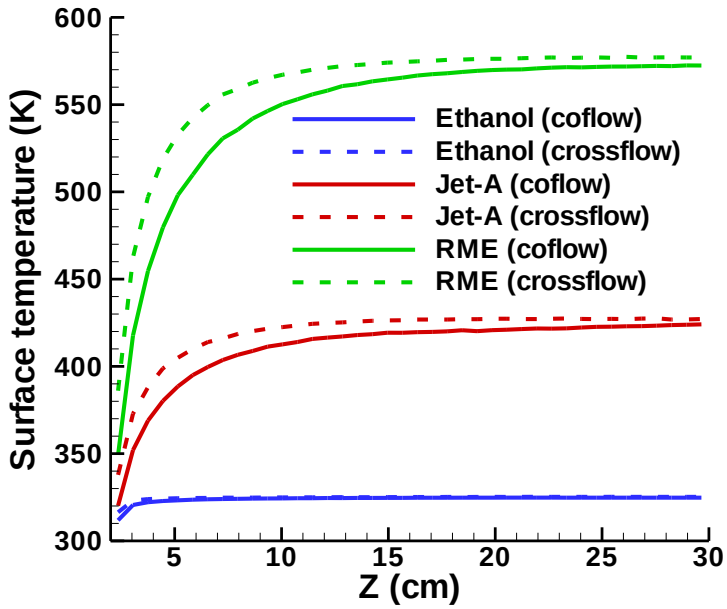

b)

Figure 32: Compare the spray characteristics between co-flow injection results and crossflow injection results a) SMD/Do b) Average surface temperature

5.3 Parametric Study of Crossflow Vaporization Performance

So far, it has been seen that crossflow could achieve better vaporization performance than co-flow. Thus, in order to have a comprehensive view of crossflow vaporization performance dependencies on different parameters, such as inlet air temperature, momentum flux ratio between fuel and air, several different sets of simulations were conducted in this section. Jet-A was chosen to show its fuel vaporization performance characteristics.

Two important dimensionless parameters are defined here,

1. Fuel/air momentum flux ratio is defined as, $qFa=(\rho_F \times u_F^2)/(\rho_{air} \times u_{air}^2)$
2. Fuel air temperature difference in dimensionless form, $T_d=(T_{air}-T_f)/T_f$

The fuel vaporization performance is clearly dependent on both parameters defined above. Thus, in order to study the separate effects, the fuel vaporization performance needed to be compared at a fixed fuel/air momentum flux ratio for different inlet air temperatures, and vice versa. To fix the fuel/air momentum flux ratio at different inlet air temperatures the fuel injection velocity is varied at different inlet air temperatures to compensate the change of the air density. Meantime, since the inlet air mass flow rate will also change due to density change at different temperatures, the fuel injection mass flow rate is also varied in order to maintain a constant stoichiometric ratio between the air and the fuel. To be consistent with previous studies, air/fuel stoichiometric ratio is fixed at 17.3, which gives the equivalence ratio: 14.7/17.3=0.85. For jet-A, the fuel/air momentum flux ratio is 73.3 when inlet air temperature is 800k and fuel injection velocity is 2m/s, which are the primary parameters used in previous studies.

Table 5: Summary of jet-A parametric studies

Inlet air temperature (K)	Inlet air velocity (m/s)	Inlet air mass flow rate (g/s)	Fuel injection mass flow rate (g/s)	Fuel injection velocity (m/s) qFa=33.3	Fuel injection velocity (m/s) qFa=73.3	Fuel injection velocity (m/s) qFa=113.3
400	10	31.77	1.84	1.91	2.83	3.52
450	10	28.1	1.63	1.8	2.67	3.32
500	10	25.4	1.47	1.71	2.53	3.15
550	10	23.1	1.34	1.63	2.41	3
600	10	21.1	1.22	1.56	2.31	2.87
650	10	19.5	1.13	1.5	2.22	2.76
700	10	18.1	1.05	1.44	2.14	2.66
800	10	15.88	0.92	1.35	2	2.5

Table 5 summarized all the important parameters used for the subsequent simulations at different inlet air temperatures and fuel/air momentum flux ratios. The inlet air temperature is varied from 400k to 800k with 50k increment, and fuel/air momentum flux ratio is fixed at three different levels, 33.3, 73.3 and 113.3. Both parameters are varied in a relatively large range in order to clearly show their influence on the fuel vaporization performance.

Figure 33-36 plots the fuel vapor mass fraction along the pre-mixer channel at different inlet air temperatures from 400k~700k, where the x-axis represents dimensionless streamwise location, defined as *(x-d)/L*, where *d* is the start of the injection point and *L* is the total vaporization length. At each temperature, one can see that the fuel vapor mass fraction increases when increasing the fuel/air momentum flux ratio. And the fuel vapor mass fraction reached a maximum value of 0.016, 0.037, 0.048 and 0.053 at the premixer exit from 400k to 700k inlet air temperatures. Since air-fuel stoichiometric ratio is fixed at 17.3, the maximum fuel vapor mass fraction would be 1/(1+17.3)=0.055, which is evident from Figure 36 where it shows jet-A almost completely vaporizing at the pre-mixer exit.

To summarize the fuel vaporization performance at different conditions, a plot was generated for the vaporization performance versus the dimensionless temperature, T_d at three different fuel/air momentum flux ratios, which is shown in Figure 37a. By curve fitting the data at *qFa*=73.3, the fuel vaporization performance can be expressed as a function of the dimensionless temperature, T_d:

$$Vaporization\ performance\% = 58.043 * \ln(T_d) + 79.791 \tag{5.5}$$

This functional form shows that the vaporization performance is a logarithmic function of the dimensionless supplying air temperature with continuously decreasing slope. It makes sense because the gradient of improving the vaporization performance by increasing air temperature must continuously decrease until the fuel fully vaporizes, where the upper limit of vaporization performance is 100%.

As seen from both Figure 36 and Figure 37a, the effect of fuel/air momentum flux ratio on the fuel vaporization performance is relatively weak since jet-A almost completely vaporized at such high supplying air temperature. In order to compensate the effect of momentum flux ratio on fuel vaporization performance and fit the data onto the previous curve-fitted function, a weighting coefficient is applied to all the scattered data, which is expressed as: $[(qFa)/(qFa)_{ref}]^{A}$, where $(qFa)_{ref}$ is the reference fuel/air momentum flux ratio, chosen to be 73.3 in this case, and the power coefficient A is adjusted such that a best fit curve could be generated. By tuning A to be 0.21, all the scattered data fit quite well with the fitting function, which is plotted in Figure 37b. Thus, the jet-A vaporization performance (%) can be summarized as a function of dimensionless supplying air temperature, T_d, and fuel/air momentum flux ratio, qFa:

$$Vaporization\ performance\% = [58.043 \ln(T_d) + 79.791] * [qFa/73.3]^{0.21} \quad (5.6)$$

From the summarized function, one can approximate the Jet-A's total vaporization performance at specified inlet air temperatures and fuel/air momentum flux ratios. As mentioned previously, the asymmetric crossflow injection and protection of the spray cone will result in some levels of inhomogeneity of the fuel vapor and air mixture, which can be shown in contour plots of either fuel vapor mass fraction or fuel vapor phase local equivalence ratio:

{equivalence ratio}=14.7/[1.0/vapor_mass_fraction-1], where 14.7 is the air/fuel stoichiometric ratio.

Figure 38 shows the contour plots of the fuel vapor phase local equivalence ratio, which is consistent with the previous contour plot of fuel vapor mass fraction. It shows higher level of vapor concentration near the center of plane.

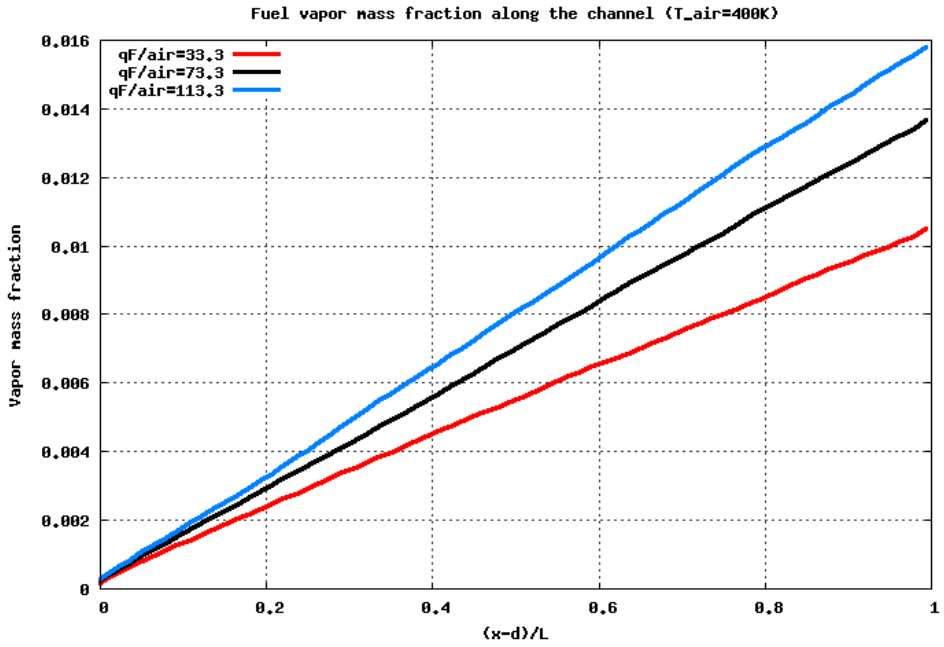

Figure 33: Jet-A vapor mass fraction along the pre-mixer at supplying air temperature of 400K at three different levels of fuel/air momentum flux ratios

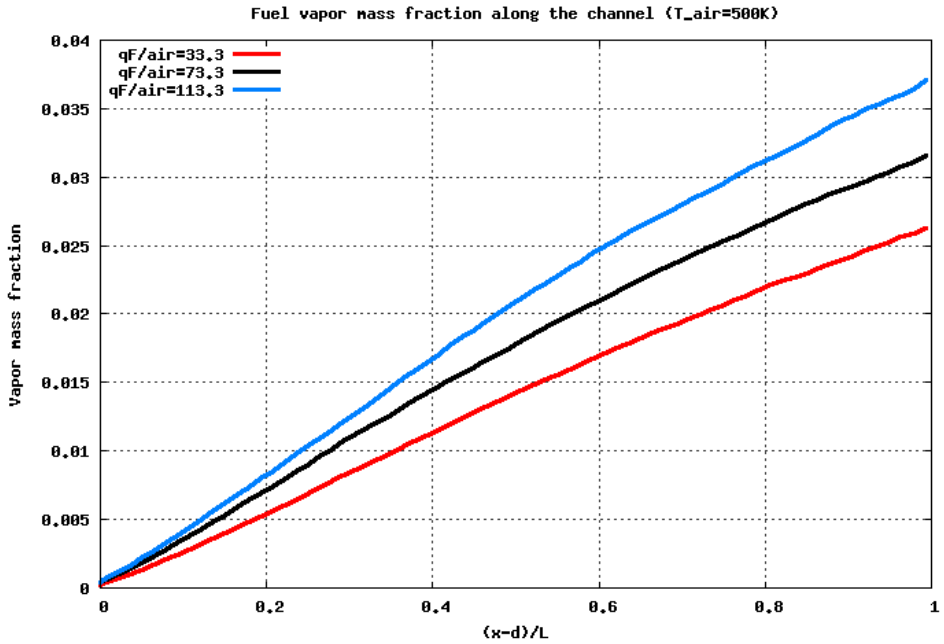

Figure 34: Jet-A vapor mass fraction along the pre-mixer at supplying air temperature of 500K at three different levels of fuel/air momentum flux ratios

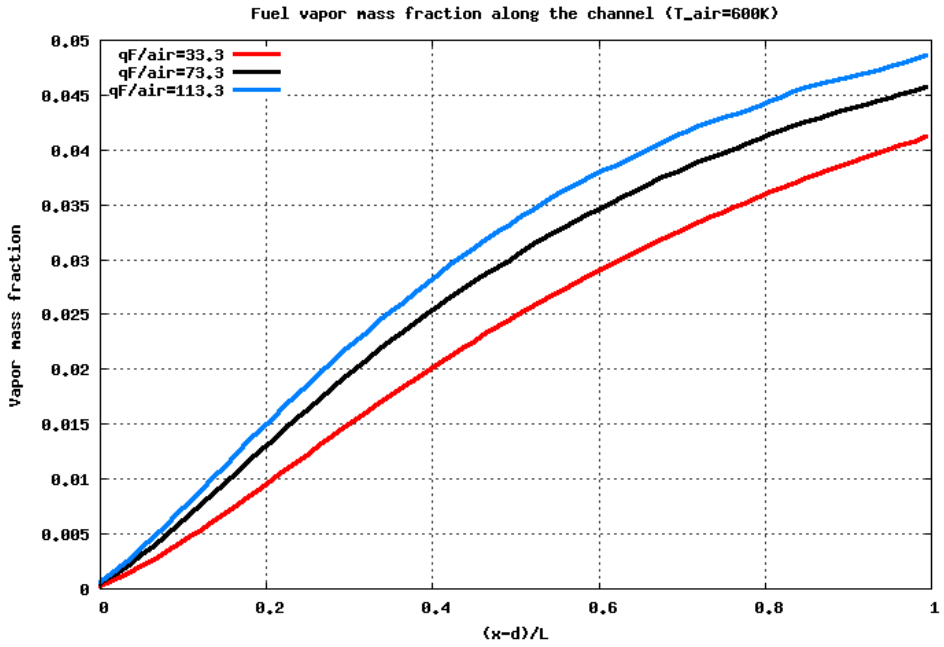

Figure 35: Jet-A vapor mass fraction along the pre-mixer at supplying air temperature of 600K at three different levels of fuel/air momentum flux ratios

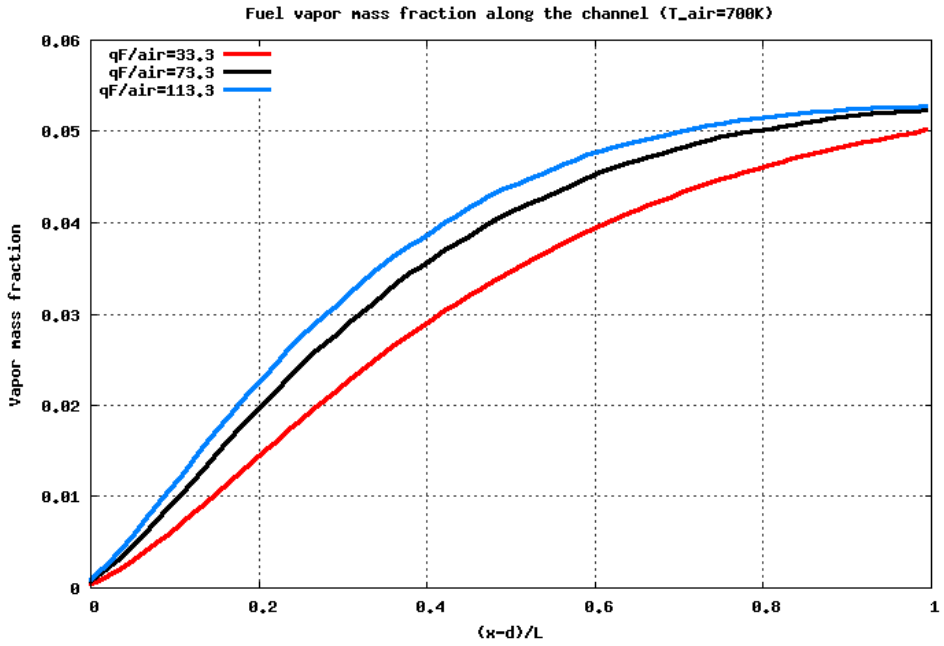

Figure 36: Jet-A vapor mass fraction along the pre-mixer at supplying air temperature of 700K at three different levels of fuel/air momentum flux ratios

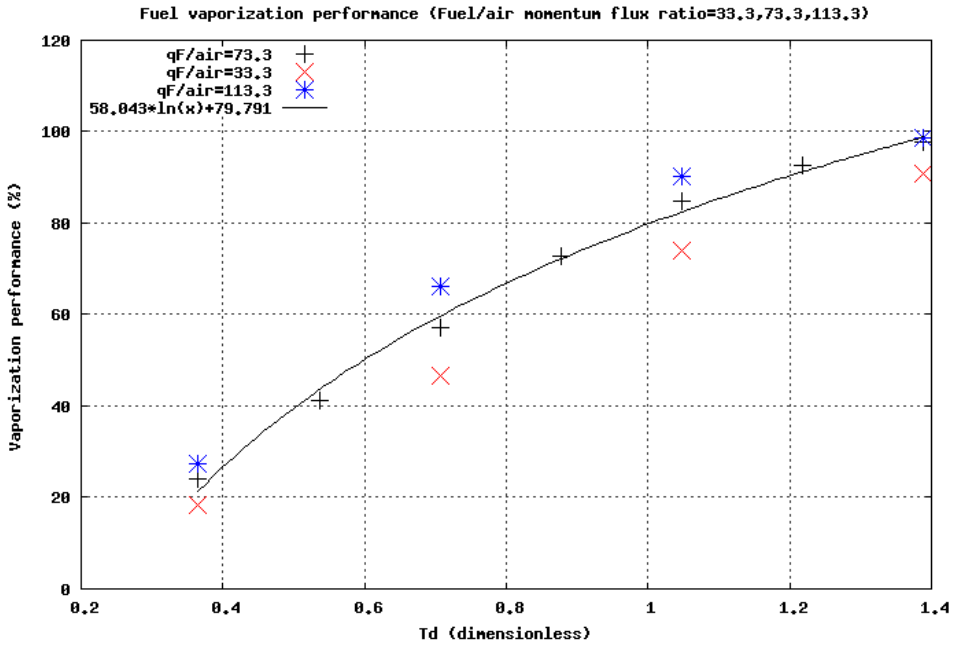

a)

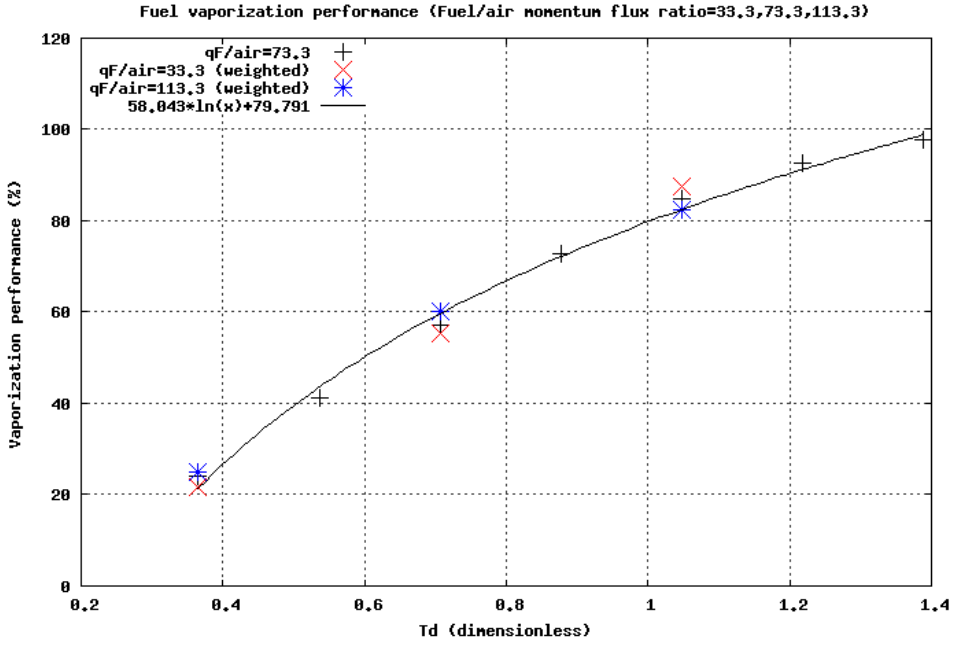

b)

Figure 37: Jet-A vaporization performance vs dimensionless supplying air temperature, T_d

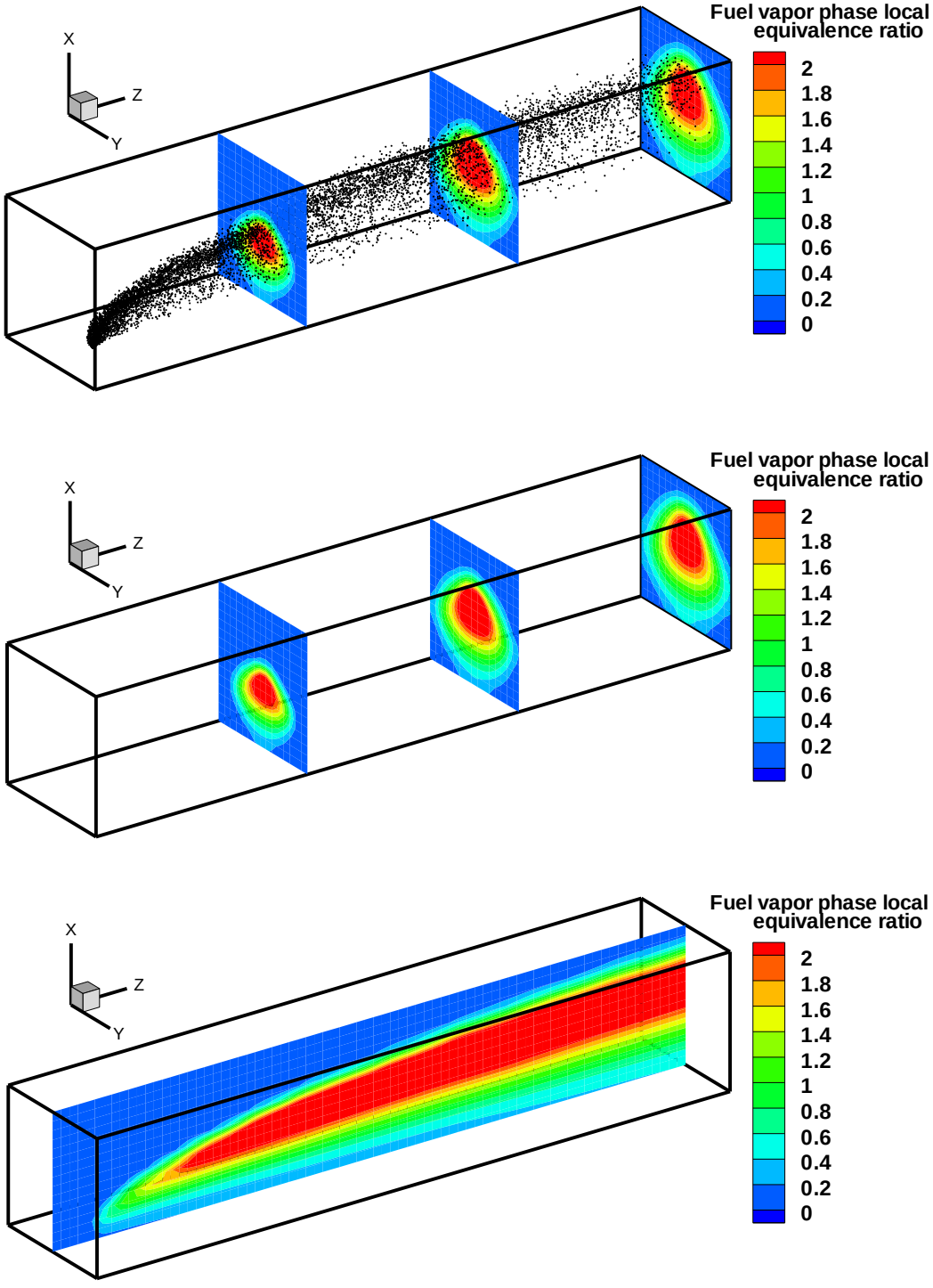

Figure 38: Jet-A fuel vapor phase local equivalence ratio contour plot at three cross-sectional Z-planes (z=10cm,20cm and 30cm) and center Y-plane

5.4 Conclusion

In this chapter, KIVA-4 code was used to simulate spray and vaporization process in a typical simplified version of rectangular pre-mixer for both biofuels and conventional fuels injections.

In the first section, the simulations are performed using the original drag model implemented in KIVA-4 code, which is applicable for a wide range of Reynolds numbers for non-evaporating sprays. As a common injection method, crossflow injections are used for fuel sprays with the expectation of its advantage in vaporizing liquid fuels compared to co-flow injections. It was found that 2.5~4.5 m/s is an optimum velocity injection range for the current configuration of the pre-mixer to achieve a better spatial distribution of droplets, therefore a constant value of 3.5 m/s was used for the injection velocity. The droplet diameter reduction and surface temperature rise were found to be strongly dependent on the fuel properties. Gasoline droplets exhibit a much faster vaporization rate due to a combination of higher vapor pressure and smaller latent heat of vaporization compared to other fuels. Though ethanol has a high vapor pressure, these droplets vaporize much slower because of its very high latent heat of vaporization which prevents the temperature rise of these droplets. A mono-disperse spray was adopted with the expectation of achieving more homogeneous fuel droplet size than a poly-dispersed spray. However, the diameter histogram in the zone near the pre-mixer exit shows a large distribution of droplet diameters. This large range of diameters was found to be mainly due to the spray cone, where droplets located in the center are protected and thus less heat is transferred into those droplets. In order to improve the vaporization performance, pre-heating has been done for fuels other than gasoline, which achieved complete vaporization with cold injection. To quantify the vaporization

performance for different fuels under different conditions, the fuel vapor mass flow rate was calculated at the pre-mixer outlet, which is the direct indicator how much percentage the liquid fuel has been vaporized when exiting the pre-mixer. Results show that pre-heating the fuels improved the vaporization performance for ethanol, jet-A and RME by 2%, 11% and 22%, respectively. The improvement for ethanol is very small since the pre-heating temperature is only 30 K higher than the cold injection temperature.

In the second section, the crossflow injections are revisited after implementing the Stefan flow corrected drag model where studies show that the drag is reduced for evaporating droplets. It was found that the spray will hit the wall under the same injection velocity using the reduced drag model. Thus, the injection velocity is reduced from 3.5 m/s to 2 m/s and the spray cone angle is increased to 140° to improve the vaporization performance. All the fuels achieved complete vaporization under the spray cone angle of 140°. Next, in order to show the advantage of crossflow injection, co-flow injections simulations under the same spray conditions were conducted. It was found that the crossflow injection indeed achieved better vaporization performance than the co-flow injection, where RME needed to be pre-heated to 493K to become fully vaporized when exiting the pre-mixer. Next, jet-A was chosen to summarize its total vaporization performance characteristics under different parameters, among which the supplying air temperature and fuel/air momentum flux ratio are most important. At each inlet air temperature, three different fuel/air mass flux ratios are used, where qFa=73.3 corresponds to the fuel/air momentum flux ratio at 2m/s of fuel injection velocity and 800K of inlet air temperature. It was found that at high inlet air temperatures, the effect of fuel/air momentum flux ratio on the

fuel total vaporization performance is relatively weak. Next, the scattered data of fuel vaporization performance at different levels of inlet air temperatures and fuel/air momentum flux ratios are curve-fitted to form a correlation function, which can be used to approximate the jet-A's total vaporization performance at specified inlet air temperature and fuel/air momentum flux ratio.

CHAPTER SIX: DROPLET COLLISION MODELING AND APPLICATION IN A CYLINDRICAL PRE-MIXER

6.1 Introduction

In the previous chapter, droplet-droplet interactions are ignored based on the assumption that droplets are sparsely distributed in space for lean fuel-air sprays such that droplet interactions are not influential to the overall vaporization performance. However, for any solid cone sprays, the number density of droplets could be very high for some regions where the collisions between droplets occur very frequently, which will in turn will have a high impact on the droplet size distribution [O'Rourke(1981)]. Thus, along with vaporization modeling, collision modeling is desirable in spray simulations in order to capture the droplet size distributions accurately.

Droplet collision modeling within a spray is a very challenging problem [Nijdam et al. (2004)] since typical liquid spray systems for gas turbine applications usually involve millions of droplets, thus a direct numerical simulation (DNS) to track each individual droplet for such systems is difficult to accomplish even with today's supercomputing facilities. For example, direct simulation of every drop will result in the order of N^2 collision computations. Typically, stochastic collision modeling approaches are used for spray simulation. In such an approach, n_i physical droplets with similar properties, such as velocity, diameter and temperature are grouped into one parcel. With the help of computational parcels the cost of collision computations is reduced to the order of $(N/n_i)^2$. This approach is commonly known as the direct simulation Monte Carlo (DSMC) technique when applied to rarefied gas dynamics simulations. Such

statistical collision modeling usually consists of two distinct phases. The first phase is to determine the probability and frequency of collisions for all possible collision pairs andthe second phase of modeling are to determine the outcome of the collision. Thus, modeling of droplet collisions for a spray is a difficult task from both numerical and physical modeling point of view.

6.1.1 Modeling the Occurrence of Collisions for a Spray

O'Rourke's droplet collision algorithm [O'Rourke(1981)] is one of those DSMC methods that is widely used to simulate the collisions and corresponding outcomes in multi-dimensional spray simulations in a Lagrangian framework. As with other standard stochastic models, O'Rourke's model calculates the probability of all potential collision partners for any parcel. Their approach naturally assumes that only parcels within the same computational cell are allowed to collide since the potential collision pairs will be in the vicinity of each other. However, the computation cells used for modeling collisions are the same for the gas phase simulations. This leads to its major drawback that the collision modeling cannot achieve grid-independent results. For example, two parcels which are very close to each other but do not lie in the same computational cell are not allowed to collide, which is naturally unphysical. Subramaniam and O'Rourke (1998) did a systematic study on the numerical convergence of KIVA-3 code, and found that grid-independent results cannot be achieved for diesel injection problems. They concluded that one major source of the problem is the large variation in spray particle density in many computational cells, which leads to large statistical errors. Schmidt and Rutland have reported that the collision results from KIVA can be highly grid-dependent [Schmidt and Rutland (2004)].

They also proposed a new modeling method based on no-time-counter (NTC) method [Schmidt and Rutland (2000)], where a separate dynamic collision mesh is used for spray collision calculations and their approach indeed yields grid-independent results.

In the current proposed work, the NTC collision algorithm was implemented for the first time into KIVA-4 code and subsequently applied it to spray simulations for both co-flow and crossflow injection methods for a typical cylindrical pre-mixer. It should be noted that the collision modeling is not restricted to cylindrical pre-mixer and can be applied with appropriate modifications to rectangular geometry as well. The details of NTC collision algorithms will be presented in a later section.

6.1.2 Modeling of Collision Outcomes

Traditionally, droplet-droplet interactions are modeled as a binary droplet collision process which could be represented as sub-steps when multiple droplets collision happens. Thus, the validity of the collision model is based on the correlations provided by binary droplet collision experiments [Jiang et al. (1992), Qian and Law (1997), Estrade et al. (1999)]. However, binary droplet collision is a complex physical process, which could lead to various outcomes. One of the early famous binary droplet collision experiments by Brazier-Smith (1972) mainly focused on the colliding water droplets in the area of meteorological applications. Since then to the early 90's, considerable amount of work on binary droplet collision experiments have been done to study the collision behaviors of hydrocarbon droplets under various ambient conditions due to its importance for spray combustion applications. Qian and Law (1999) used two dimensionless

parameters namely the impact parameter and collision Weber number to distinguish five different regimes for both water and hydrocarbon droplets under different pressures and surrounding gas compositions for equal-size binary droplet collisions.

Generally speaking, the outcome of binary droplet collision depends on three dimensionless parameters:

1. Collision Weber number, which is defined as the ratio of the inertia force to the surface tension force: $We_{col} = \frac{\rho_L u_{i,j}^2 D_s}{\sigma}$, where $u_{i,j}$ is the magnitude of the relative velocity between two colliding droplets and D_s is the diameter of the smaller drop.

2. Impact parameter: $B = \frac{2Z}{D_s + D_l}$, where Z is orthogonal distance between the center of two colliding droplets, which is illustrated in Figure 39.

3. Droplet size ratio: $\Delta = D_s/D_l$, which is defined as the ratio of the smaller droplet to the larger droplet

In general, the outcomes of binary droplet collision may be either bouncing, stable coalescence, reflexive separation, stretching separation and shattering depending on the operating conditions [Jiang et al. (1992), Qian and Law (1997)]. Estrade et al. (1999) experimentally investigated the binary collision of ethanol droplets at different droplet size ratios and proposed a theoretical criterion of bouncing. In the regime of bouncing, the droplets do not actually contact each other due to a layer of gas trapped between two colliding droplets. Figure 40 shows the regime map from their experiments at droplet size ratio of 1 and 0.5. The figure shows bouncing mostly

occurs at high impact numbers and relatively low collision Weber numbers. Since dissipation is not considered during their collision analysis, droplet velocities are assumed to be unaffected during collision. However, this assumption is questionable at low impact numbers when colliding droplets undergo considerable deformation such that their velocities will be altered after bouncing collisions. Comparing Figure 40a and Figure 40b, it is shown that the coalescence is more likely to happen at droplet size ratios other than one. For Δ=1, it can be seen that the coalescence regime is dominant for We_{col}<40 with a small regime of reflexive separation at very low impact parameters and a relatively large regime of stretching/grazing separation at high impact parameters. When Δ=0.5the coalescence regime is totally dominant for We_{col}<40 with a small regime of stretching/grazing separation at high impact parameters and the reflexive separation regime is shifted towards collision Weber numbers higher than 50.

For all the pre-mixer simulation cases studied in this thesis, the collision Weber numbers was directly recorded and most of the values were found to be less than 40. So this leads to the main assumptions for current modeling of collision outcomes: either coalescence happens or stretching/grazing separation happens. Experimental data indicate that shattering due to collision will not occur if We_{col}<40 [O'Rourke (1981)]. Thus, current modeling of stretching/grazing separation did not consider any satellite droplet formations. However, at very high collision Weber numbers, fragmentation of droplets during binary collisions can be very important. Georjon and Reitz (1999) implemented a simplified drop-shattering collision model into KIVA-II code for collisions when We_{col}>100 based on Rayleigh linear jet breakup theory. For extremely high speed injection with collision Weber number in the range of 100 and higher, the

current model will overpredict the droplet size due to the absence of the shattering mechanism in the implemented code. Also, as mentioned earlier, there is a small regime of reflexive separation at low impact parameter for We_{col}<40 of equal-size binary droplet collisions. It was not included in the current modeling of collision outcomes based on the assumptions that most of the collisions happen at droplet size ratio other than one where the most dominant regimes are either coalescence or grazing separation. Strictly speaking, the current model may over-predict the droplet size by a small margin since the droplet size will remain unaffected when reflexive separation happens other than coalescence where the droplet size will increase.

Although it is important to include all outcome regimes to accurately predict the post-collision outcomes, such as resultant number of droplets, droplet velocity, droplet size and droplet deformations, to accurately model the collision occurrence consistently is also very crucial and requires considerable efforts. The contribution of this work is to implement an improved, less mesh-dependent sampling methodology to predict consistent occurrence of collisions for the spray. Thus, the collision modeling serves as a compliment to the vaporization modeling in order to more accurately predict the vaporization performance. Since the particular problems of concern in this thesis isthe incoming air temperature being very high such that the vaporization is still the dominant factor in deciding the droplet size distribution and eventually the total vaporization performance.

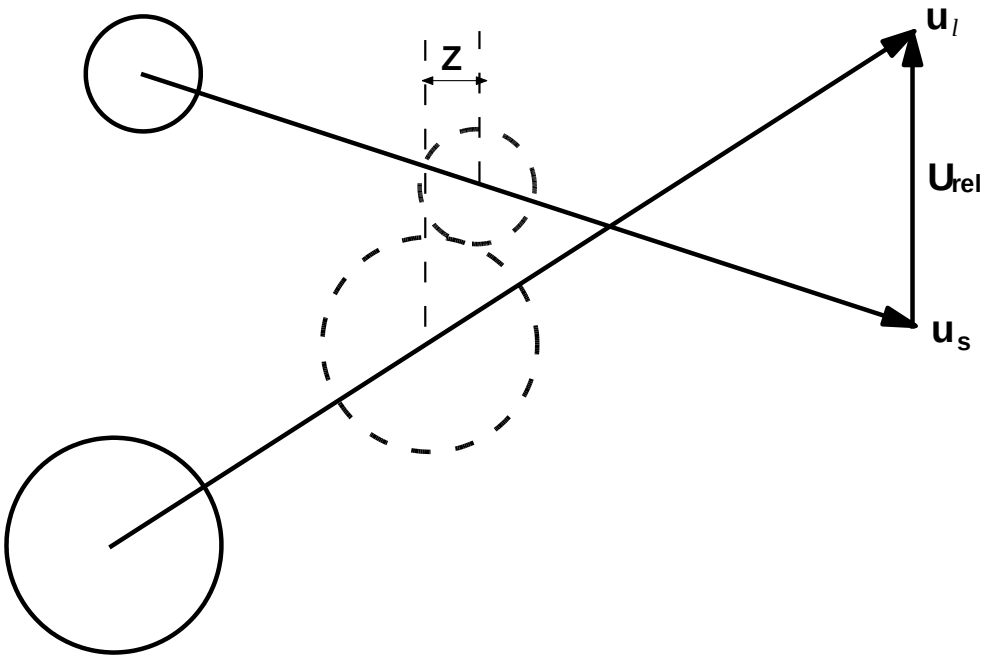

Figure 39: Schematics of binary droplet collision

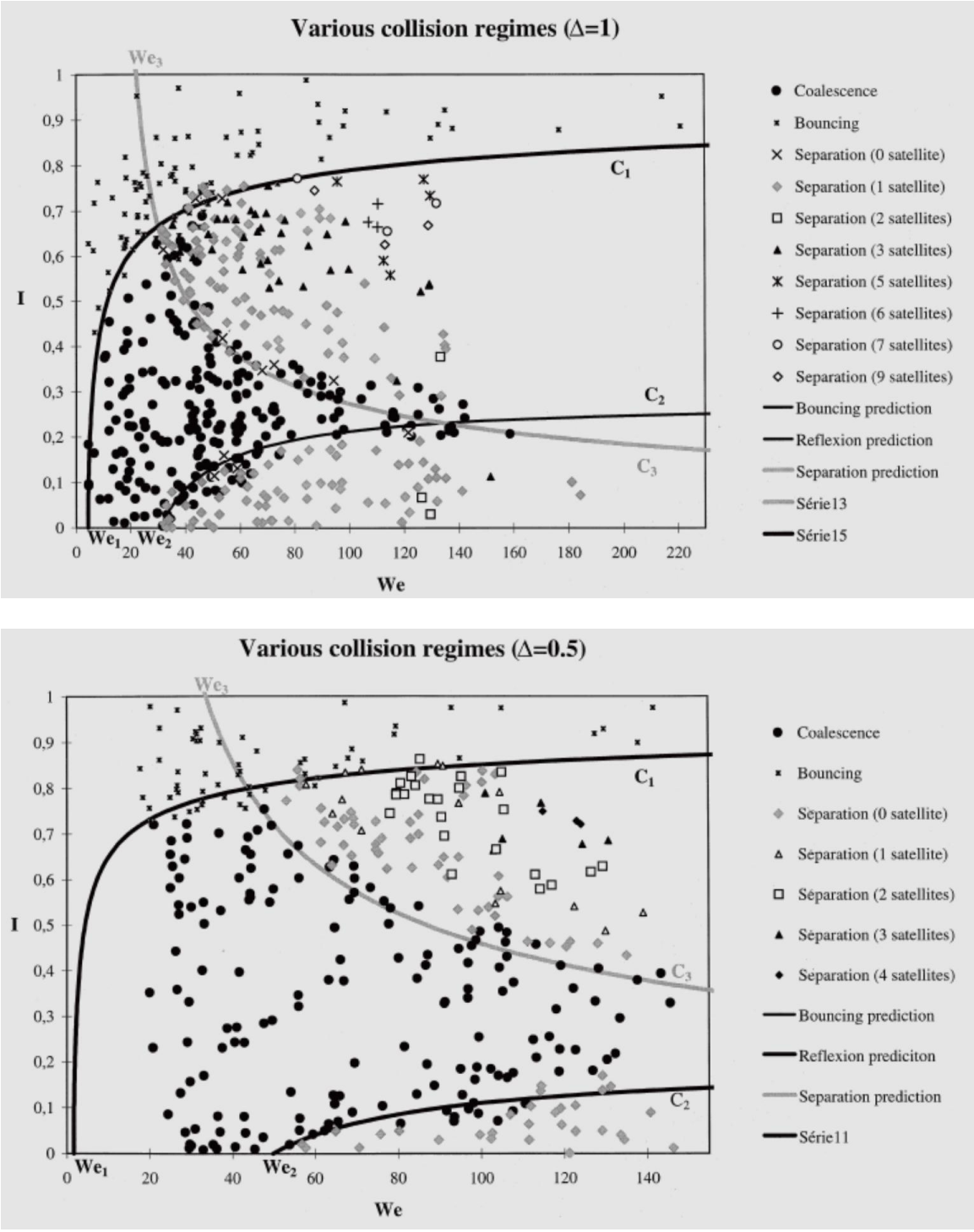

Figure 40: Collision outcome regimes for binary ethanol droplet collision a) Δ=1 b) Δ=0.5 (From Estrade et al. (1999))

6.2 Collision Model

6.2.1 Mathematical Formulations

Starting with O'Rourke's model, which assumes that there is a probability that any droplet may collide with all other droplets and is given by [O'Rourke (1981)] :

$$p_{i,j} = \frac{A_{i,j} u_{i,j} \Delta t}{V_{cell}} \tag{6.1}$$

where $u_{i,j}$ represents the magnitude of relative velocity between two droplets, and V_{cell} represents the collision cell volume. $A_{i,j}$ represents the collision cross sectional area swept by both droplets and is defined as: $A_{i,j} = \pi\left(r_i + r_j\right)^2$. This indicates that the probability of collision decreases with increase in collision cell volume. Hence, from the definition of the probability, the assumption indicates that only droplets which are very close to each other have the tendency to collide. Thus, the collision cell volume needs to be properly chosen and be adaptable in both computational time and space.

Thus, the mean expected number of collisions for a collector droplet with all droplets of the contributor is given by [Amsden et al. (1989)]:

$$\overline{\lambda} = n_j \frac{A_{i,j} u_{i,j} \Delta t}{V_{cell}} \tag{6.2}$$

O'Rourke (1981) assumes that a collector which could undergo *n* collisions with the contributor follows a Poisson distribution:

$$P_n = e^{-\bar{\lambda}} \frac{\bar{\lambda}^n}{n!} \tag{6.3}$$

Thus, the probability of no collision is $P_0 = e^{-\bar{\lambda}}$. A random number X is chosen in the interval (0,1) to determine the instance *n* [Amsden et al. (1989)]::

$$\sum_{k=0}^{n-1} P_k \le X < \sum_{k=0}^{n} P_k \tag{6.4}$$

O'Rourke's algorithm is computationally expensive ($t \sim np^2$, where *np* is the number of parcels), as a large *np* is necessary for accurate statistical representation of the spray.

If a computational collision cell contains *N* droplets, then the expected total number of collisions within this cell over a period of time of Δt will be the summation over the probabilities of all possible collisions [Schmidt and Rutland (2000)]:

$M_{coll} = \frac{1}{2} \sum_{i=1}^{N} \sum_{j=1}^{N} \frac{A_{i,j} u_{i,j} \Delta t}{V_{cell}}$, where the factor ½ is a result of symmetry

By introducing the method of computational parcel, it becomes:

$$M_{coll} = \frac{1}{2} \sum_{i=1}^{np} n_i \sum_{j=1}^{np} n_j \frac{A_{i,j} u_{i,j} \Delta t}{V_{cell}} \tag{6.5}$$

Thus, evaluation of collisions using this equation would have a cost of the order of np^2. The new approach based on no-time-counter (NTC) algorithm has a cost linearly proportional to *np*. This technique randomly chooses a subset of candidate parcels from the total population of parcels in each collision cell. The following equations show the mathematical basis of the NTC algorithm [Schmidt and Rutland (2000)]:

Recasting the total number of collisions one can write [Schmidt and Rutland (2000)]:

$$M_{coll} = \frac{(nAu)_{\max}\Delta t}{2V_{cell}} \sum_{i=1}^{np} n_i \sum_{j=1}^{np} \frac{n_j A_{i,j} u_{i,j}}{(nAu)_{\max}} \tag{6.6}$$

Here one must ensure that $\frac{n_j A_{i,j} u_{i,j}}{(nAu)_{\max}} < 1$, where $(nAu)_{max}$ is used to scale up the probability and scale down the total number of collisions.

Now one can assume that a subset parcels maybe randomly selected to represent the total population, such that:

$$\sum_{i=1}^{a*np} x_i = a \sum_{i=1}^{np} x_i \tag{6.7}$$

where a<1 and x_i is a representative property for each parcel. Thus, using the above concept, the equation be rearranged for M_{coll} to get [Schmidt and Rutland (2000)]:

$$M_{coll} = \sum_{i=1}^{np\sqrt{\frac{(nuA)_{\max}\Delta t}{2V_{cell}}}} n_i \sum_{j=1}^{np\sqrt{\frac{(nuA)_{\max}\Delta t}{2V_{cell}}}} \frac{n_j u_{i,j} A_{i,j}}{(nuA)_{\max}} \tag{6.8}$$

where $M_{cand} = \frac{n_p^2 (nAu)_{\max}\Delta t}{2V_{cell}}$ is the chosen subset to represent the total population. Thus, one can reduce the computational cost from order of np^2 to order of M_{cand}, which is proportional to np [Schmidt and Rutland (2000)].

$$M_{coll} = \sum_{i=1}^{\sqrt{M_{cand}}} n_i \sum_{j=1}^{\sqrt{M_{cand}}} \frac{n_j u_{i,j} A_{i,j}}{(nuA)_{\max}} \tag{6.9}$$

It should be noted that the number of candidate pairs given by M_{coll} is randomly chosen with replacement from the total cell population since multiple collisions may happen between parcels per time step. O'Rourke (1981) has observed that the consideration of multiple collisions is necessary to obtain accurate results for dense sprays in case of large time steps. Figure 41 illustrated the concept of the random subset representation of the total population. Suppose if a total of 7 parcels within a collision cell are found. The total possible collision pairs will be 21 and the probability for each collision pair to happen is given in Figure 41a. Then, by making a proper choice of $(nuA)_{max}$, we obtain the value of M_{coll} to be 7, which is one third of the total possible collision pairs within this cell. Next, randomly pick up 7 subsets out of the 21 total sets as illustrated in Figure 41b. As we can see, for each of the 7 pairs which are randomly chosen, their collision probability is tripled. Thus, the total collision probability of all possible collision pairs remains unaffected.

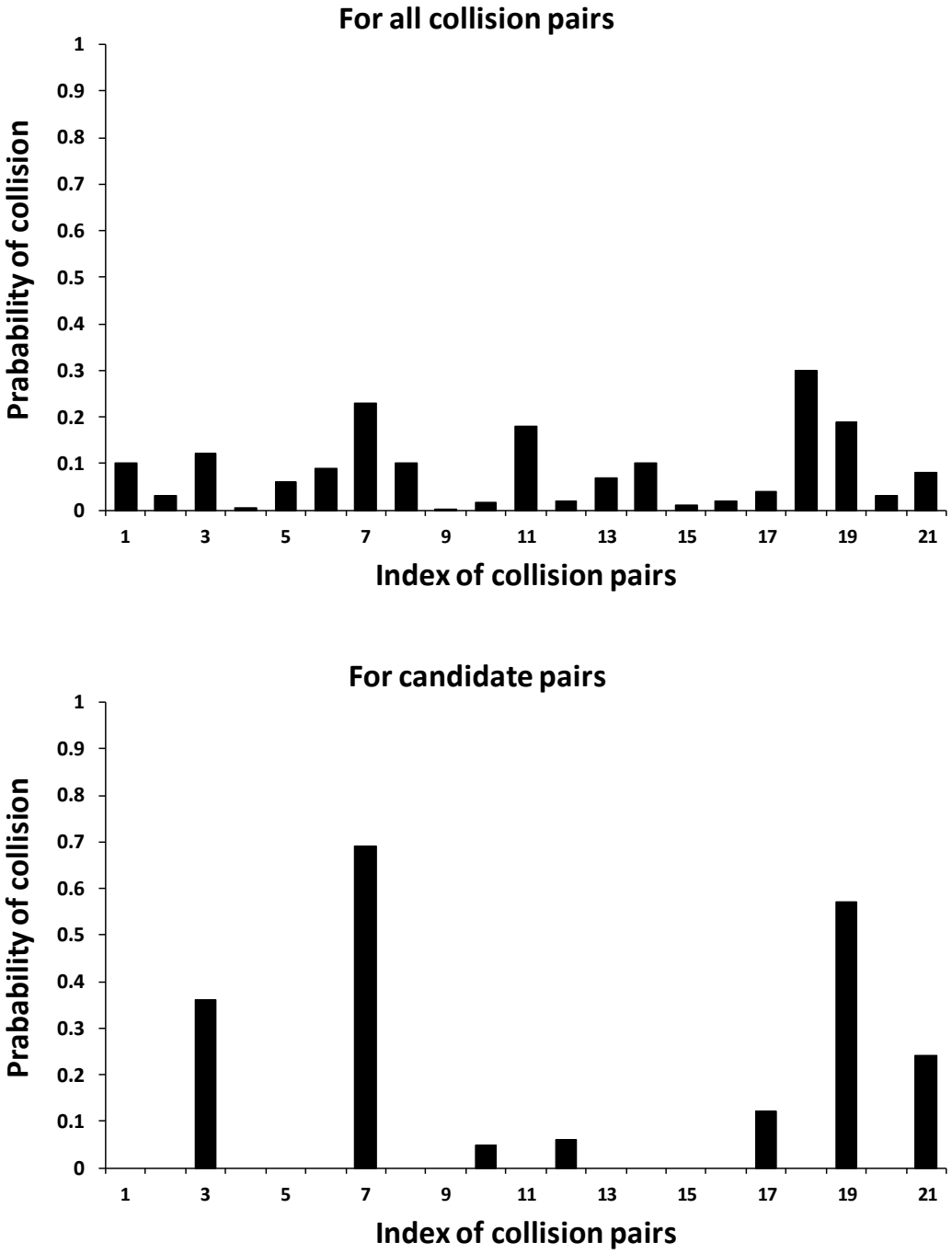

Figure 41: Illustration of the probability of collision within a collision cell a) For all possible collision pairs b) For only the subsets of all possible collision pairs

6.2.2 Implementation of NTC algorithm into KIVA-4 code

Correct implementation of NTC collision scheme into an existing multi-dimensional CFD code requires extensive programming efforts. Details of this implementation of NTC algorithm into KIVA-4 are provided here and could also be found in [Schmidt and Rutland (2000), Schmidt and Rutland (2004)].

6.2.2.1 Generation of the Independent Collision Mesh

It is important to establish a proper collision space where only parcels which are near each other are allowed to collide. Use of the static gas phase mesh as collision mesh tends to induce a high statistical error. However, droplet collisions have no connection to the gas phase mesh for DSMC methodology, and therefore gas phase mesh is not used for modeling droplet collisions. For simple single injection applications, an independent polar collision mesh around the injector is generated to envelop the spray at each time step and the size of this mesh is determined by the maximum penetration of the spray in both axial and radial directions. There is, however, a possibility that two parcels which are very close to each other maybe sorted into different collision cells. To suppress this numerical artifact, the polar mesh is randomly rotated at an angle between 0 to 2π. The resolution of the collision mesh is set such that the average number of parcels per cell is about 5~10, which is determined to be enough to resolve the spray [Schmidt and Rutland (2004)].

6.2.2.2 Sorting the Parcels by the Collision Cells

In this new algorithm, all parcels are sorted by the collision cell they reside in at every time step before collision happens. Hence, each parcel is assigned a local identification number depending on its cell of residence. In the meantime, the global identification numbers are cross-referenced with this local identification number for later use when updating their properties from collision calculations. By sorting the parcels by their collision cells, the computational efficiency is significantly improved and it becomes more convenient to perform the collision calculations using two loops: the outer one loops over all collision cells and the inner one loops over all candidate collision pairs in each cell.

6.2.2.3 Applying the NTC Collision Algorithm by Looping over all Collision Cells

For each collision cell, the number of candidate pairs, M_{cand}, is randomly chosen among all possible pairs of parcels. A collision will take place between parcel i and parcel j if the normalized probability is larger than the random deviate, XX in the interval of (0,1):

$$\frac{n_j A_{i,j} u_{i,j}}{(nAu)_{\max}} > XX \tag{6.10}$$

Making a proper choice to obtain the value of $(nAu)_{max}$ is very important. Current implementation loops over all the parcels in each collision cell to find out the maximum value of nAu, and assigns a coefficient to obtain $(nAu)_{max}$, $(nAu)_{max}=a*Max(nAu)$, with $a>1$. Although this approach requires one additional do-loop in the code which slows down the simulation, good numerical accuracy is ensured.

However, in order to use NTC collision scheme, the following criteria must be satisfied:

$$M_{cand} < \frac{n_p^2}{2} \tag{6.11}$$

Since it is not possible that the candidate pairs to exceed the total number of possible pairs, therefore:

$$(nAu)_{\max} < \frac{V_{cell}}{\Delta t} \tag{6.12}$$

This inequality is a measure of how well the spray is resolved by comparing the swept volume of the colliding parcels to the volume of the collision cell for a specified time step, Δt. Thus, when Δt is very large compared to the actual collision time, this inequality will not be satisfied. Although the satisfaction of this inequality is highly desirable to ensure a well-resolved collision calculation, a safety switch is implemented from the NTC collision calculation to direct single-cell collision (DSCC) for those under-resolved regions. The DSCC scheme is the same as O'Rourke's model except that it takes the advantage of grouping parcels into collision cells.

6.2.2.4 Calculation of the Outcome of Each Collision

As mentioned earlier, the outcome of binary droplet collision depends on three dimensionless parameters: collision Weber number, impact parameter, and droplet size ratio. The current modeling of collision considers two dominant outcome regimes, namely coalescence and grazing collision for $We_{col}<40$. An efficiency of coalescence is defined as:

$$e_{coal} = min\left(1.0, \frac{12}{5We_{col}} f(\Delta)\right) \tag{6.13}$$

where $f(\Delta)$ is an empirical function of droplet size ratio defined as:

$$f(\Delta) = \Delta^3 - 2.4\Delta^2 + 2.7\Delta \tag{6.14}$$

This function is derived based on the assumption that the rotational energy of combined entity of colliding droplets is less than the surface tension energy such that the coalescence becomes permanent (Brazier-Smith et al. 1972).

The threshold is determined by the critical impact parameter B_{cr} which is defined as [Amsden et al. (1989)]:

$$B_{cr} = \sqrt{e_{coal}} \tag{6.15}$$

When collision happens between two droplets, the impact parameter, B, is set to the square root of a uniform random number between 0 and 1. Coalescence will occur if the impact parameter B is lower than the critical value, B_{cr}; otherwise, grazing collision will occur. When coalescence occurs, both droplet size and velocity will change, whereas grazing collision only changes the droplet velocity. The resultant droplet size and velocity after coalescence collision is given by:

$$D_{new} = (D_i^3 + D_j^3)^{1/3} \tag{6.16}$$

$$\mathbf{u}_{new} = \frac{D_i^3 \mathbf{u}_i + D_j^3 \mathbf{u}_j}{D_i^3 + D_j^3} \tag{6.17}$$

where i, j denote to the two colliding droplets. The new droplet velocity after grazing collision is given by:

$$\mathbf{u}_{new,i} = \frac{D_i^3 \mathbf{u}_i + D_j^3 \mathbf{u}_j + D_j^3 (\mathbf{u}_i - \mathbf{u}_j) f_z}{D_i^3 + D_j^3} \tag{6.18}$$

where the factor f_z is given by:

$$f_z = \left(\frac{B - B_{cr}}{1 - B_{cr}} \right) \tag{6.19}$$

6.3 Grid-independence Study of NTC collision model

This section presents some simulation results between O'Rourke's and NTC collision schemes. It is known that O'Rourke's model may generate severe numerical artifact when the simulation is performed on a Cartesian mesh [Schmidt and Rutland (2004)]. As illustrated in Figure 42a, two droplets which are almost 90° apart have the highest relative velocity, while the two droplets which are 180° apart have the highest relative velocity in Figure 42b. This helps to understand why some numerical artifacts are generated. For example, Figure 43a shows the so-called "four-leaf clover" numerical artifact when the collision model is turned on for a simple non-evaporating downward spray. This numerical artifact is generated due to the fact that parcels which are 90° apart have the highest relative velocity, resulting in collision with the highest probability. If coalescence occurs for those parcel pairs, the resultant parcel will have a flow direction which is 45° offset from the x-axis or y-axis. This is the reason why the parcel number density becomes lower near the axis, whereas the spray morphology is supposed to be axisymmetric. By turning off the collision model, this four-leaf clover effects would disappear, which can be seen from Figure 43b. This numerical artifact is also not present when the simulation is performed on a polar mesh shown in Figure 43c because the azimuthal direction is better resolved on a polar mesh where the parcels with the highest relative velocities are separated into different cells. When the NTC collision scheme is applied with a separate polar collision mesh, the four-leaf clover artifact is not seen, Figure 43d, when the same simulation is performed on a Cartesian mesh.

Next, the NTC collision results are compared to O'Rourke's collision results to show its reduced grid dependence. The case studied here is a simple downward diesel spray directed into an enclosed solid cylinder. The geometry of this cylinder is the same as the geometry from Schmidt and Rutland (2004), with a diameter of 5 cm and a height of 20 cm with the spray parameters being different. The fuel studied here is diesel fuel #2 with properties from the standard KIVA-4 fuel library. The fuel is injected into the cylinder at 30 m/s with a solid spray cone angle of 30^{o}. The fuel mass flow rate is set at 1.6 g/s. To avoid injection singularity, the injection location is set 1cm away from the solid wall boundary. The injection duration is set to be 3 milliseconds while the simulation time is 10 milliseconds. The initial Sauter Mean Diameter (SMD) of the spray is 10 μm with a Rosin-Rammler diameter distribution. Parcels are injected at a rate of 3 million/s, which will eventually result in 9000 total number of parcels in the cylinder assuming no depletion of parcels due to coalescence. This total number of parcels is chosen because of the high computational expense when using original collision scheme. Three mesh resolutions used are 15x15x20 (coarse grid resolution), 30x30x60 (medium grid resolution) and 45x45x120 (fine grid resolution).

For all simulations, only the collision model and drag model are turned on, and evaporation model, breakup model, turbulence model are switched off. This serves the purpose of studying the separate effects on the collision modeling. First, the setup with original collision model is tested on all three mesh resolutions. The SMD evolution with time is plotted on Figure 44, which shows a very high level of grid dependence for the simulation results using the original collision

model. The final SMD for coarse mesh resolution and medium mesh resolution are 87 micron and 53 micron, respectively. The SMD for the fine mesh resolution reached a value of 116 micron after 8.3 milliseconds when the spray has penetrated to the bottom wall. Thus, it is seen that the difference in SMD prediction among various mesh resolutions can be more than 100%, which is unacceptable.

Next, the NTC/DSCC collision model was implemented into KIVA-4 code to perform the same tests. Results are presented in Figure 45a, where it can be seen that the predicted SMD for the coarse, medium, fine mesh resolutions are 51.7 micron, 47.6 micron, 40.5 micron, respectively. Despite the fact that the SMD results still show some grid dependence, it is much improved compared to the original collision model. As pointed out by Schmidt and Rutland (2004), the slightly grid-dependent result is not a direct artifact of the new NTC collision model, but due to the corrupting influence of the momentum and drag coupling in the code. To confirm this argument, the droplet phase was decoupled from the gas phase by fixing the gas phase velocity to be zero when the drag calculation for each droplet was performed. The results shown in Figure 45b are found to be perfect grid-independent. Although the results (Figure 45b) would be unphysical since gas phase velocity is not zero in reality, it establishes the proof-of-concept of the NTC collision scheme.

Furthermore, the NTC/DSCC collision scheme only took 1 CPU minute to complete the coarse mesh resolution simulation running on an Intel Xeon W3520 (2.67GHz) processor, a one-eighth saving compared to the original collision scheme.

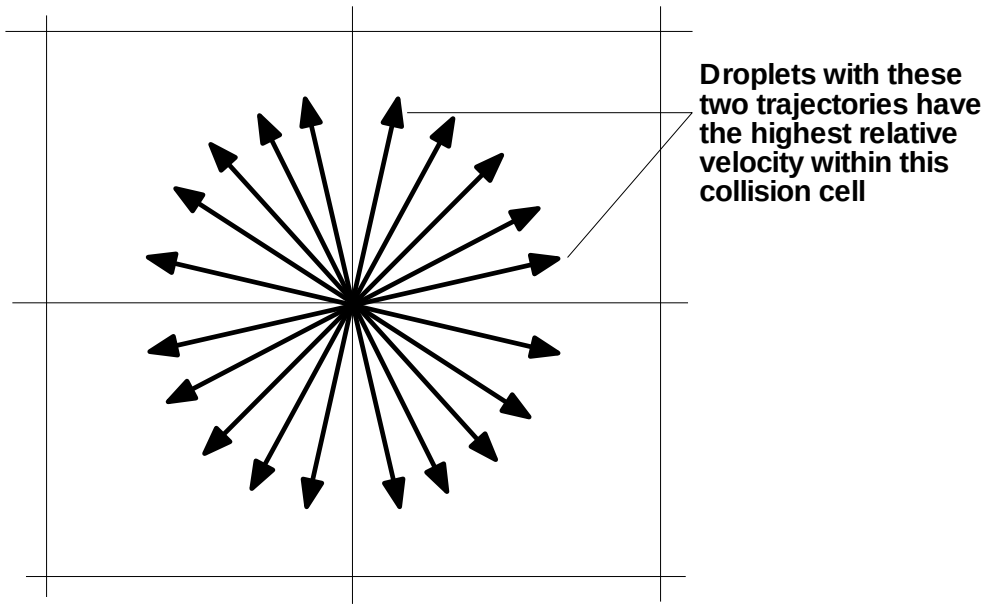

a)

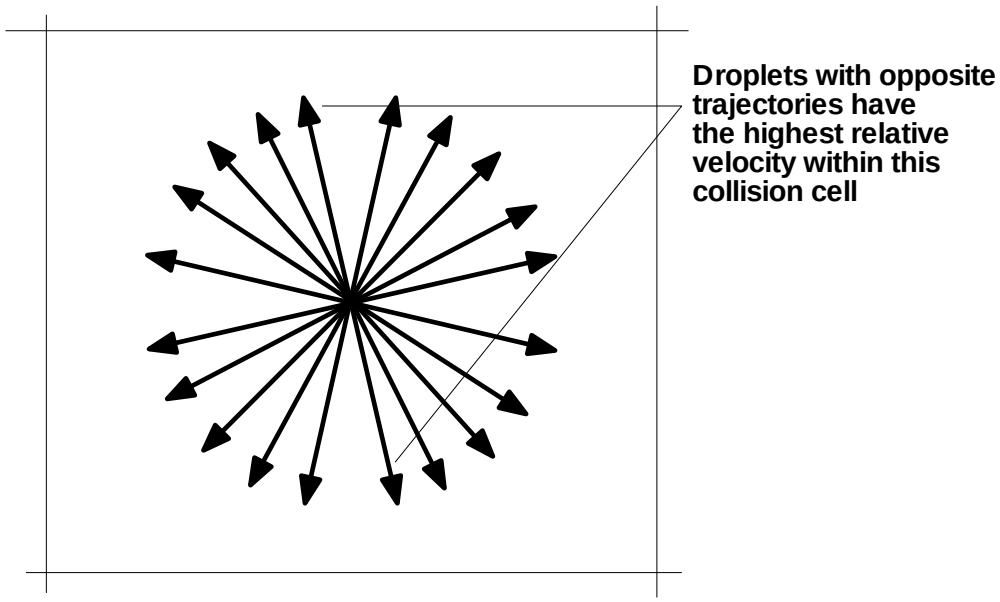

b)

Figure 42: Illustration why four-leaf clover numerical artifact may occur

a)

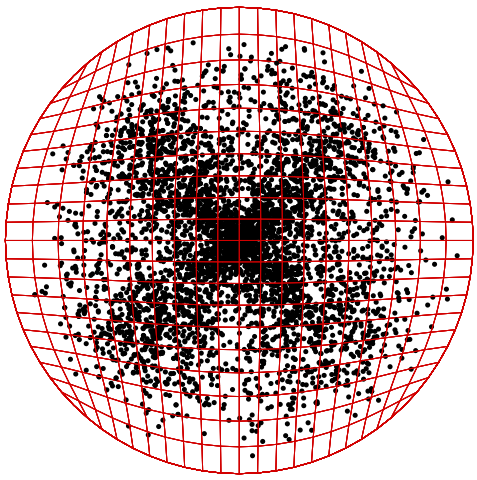

b)

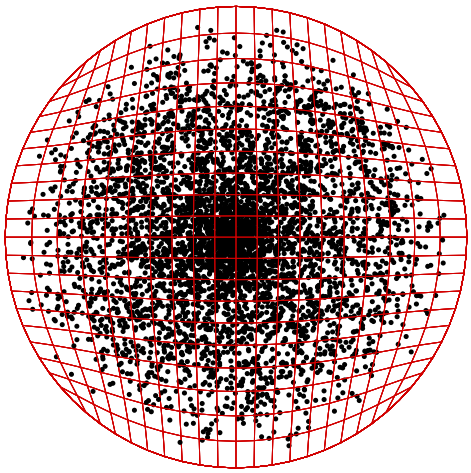

c)

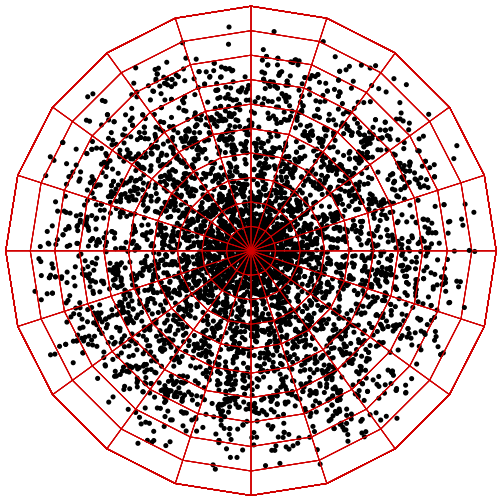

d)

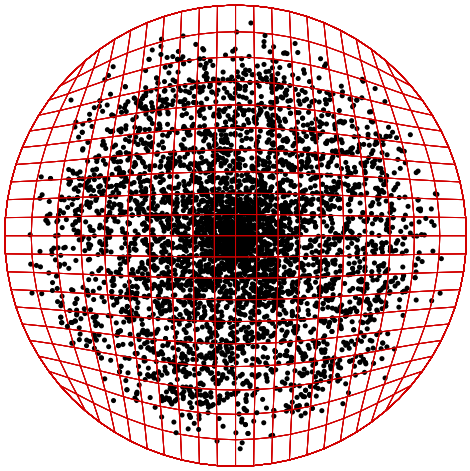

Figure 43: Simulations of a hollow-cone downward spray: a) on a Cartesian mesh using KIVA-4's original collision algorithm b) on a Cartesian mesh with collision model turned off c) on a polar mesh using KIVA-4's original collision algorithm d) on a Cartesian mesh using improved NTC/DSCC collision algorithm

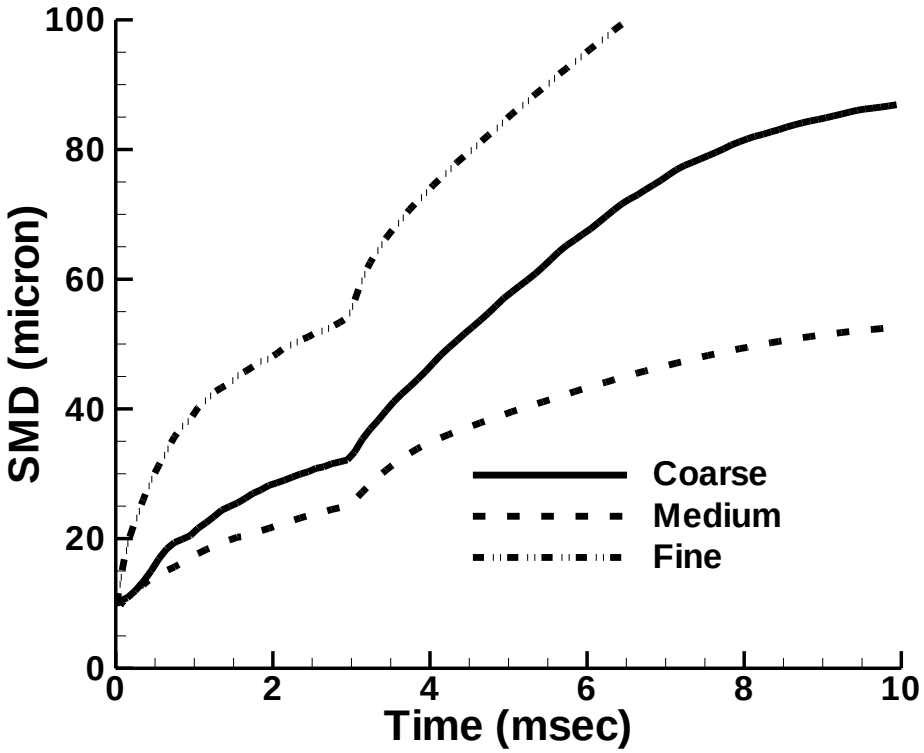

Figure 44: Simulation results for a diesel-type downward spray using original KIVA-4's collision algorithm on three different mesh resolutions

a)

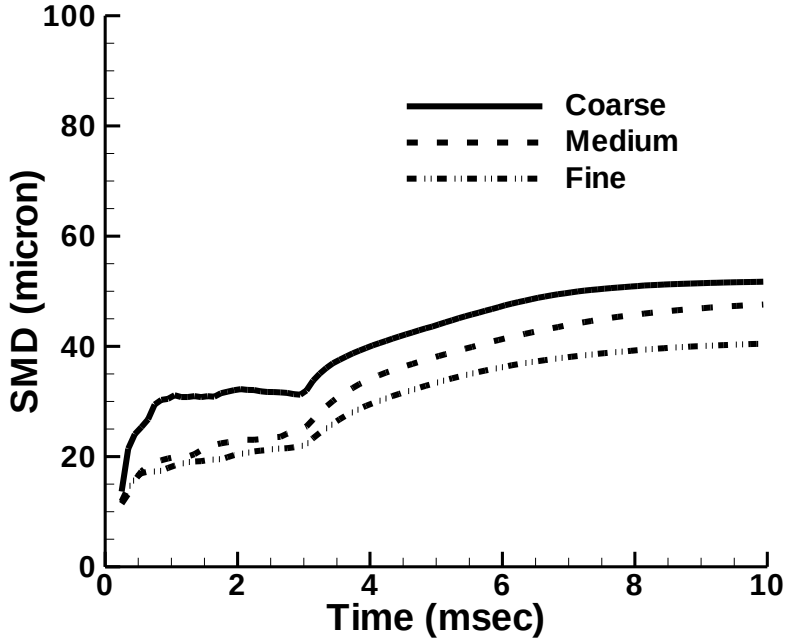

b)

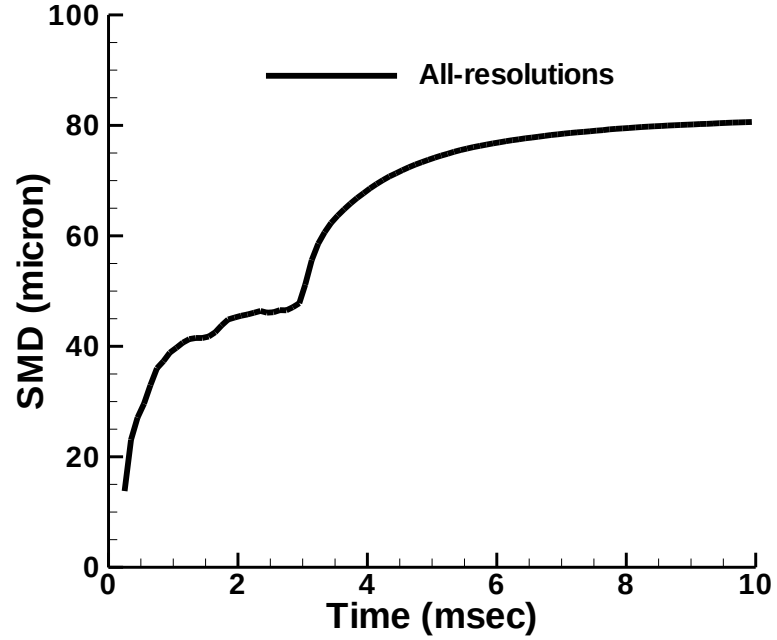

Figure 45: Simulation results for a diesel-type downward spray using improved NTC/DSCC collision algorithm on three different mesh resolutions: a) gas phase solver was turned on b) gas phase solver was turned off and fixed the gas phase velocity to be zero

6.4 Co-flow Injection in a Cylindrical Pre-mixer with Collision Modeling

The corrupting influence from the momentum and drag coupling on the discrete droplet phase is relatively small for larger droplets and this influence is also small even for small droplets when they are away from the nozzle tip [Subramaniam and O'Rourke (1998)]. Thus, for all the subsequent pre-mixer simulations, mono-dispersed spray was adopted with an initial droplet size of 80 micron diameter, which is relatively large but is still within the range of practical sprays.

Two types of liquid fuels are investigated here: Jet-A and RME. Jet-A is the primary conventional fuel used in the aviation industry. RME is a biodiesel which can be blended in jet-A. RME has already been tested in blends with Jet-A fuel as a potential surrogate fuel in the aviation industry [Dagaut et al. (2007)]. Thus, it is important to study both fuels and compare their vaporization characteristics.

6.4.1 Computational Setup for Co-axial Pre-mixer

The computational domain in Figure 46 represents a typical simplified cylindrical pre-mixer with a length of 300 mm and a radius of 60mm. The pre-mixer has three bounding surfaces with the following set of boundary conditions: the left side is assigned as velocity inlet boundary condition with fixed co-flow velocity and temperature and the right side is pressure outlet boundary condition. The cylindrical surface is assigned law-of-wall boundary conditions. Air is introduced into the pre-mixer at a constant velocity and temperature of 10 m/sec and 800 K, which is the same as the previous chapter. The liquid fuel is injected into the pre-mixer co-axially with the air after the gas phase flow field reached a steady state in about 0.01 s. Figure 46

also shows the contour plot of the gas phase velocity in the co-flow direction at two cross-sectional planes of Z=70 mm and Z=230 mm respectively. The two-way coupling effects can be clearly observed from the velocity contour plot where the velocity near the center of slice decreased due to the inter-phase drag from the discrete droplet phase.

First, a baseline set of parameters was established with a fairly large spray angle of 90° and 3 m/s injection velocity such that the spraying droplets are well dispersed within the pre-mixer while not impacting the wall. A summary of the baseline parameter set is listed in Table 6. All the simulation cases were run at atmospheric pressure. In order to achieve better droplet dispersion and vaporization performance, a high value of turbulent intensity (20% of the mean crossflow kinetic energy) was used for all the simulations reported here. The average number of parcels per collision cell is fixed around 2 since the real collision volume is approximately one third of total volume generated by the polar collision mesh. Thus, the real average number of parcels per collision cell is actually around 6. This is verified by recording both the total number of collision cells that contain at least one pair of parcels and the total number of parcels contained within the simulation volume.

6.4.2 Spray Simulation Results and Analysis for the Baseline Tests

In this section, the spray simulations results are presented for both jet-A and RME with the same initial injection temperature of 293 K. Three different mesh resolutions are used and the details are listed in Table 7.

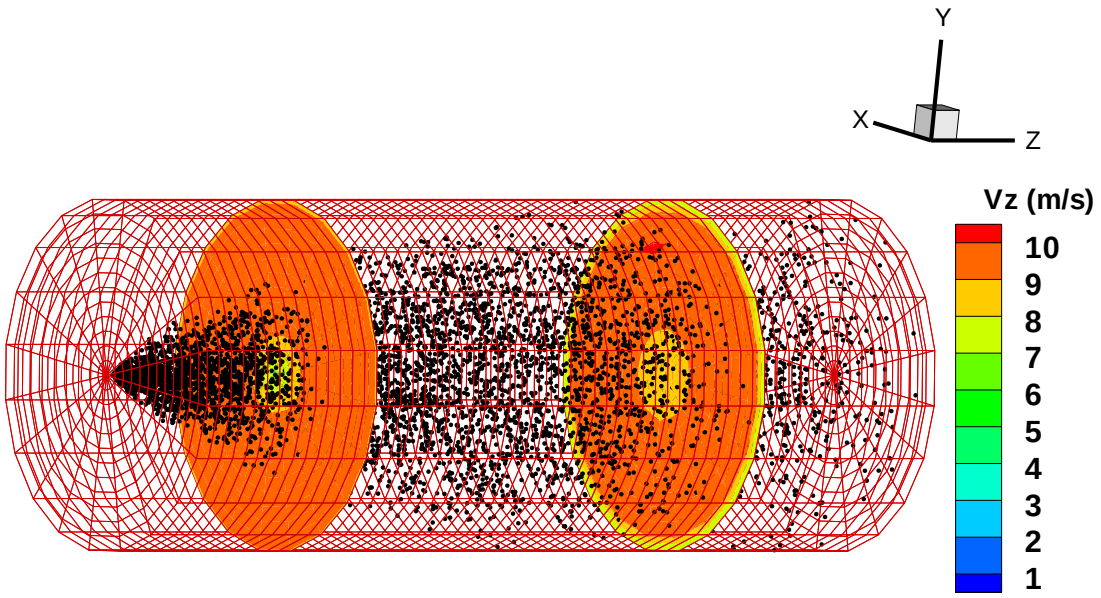

Figure 46: Three-dimensional view of co-axial flow injection with converged gas phase velocity field

Table 6: Summary of baseline flow parameters

Initial droplet diameter (μm)	Air flow velocity (m/s)	Air flow temperature (K)	Air flow turbulent intensity	Droplet injection velocity (m/s)	Spray cone angle (degree)	Fuel mass flow rate (g/s)	Air mass flow rate (g/s)
80	10	800	0.2	3	90	2.7	48

Table 7: Summary of mesh resolutions

	Cells in radial direction	Cells in axial direction	Cells in azimuthal direction	Total cells
Coarse	6	30	10	1800
Medium	12	60	20	14400
Fine	18	90	30	48600

First of all, to show that the results are grid independent, the Sauter-mean-diameters (SMD) of the spray are calculated and plotted versus Z-axis by equally dividing the pre-mixer into 30 zones. The SMD is then normalized by the initial injection SMD, which is D_0. The jet-A spray simulations for three different meshes are presented in Figure 47. Figure 47a shows that the SMD variation along the z-direction for all three grids. The initial increase of SMD is probably due to the high coalescence rate and low vaporization rate near the injection port where the number density of the droplets is relatively high and the surface temperature of the droplets is relatively low. Meantime, the total number of droplets within each zone is also plotted since it is a good indicator of the spray vaporization performance, and the results for all grids are shown in Figure 47b. The variations of both SMD and total number of droplets along z-axis show very good grid-independence, except that the SMD of coarse grid shows slightly deviation from the other two grids, which is probably because the gas phase is not well resolved. Thus, for the rest of the simulation, the medium mesh resolution is adopted to ensure that the gas phase flow field is well resolved.

Next, the fuel vapor mass flow rate at the outlet is calculated since it indicates the percentage of the liquid fuel that has been vaporized through the pre-mixer chamber. The jet-A fuel vapor mass flow rates for all grid resolutions are plotted versus simulation time in Figure 48. Results also show very good grid-independence. The final steady-state jet-A fuel vapor mass flow rate is around 2.2 g/sec for all resolutions. Since the liquid fuel is injected at a rate of 2.7 g/sec, 2.2 g/sec vapor mass flow rate at the outlet indicates that 81.5% of liquid jet-A fuel has been vaporized from the injection point to the outlet of the pre-mixer. The RME fuel vapor mass flow

rate (for medium mesh resolution) is also presented in Figure 48, which shows an average value around 1.6 g/sec, implying that 59.3% of liquid RME has been vaporized through the pre-mixer. There is 22.2% difference in vaporization performance between jet-A and RME, which is obvious from the vapor pressure plot for each fuel as shown in Figure 12. Were the vapor pressure of jet-A is much higher compared to RME at the same temperature, indicating that jet-A would indeed have a higher vaporization rate.

Furthermore, to show the importance of the collision modeling and its influence in determining the vaporization performance, the collision model was turned off and compared to the results with the collision model activated. From Figure 49a, the final steady-state jet-A and RME fuel vapor mass flow rates without collision is around 2.4 g/sec and 1.9 g/sec, respectively. This indicated that the vaporization performance is lowered by 7.4% for jet-A and by 11.1% for RME when the collision model is activated. This is primarily due to the coalescence induced by collision which leads to surface area destruction producing larger droplets that have lower vaporization rate. This can be proved unambiguously from Figure 49b, which shows that the SMD distribution along z-axis for all cases. It can be seen that the SMD for both fuels will continuously decrease along the z-axis if there is no collision. However in reality SMD for RME increased up to 1.3 times of its original injection size and slowly decreased to 1.2 times of its initial injection size along z-axis when the collision model is activated. Thus, the results show that droplet collisions have high impact on the droplet size distribution which will in turn influence the vaporization performance.

a)

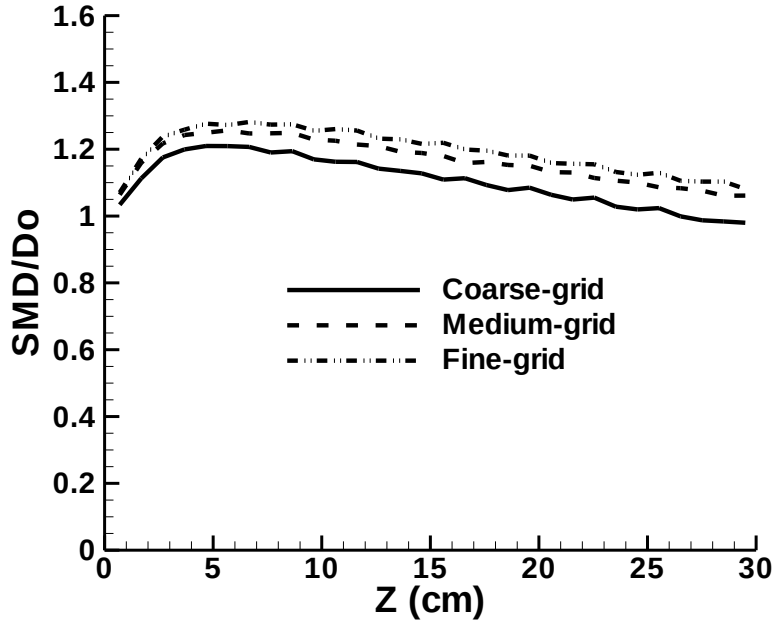

b)

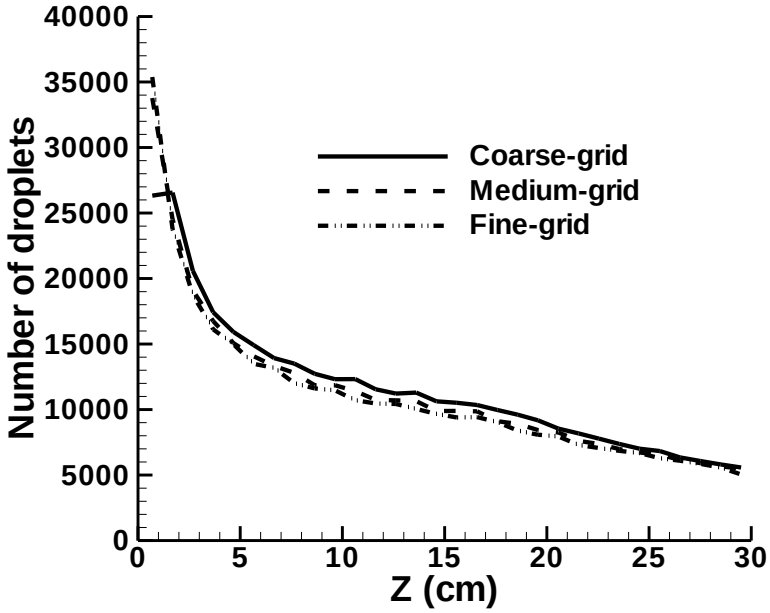

Figure 47: Co-axial flow injection simulation of jet-A for all three mesh resolutions: a) Normalized Sauter-mean-diameter plot versus z-axis b) total number of droplets within each zone plotted along z-axis

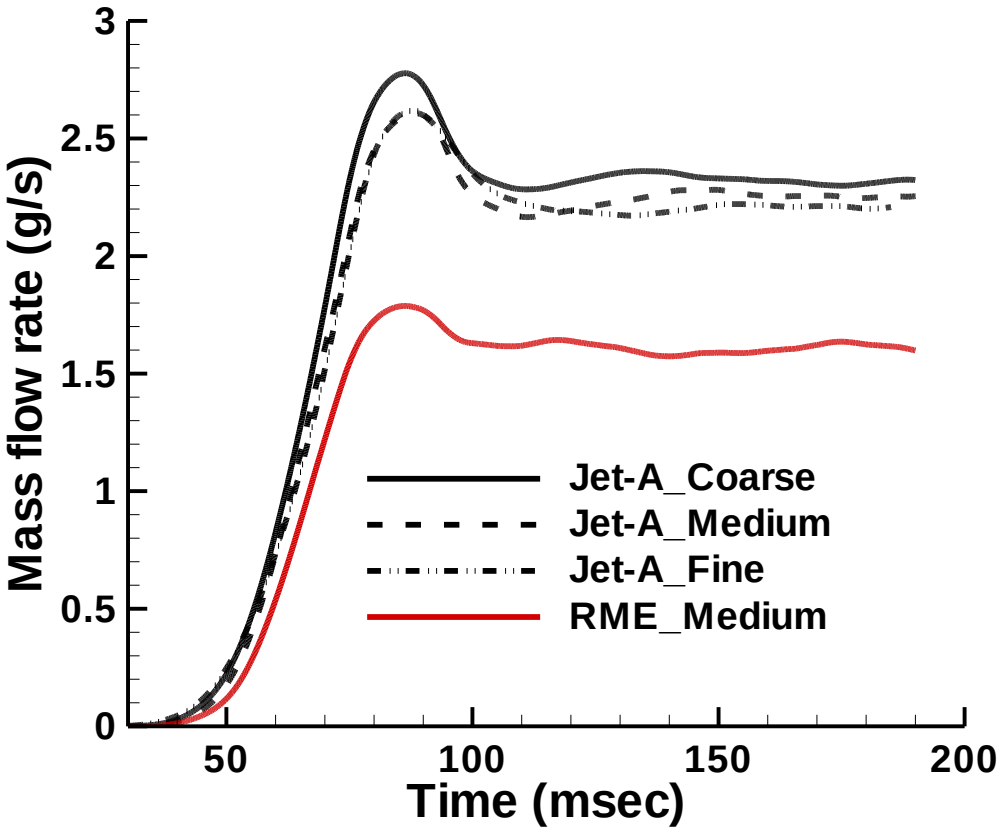

Figure 48: Fuel vapor mass flow rate at the pre-mixer exit plotted versus simulation time for jet-A of all grids and RME of medium resolution for co-axial flow injections (All results are time-averaged with an average period of 2 milliseconds)

a)

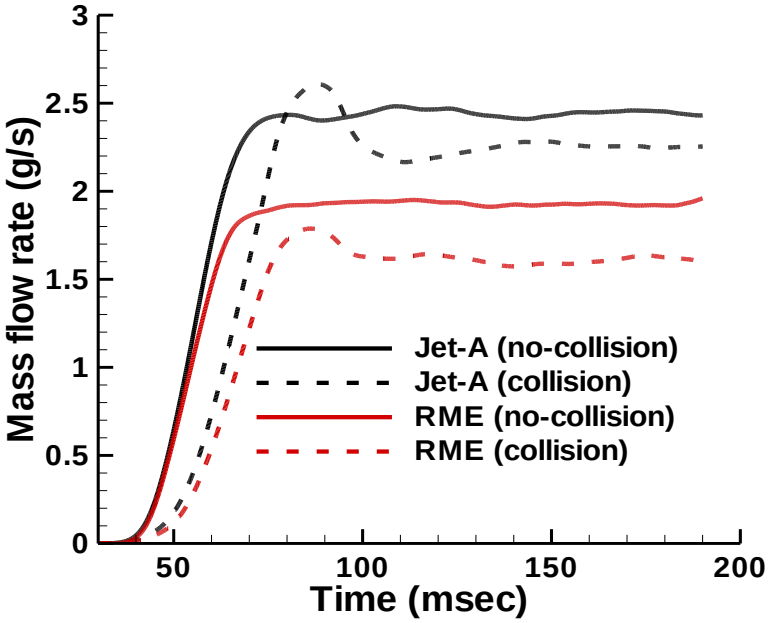

b)

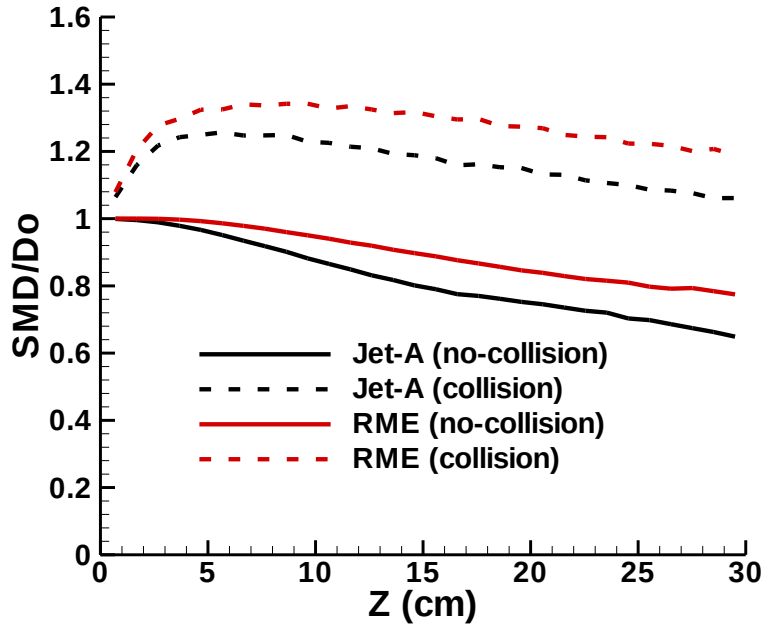

Figure 49: Simulation results of jet-A and RME: a) Fuel vapor mass flow rate at the pre-mixer exit b) normalized SMD plotted along z-axis. Comparisions between simulations without collision model and with collision model for spray cone angle of 90° and injection velocity of 3m/s

6.4.3 Spray Simulation Results and Analysis with Higher Spray Angle and Injection Velocity

It was shown in the previous section that the vaporization performance for either fuel is not ideal, especially for RME. To explore the possibility of improving the vaporization performance within the current pre-mixer configuration, a series of combinations of spray cone angle and injection velocity was tested. This was done since larger spray cone angle and higher injection velocity will improve the dispersion of the injected droplets which will in turn improve the vaporization performance.

Several spray cone angles and injection velocity combinations were attempted for the simulation. Beyond 130° and 5 m/s, part of the spray was seen to impact the wall and hence higher combinations were not desired. Including this combination of cone angle and injection velocity, four combinations are presented: 1) 90° and 3 m/s (baseline), 2) 90° and 5 m/s, 3) 130° and 3 m/s and 4) 130° and 5 m/s. Figure 50 shows the RME vapor mass flow rate for all combinations. One can see that the RME vapor mass flow rate exhibits the highest value of 2.3 g/s for 130° spray angle and 5 m/s for injection velocity, implying that 85.2% of the injected RME fuel has vaporized. Compared to the baseline case there is a 25.9% improvement in vaporization performance for RME. Thus, 130° spray angle and 5m/s injection velocity serves as an optimum combination to efficiently vaporize the liquid fuels for current pre-mixer configuration. As done in the previous section, results on the vaporization performance and droplet size distributions are compared between the collision model deactivated and activated (Figure 50). Surprisingly, Figure 51a shows that the vaporization performance is almost identical for both fuels with and

without the collision model: jet-A achieved 96.3% in vaporization performance while it is 85.2% for RME. However, the SMD distribution (obtained with collision model) along z-axis as seen in Figure 51b, shows consistently higher value than that obtained without the collision model. Large droplets are expected to have lower vaporization rate, which seems to be contradictory to the identical vaporization performances in Figure 51a. This can be explained as follows: with the collision model activated, the average droplet size could increase due to coalescence. However, the drag equation in conjunction with the droplet acceleration equation (Newton's second law), suggests that the droplet acceleration is inversely proportional to the square of the droplet diameter, i.e., it is smaller for larger droplets. Lower acceleration will result over a longer residence time and vaporization time for the larger droplet in the pre-mixer. Thus, smaller droplets vaporize faster but also travel faster through the pre-mixer and larger droplets vaporize slower but also travel slower. Under certain conditions, these two opposing effects can cancel each other out in a cumulative sense, leading to approximately similar vaporization performances as obtained without incorporating the collision model. The balance is only achieved in the case of higher spray cone angle and injection velocity, while the baseline results still show lower vaporization performance for results using the collision model. This is because the spray occupies less space at lower spray cone angle and injection velocity, resulting in higher droplet number density, which in turn, promotes droplet collision probability. Figure 49b shows relatively higher SMD along the pre-mixer length for lower spray cone angle and injection velocity. As usual, to improve the vaporization performance for RME, the fuel was pre-heated to 493 K and found that the corresponding vaporization performance is improved to 95%.

To quantitatively describe the dispersion level of the spray at different combinations of spray cone angle and injection velocity and show the influence of the collision modeling on the spray dispersions.Mmaximum radial extent of the spray in each zone was calculated along the pre-mixer and normalized by the pre-mixer radius to clearly show how well the spray is dispersed at each condition. RME is used to show these effects in Figure 52. For baseline tests, the collision activated results show relatively higher dispersion levels than when the collision model is deactivated. From the previous analysis, it is understood that the coalescence rate induced by collision is pretty high for baseline cases such that the average droplet size is much higher when the collision model is activated. Thus, larger droplets would travel farther in the radial direction compared to smaller droplets due to the smaller deceleration rates. Therefore, the dispersion level is relatively high when collision is activated. From Figure 52, it can be seen that the dispersion level for 130° spray cone angle and 5 m/s injection velocity is much higher than the baseline tests. This also quantitatively supports our previous analysis where the spray is better dispersed at higher spray cone angles and injection velocities, which improves the vaporization performance significantly.

Another important spray characteristic is the droplet size distribution when collision is activated. Figure 53 shows the histogram of the droplet diameter distributions for the baseline cases for both jet-A and RME within the primary zone of interest, which is defined from cross-section plane z = 28 cm to plane z = 30cm. This histogram shows the spread of the droplet diameter distribution near the exit of the pre-mixer. The total range of the histogram is defined from zero to the maximum droplet diameter existing in the zone for both fuels (which is about 190

microns). The entire range is divided into several bins where the size of each bin is approximately 6 microns. The frequency is normalized by the total count of droplets within the zone of interest for each fuel. As seen from the diameter histogram, jet-A shows the highest frequency around 48 micron, while RME shows the highest frequency around 66 micron. This large range of diametes near the pre-mixer exit indicates how the collision between droplets can affect the droplet size distribution within a spray. It also indicates that vaporization performance needs to be improved to eliminate the large droplets which can potentially affect the combustion efficiency. Figure 53b shows the diameter distribution for the simulations at 130° spray cone angle and 5m/s injection velocity. The spread of the diameter distribution is constrained below 120 micron, which is much smaller than the baseline tests. Thus, vaporization performance is improved at higher dispersion levels of the spray since very large droplets are not present.

To avoid droplet collision on the walls, swirl is not introduced at the inlet of the pre-mixer. Therefore, in the current configuration, the vapor concentration at the exit is expected to deviate from homogeneity. To quantify the homogeneity of the fuel vapor mass fractions, the so-called "unmixedness" parameter is calculated at the pre-mixer exit [14]. The unmixedness parameter is defined as the standard deviation of the fuel vapor mass fraction divided by the averaged fuel vapor mass fraction within the zone of interest. The ideal value of unmixedness should be zero, meaning perfect homogeneity. For the baseline tests, the values of unmixedness for jet-A and RME are 0.81 and 0.77, respectively. This shows that the extent of inhomogeneity for both fuels is very similar. For the tests at 130° spray cone angle and 5m/s injection velocity, the values of unmixedness for jet-A and RME are 0.33 and 0.25, respectively. These low values of

unmixedness suggest that the fuel-air mixture is much more homogeneous when the dispersion level of the spray is high.

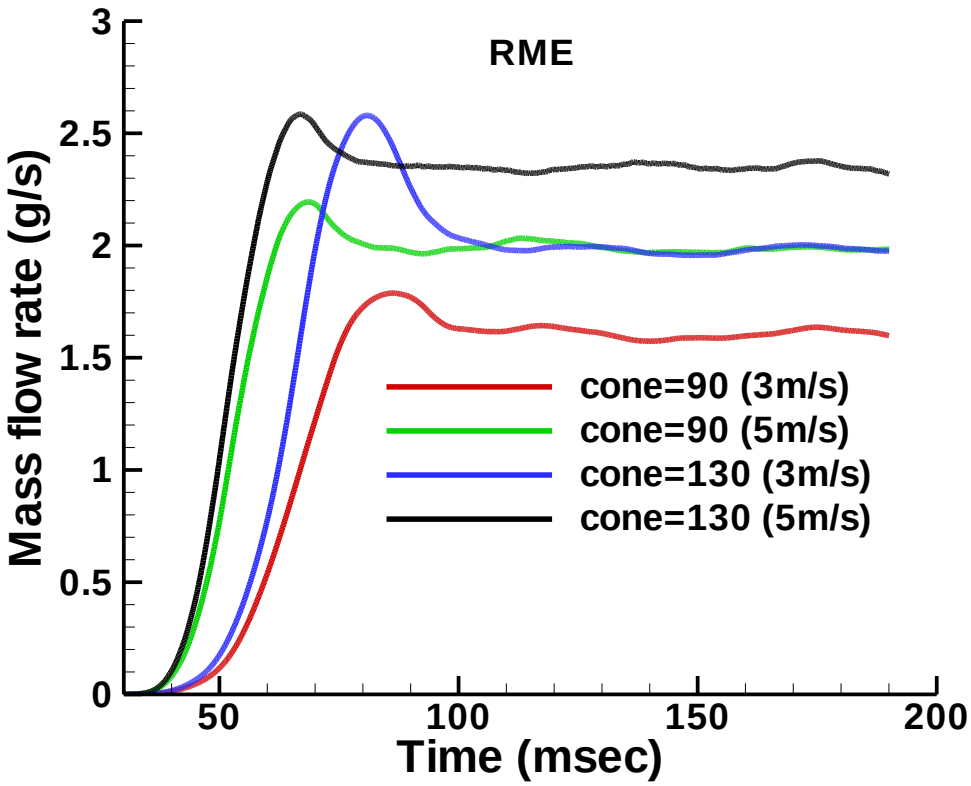

Figure 50: RME vapor mass flow rate at the pre-mixer exit for different combinations of spray cone angle and injection velocity.

a)

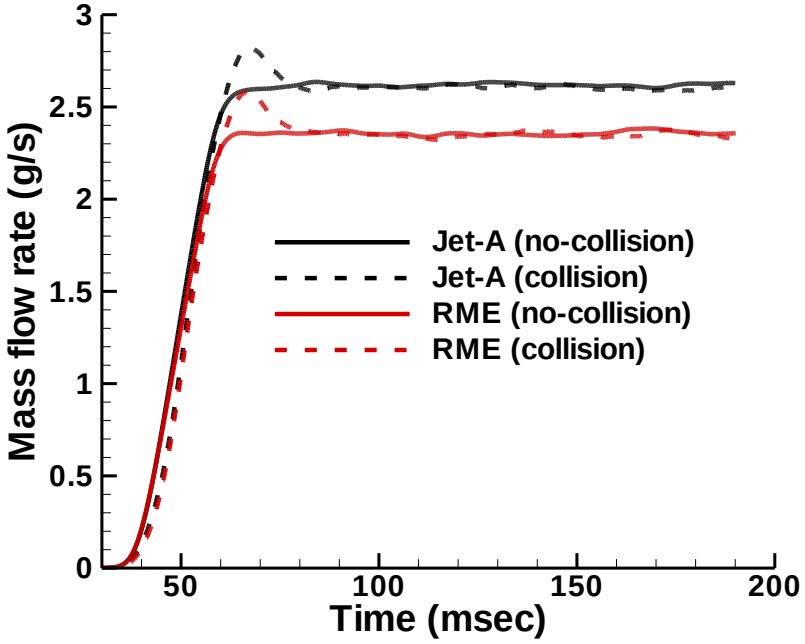

b)

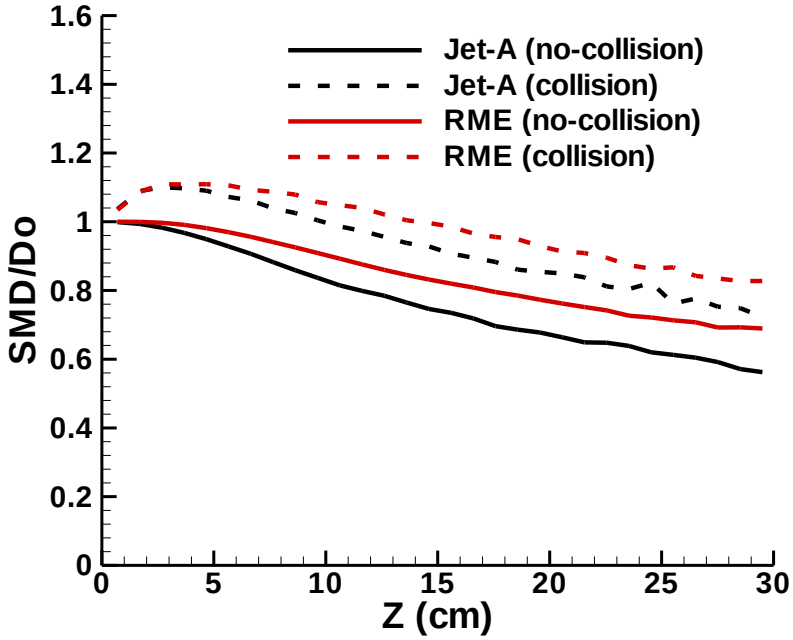

Figure 51: Simulation results of jet-A and RME: a) Fuel vapor mass flow rate at the pre-mixer outlet b) normalized SMD plotted along z-axis. comparisions between simulations without collision model and with collision model for spray cone angle of 130° and injection velocity of 5m/s

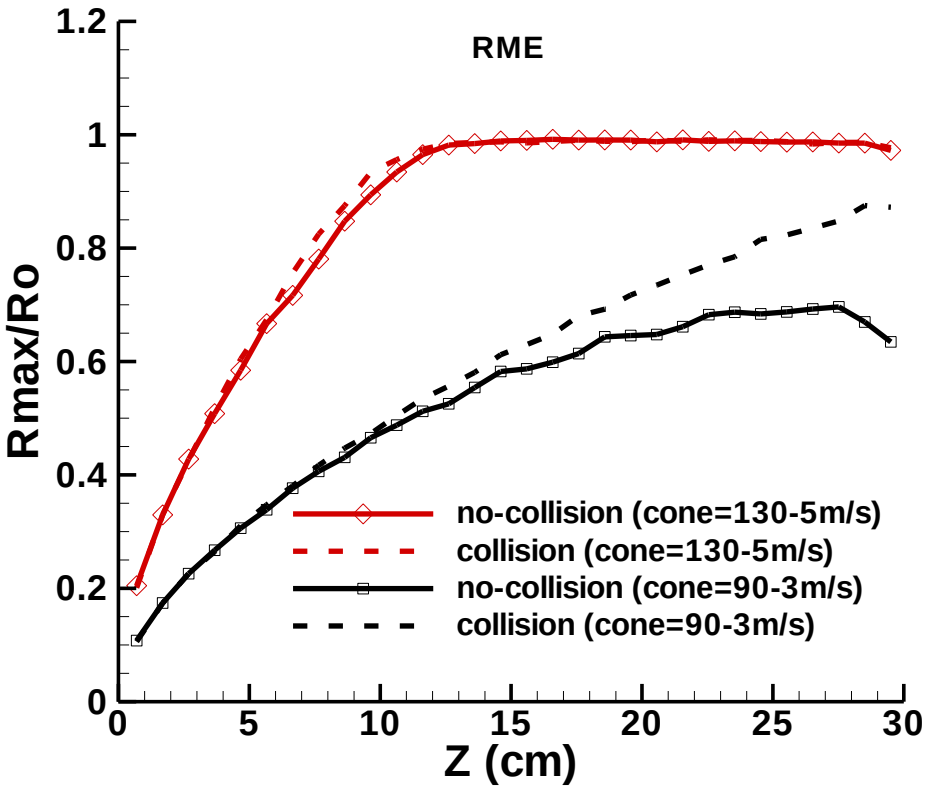

Figure 52: Spray dispersion along z-axis at various conditions

a)

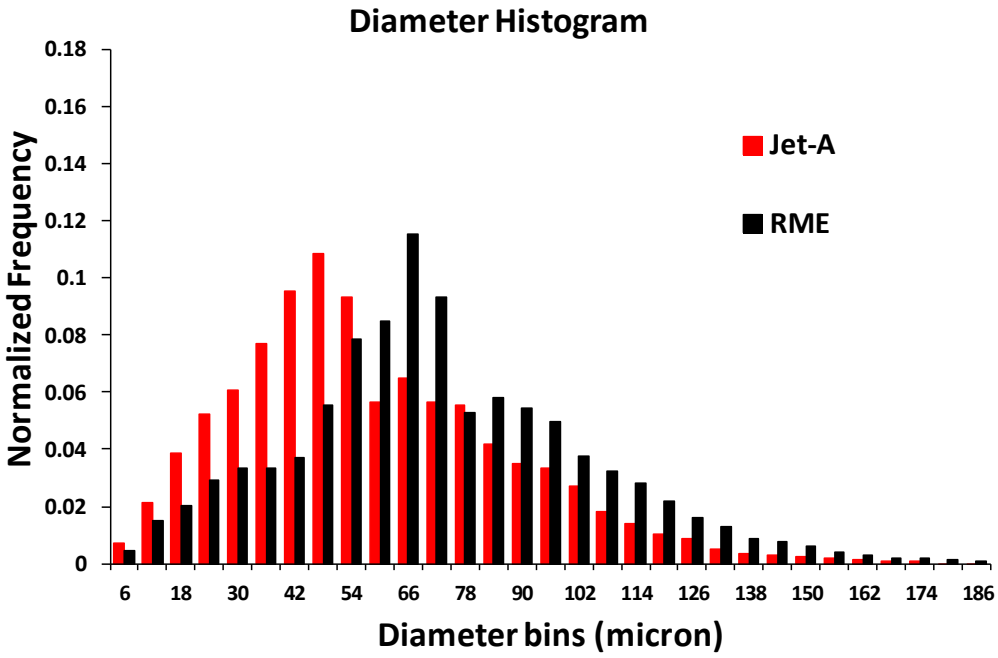

b)

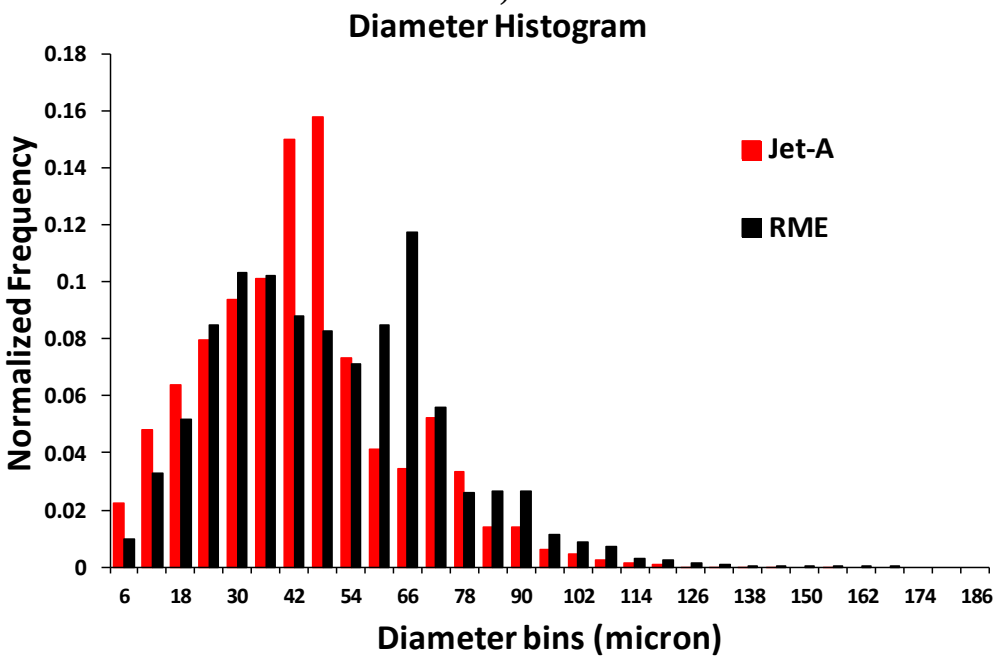

Figure 53: Droplet diameter histogram in the primary zone of interest (from plane z=28cm to z=30cm): a) Baseline test with spray cone angle of 90° and injection velocity of 3 m/s, b) spray cone angle of 130° and injection velocity of 5 m/s

6.5 Crossflow Injection in Cylindrical Pre-mixer with Collision Modeling

In this section, another typical injection method is tested, crossflow injection. Different than co-flow injections, the liquid fuel is injected at an angle with respect to the air-flow direction for crossflow injections. Crossflow injection has shown better vaporization performance from the previous chapter due to higher relative velocity between the droplet and the air which will promote a higher vaporization rate. However, the droplet collision effects on the overall vaporization performance were not considered from previous chapter. With the improved collision modeling [Schmidt and Rutland (2000)] implemented, crossflow injection was simulated for both fuels and results are discussed in details in this section.

6.5.1 Computational Setup

In order to apply NTC/DSCC collision algorithm for a crossflow configuration, the grid strategy used for simple downward spray and co-flow spray would be different since crossflow spray is not axisymmetric around its injection port. However, to avoid numerical complexity, a polar mesh for crossflow can still be used. The difference is that the polar collision mesh for crossflow spray won't be dynamically enveloping the flow based on the maximum axial and radial extent of the spray; instead, the mesh is static in the sense of fixing the number of collision cells, but the polar collision mesh is still randomly rotated at an angel between 0 to 2π around its axis. This grid strategy is very reasonable for a spray within a continuous flow with open boundaries. Although the collision rate may not be accurately predicted before the spray is established in the domain, this initial stage can be ignored by running the simulation longer. Thus, the total run-time is adjusted long enough to ensure good numerical consistency comparing to co-flow

configuration. The number of collision cells is determined based on some preliminary tests. First, a baseline test with an estimated number of collision cells to see how the spray is dispersed in space by recording the number of cells which at least contain one pair of parcels was conducted. This allowed one to calculate the average number of parcels per cell for the baseline test. After some tests, it was established a fixed number of collision cells such that the average number of parcels per cell is around 6, which is consistent with co-flow simulations.

In order to compare the vaporization performance between co-flow injection and crossflow injection the pre-mixer geometry and all the spray parameters are maintained to be the same, such as air-flow velocity and temperature, the spray cone angle, fuel injection velocity and temperature, and the initial droplet size of the spray. However, at spray cone angle of 130° and 5 m/s injection velocity, it was found that the spray will impact the wall if using 90° crossflow injection as in the previous chapter. Thus, the angle of injection for crossflow configuration is determined by running a series of tests such that the droplets are well-dispersed within the pre-mixer space but not hitting the wall. It was found that an optimum injection angle of 40° is needed based on the current pre-mixer geometry and spray parameters. The schematic of the crossflow injection is illustrated in Figure 54a, and Figure 54b shows the dispersion of the crossflow spray after reaching quasi-steady state in a similar manner as Figure 46 for co-flow sprays.

6.5.2 Results and Analysis

First, a check of the vaporization performance of both jet-A and RME was done by monitoring the fuel vapor mass flow rate at the outlet. Both collision modeling and non-collision modeling results are shown in Figure 55a. With collision model activated, it can be seen that the average value of the vapor mass flow rate for jet-A is around 2.5 g/sec. Since the liquid fuel is injected at a rate of 2.7 g/sec, 2.5 g/sec vapor mass flow rate at the outlet indicates that 92.6% of liquid jet-A fuel has been vaporized when reaching the outlet of the pre-mixer. Meantime, RME's average vapor mass flow rate is around 2.15 g/sec, meaning that 79.6% of liquid RME fuel is vaporized through the pre-mixer. There is an 18% difference in vaporization performance between jet-A and RME, which is expected since jet-A has much higher vapor pressures than RME. As usual, RME was pre-heated to 493K and the vaporization performance is improved to 92%. To see the influence of the droplet collisions on the total vaporization performance the collision model was deactivated during the simulation. Without collision, one can see that jet-A is fully vaporized since its vapor mass flow rate reached a value of 2.7 g/sec at the outlet. Meanwhile, to monitor where jet-A reached total evaporation, results were monitored at several cross-sections of the domain, and found that at z=25cm the fuel vapor mass flow rate already reached 2.7 g/sec. Meanwhile, the fuel vapor mass flow rate for RME reached a value of 2.6 g/sec at the outlet. Comparing with 2.15 g/sec with the collision model, there is a 16.7% difference in vaporization performance for RME. Both fuels show a large difference in vaporization performance for simulations with collision modeling and without collision modeling. Thus, the vaporization modeling in conjunction with collision modeling is necessary in predicting the vaporization performance for current applications.

Next, SMD are calculated and plotted in Figure 55b, where one can clearly see the influence of collisions on the droplet size distribution. Take jet-A for example, without collision modeling, SMD/Do went straight down from 1 to 0.2 along the z-axis; with collision modeling, SMD/Do first went up to 1.2 and then slowly went back to 1.0 along the z-axis. This shows that the inter-droplet collisions have very high influence on the droplet size distributions for crossflow injections.

Similar as co-flow simulations, the average surface temperature and total number of droplets within each zone are plotted along z-axis for crossflow simulations. Results are shown in Figure 56. By comparing Figure 56a with Figure 52a, one can see that the temperature rise for crossflow is faster than co-flow for both fuels. This is probably due to a larger contact area beten the spray and incoming air for crossflow than co-flow near the injection port such that the spray obtained more heat transfer from the hot air to promote the increase of the droplet surface temperature. More interestingly, Figure 13b shows that the SMD variation for crossflow injection is even smaller compared to co-axial flow injection along the z-axis. This tells that the collision rate is higher for crossflow injection than co-axial flow injection, which can be explained as follows: for co-axial flow injection, all the droplets are injected approximately in the same direction as the air flow, such that the relative velocities among droplets in each collision cell are relatively small, which results in a relatively low collision rate since probability of collision is proportional to the relative velocity between colliding droplets; for crossflow injection, the spray is injected transversely into the air with a large spray cone angle, so the chance for droplets within the same

collision cell having larger relative velocities will be higher compared to co-axial flow, which in turn promotes the collision rate. Figure 57 shows the normalized droplet size histogram for crossflow injection in a similar manner as co-flow injection shown in Figure 10. One can see that the crossflow injection has a much larger spread in droplet size distribution compared to co-flow flow, which further confirms crossflow has a higher collision rate which confirms that collisions have a larger impact on the droplet size distribution.

Therefore, for crossflow injections, although the vaporization rate is promoted due to higher relative velocity between the spray and air, the collision rate is also higher which generates larger droplets and then slows down the droplet vaporization process. This is the reason why the crossflow vaporization performance only improved slightly from co-flow for the current configuration of the pre-mixer. For crossflow injection, the unmixedness parameter is also calculated at the outlet of the pre-mixer. The values of unmixedness for jet-A and RME are 0.65 and 0.67, respectively. The unmixedness for crossflow injection is higher than co-axial flow injection, indicating the extent of inhomogeneity of the fuel vapor and air mixture is higher for the crossflow injection. This is expected since the crossflow injection is not axisymmetric and would cause a slight increase in the standard deviation of the fuel vapor concentration at the outlet compared to co-flow injection.

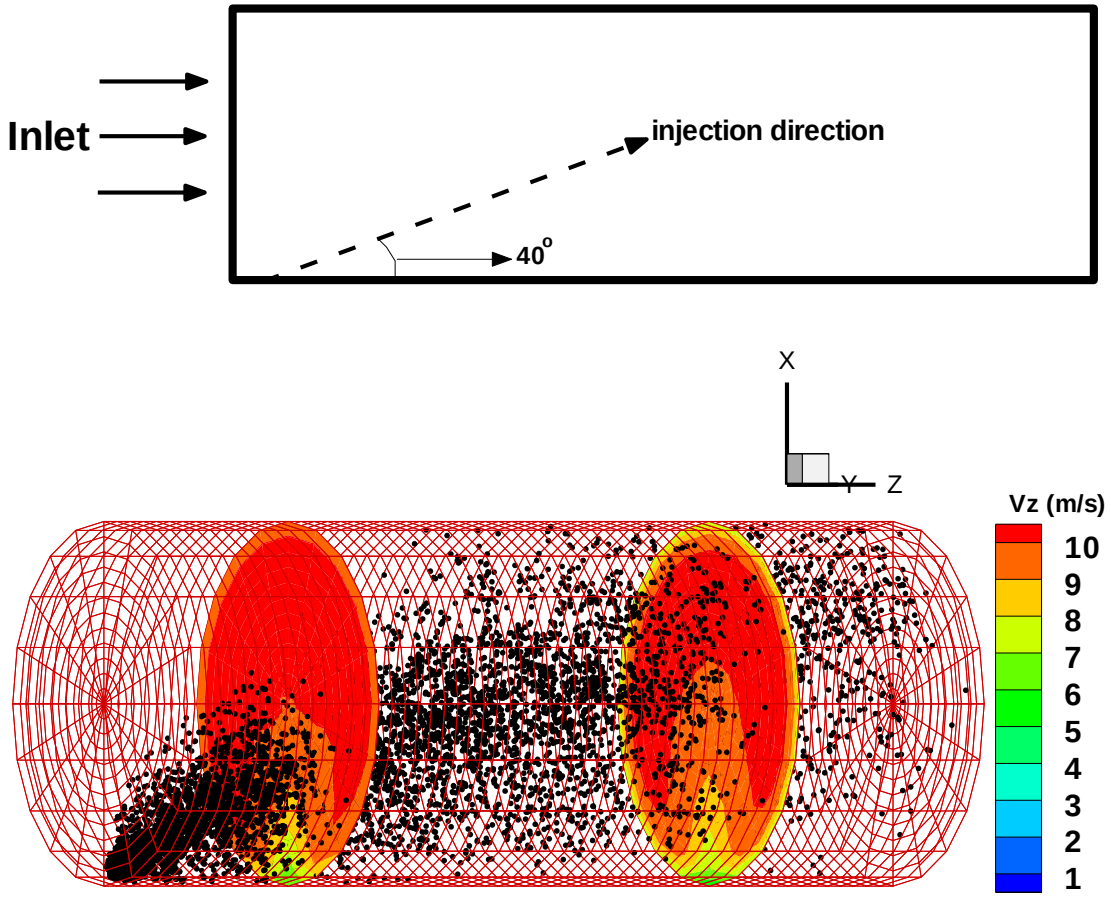

Figure 54: Schematics for oblique crossflow injection and droplets dispersion in the pre-mixer

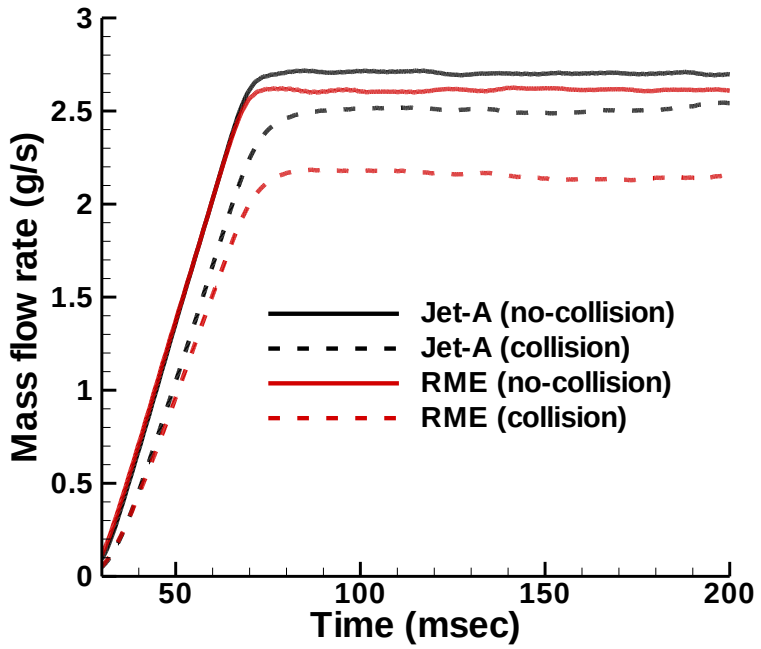

a)

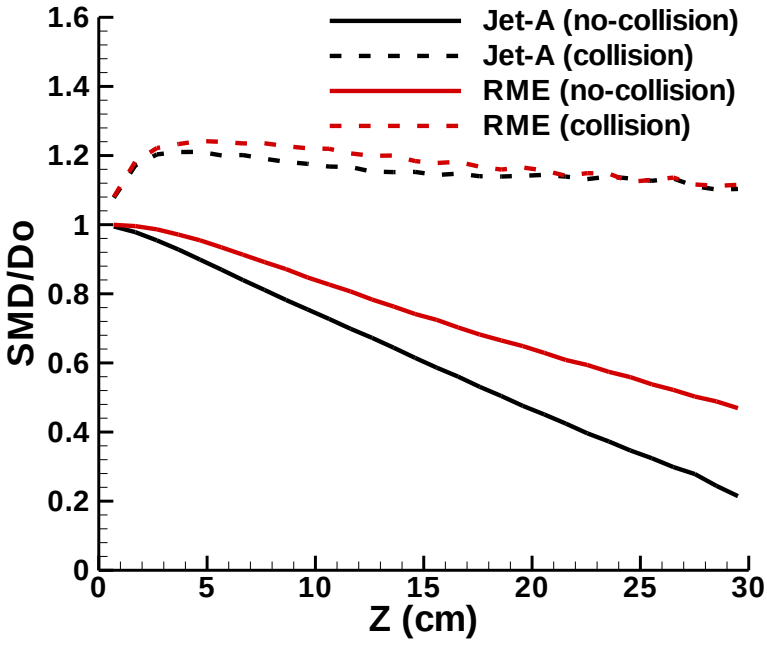

b)

Figure 55: Simulation results of jet-A and RME: a) Fuel vapor mass flow rate at pre-mixer exit b) normalized SMD plotted along z-axis. Comparisions between simulations without collision model and with collision model

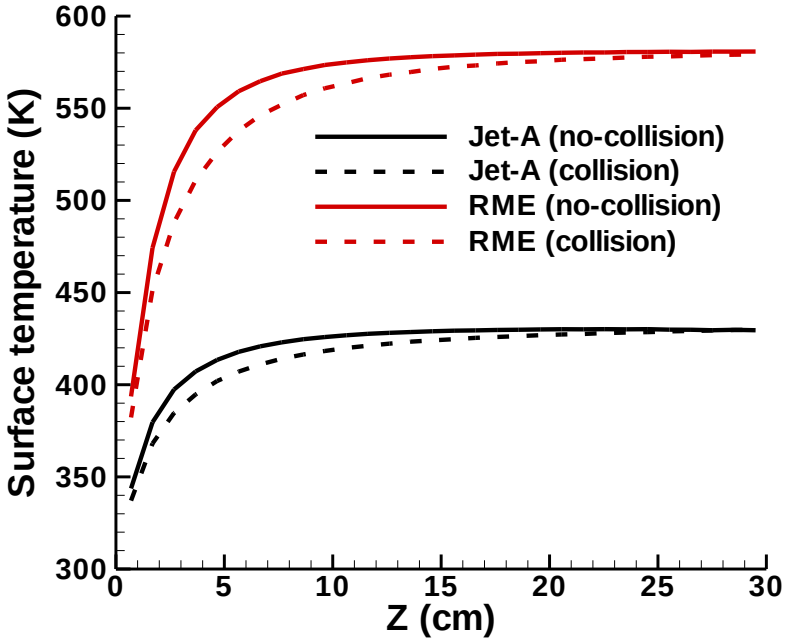

a)

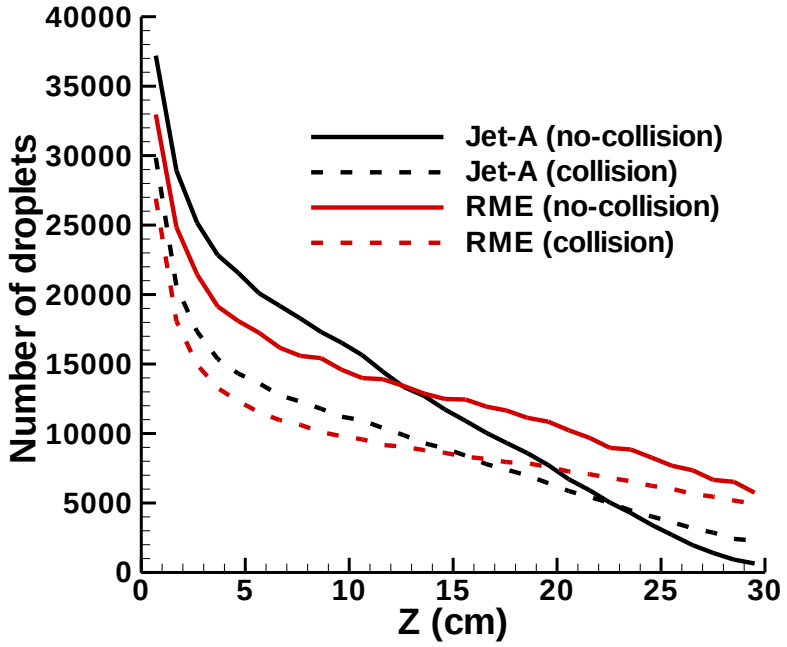

b)

Figure 56: Simulation results of jet-A and RME: a) average surface temperature plotted along z-axis b) number of droplets plotted along z-axis. Comparisions between simulations without collision model and with collision model

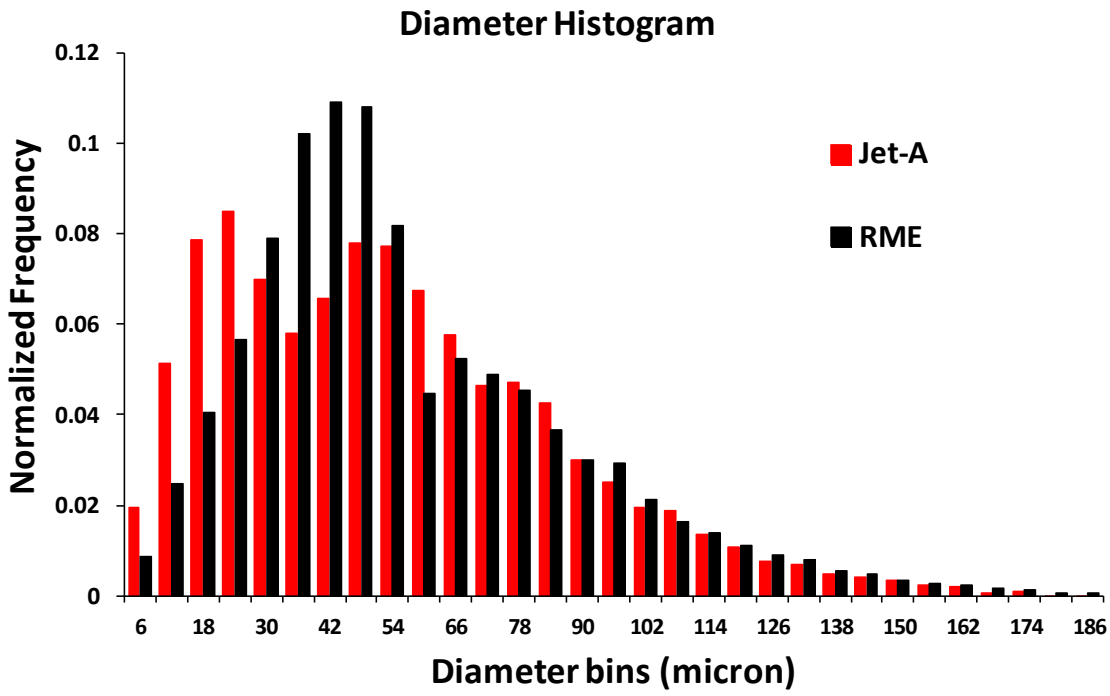

Figure 57: Droplet diameter histogram for oblique crossflow injection in the primary zone of interest (from plane z=28cm to z=30cm).

6.6 Conclusion

In this chapter, the numerical code, KIVA-4, has been used with modified collision algorithm based on the NTC/DSCC method. This improved collision algorithm eliminated the "four-leaf clover" numerical artifacts which could appear when using the original collision algorithm implemented in KIVA-4. For a diesel type injection problem investigated in this paper, the results from the original collision model are found to be grid-dependent, but the modified collision algorithm improves the results significantly.

The collision algorithm was then subsequently used to simulate the spray and vaporization process in a pre-mixer for both jet-A and RME fuels. The liquid fuels are injected into the pre-mixer co-axially with the air flow. SMD results for a mono-dispersed spray with an initial SMD of 80 μm show very good grid independence for a spray cone angle of 90° and injection velocity of 3 m/s. By comparing the fuel vapor mass flow at the outlet to the liquid fuel injection mass flow rate, it was found that 81.5% of jet-A fuel was vaporized through the pre-mixer and 59.3% for RME. The large difference in vaporization performance between jet-A and RME is due to RME's low vapor pressure. In order to improve the vaporization performance, a series of tests were done for several combinations of spray cone angle and injection velocity. Larger spray cone angle and higher injection velocity expectedly showed improvement in dispersion and vaporization performance. The vaporization performance for jet-A and RME at the optimum combination of spray cone angle of 130° and injection velocity of 5 m/s increased to 96.3% and 85.2%, respectively. This major improvement in vaporization performance is also partially due to the relatively smaller average droplet diameter which has a higher vaporization rate. By pre-

heating RME to 493K prior to injection, it was found that the vaporization performance can be further improved to 95%. Comparisons were also made between collision model deactivated and collision model activated. It was found that the vaporization performance decreased due to high droplet coalescence rate induced by collisions for the baseline tests, while the vaporization performance was not affected at the optimum combination of spray cone angle and injection velocity. For all the above tests, the spray dispersion level was also quantified by calculating the maximum radial extent of the spray in each zone along the pre-mixer. Results show that the dispersion level is much higher at larger spray cone angles and injection velocities compared to baseline cases. In order to quantify the homogeneity of the fuel vapor-air mixture, the unmixedness parameter was calculated at the exit of the pre-mixer, which showed that the homogeneity of the fuel-air mixture is significantly improved when the dispersion level of the spray is high.

Next, the crossflow injection of liquid fuels is simulated at the optimum combination of spray cone angle and injection velocity in order to compare the vaporization performance between two injection methods. It wasfound that the fuels needed to be injected at an angle of 40° instead of 90° with respect to streamwise direction to avoid impacting on the wall. The vaporization performance for jet-A and RME are 92.6% and 79.6%, respectively. Compared to co-flow injection performance, crossflow performance is a few percentages lower because of a higher coalescence rate induced by droplet collisions canceling out its higher heat transfer efficiency between two phases for crossflow injections. By pre-heating RME to 493K prior to injection, it was found that the vaporization performance can be improved to 92%.

CHAPTER SEVEN: FUTURE WORK

To accurately predict the pre-vaporization length scale is a crucial part of design process for LPP type of gas turbines that operate on liquid fuels. In present study, different types of liquid fuels injected into hot convective air environment and their subsequent dispersion and vaporization process have been studied under atmosphere pressure. This type of two-phase flow system is very challenging to be simulated since it requires a lot of accurate physical sub-models when a DNS type of simulation is not possible. Therefore, there are still a lot of areas which need to be further explored in order to expand the capability of the current code in solving such problems under various conditions. Hence, the following are proposed to direct the future investigations on continuation of the present studies:

- Since KIVA code has problems to resolve the gas phase flow field fine enough near the nozzle region when injecting small diameter of droplets (that's why the current study uses 80 micron), the inter-phase drag can't be accurately calculated such that the spray processes are under-resolved. As suggested by Abani et al. (2008), applying the gas-entrainment model near the nozzle region provides encouraging results to resolve this issue. It will be worth a try to implement such model in order to simulate fine spray process where the initial injection size is very small.

- As mentioned in Chapter 6, binary droplet collision has several more possible outcomes than currently incorporated in the code (grazing collision and coalescence collision).

For example, shattering collision will happen at high collision Weber numbers, which needs to be incorporated into the collision model to simulate high Weber number spray processes. Thus, more accurate collision outcome model needs to be developed. Post and Abraham (2002) developed a composite collision outcome model based on several existing correlations and mainly focused on diesel spray application where the collision Weber number can be O(1000). Such model is also desirable in our current applications when the droplet collisions have a very large influence on the droplet size distribution and the subsequent vaporization performance. For example, this influence is expected to be much higher for sprays under low convective air temperatures than high convective air temperatures due to the lower influence of vaporization on droplet size. Meantime, the inter-phase drag model also needs to be modified to simulate high speed sprays where the droplet Reynolds numbers are higher than 30.

- The current studies are conducted under atmospheric pressure and 800 K of air temperature, hence additional parametric studies are desirable to see the influence of the elevated environment pressure on the spray vaporization process where the gas turbines are operated.

LIST OF REFERENCES

Abani, N., Kokjohn, S., Park, S.W., Bergin, M., Munnannur, A., Ning, W., Sun, Y., Reitz, R.D., "An improved spray model for reducing numerical parameter dependencies in diesel engine CFD simulations", SAE08-PFL-678 (2008)

Abramzon, B., Sirignano, W.A., "Droplet vaporization model for spray combustion calculations", Int. J. Heat Mass Transfer 12 (9) (1989) 1605–1648.

Amsden, A.A., Ramshaw, J.D., O'Rourke, P.J., and Dukowicz, J.K., "KIVA: A computer program for two- and three-dimensional fluid flows with chemical reactions and fuel sprays", Los Alamos National Laboratory report LA-10245-MS (1985)

Amsden, A.A., O'Rourke, P.J., and Bulter, T.D., "KIVA-II: A computer program for chemically reactive flows with sprays", Los Alamos National Laboratory, LA-11560-MS (1989)

Amsden, A.A., "KIVA-3: A KIVA program with block-structured mesh for complex geometries", Los Alamos National Laboratory, LA-12503-MS (1993)

Amsden, A.A., "KIVA-3V: A block-structured KIVA program for engines with vertical or canted valves", Los Alamos National Laboratory, LA-13313-MS (1997)

Bai, B.F., Zhang, H.B., Liu, L., and Sun, H.J., "Experimental study on turbulent mixing of spray droplets in crossflow", Experimental Thermal and Fluid Science, Vol.33, pp. 1012-1020 (2009)

Barata, J., "Modelling of biofuel droplets dispersion and evaporation", Renewable Energy, Vol. 33, no. 4, pp. 769-779 (2008)

Bellofiore, A., "Experimental and numerical study of liquid jets injected in high-density air crossflow", Ph.D. Thesis, University of Studies of Naples Federico II (2006)

Berlemont, A., Grancher, M.S., Gouebet, G., "Heat and mass transfer coupling between vaporizing droplets and turbulence using a Lagrangian approach", Int. J. Heat Mass Transfer 38 (17) (1995) 3023–3034.

Bianchi, G.M., Minelli, F., Scardovelli, R., Zaleski, S., "3D large scale simulation of the high-speed liquid jet atomization", SAE Tech. Pap (2007-01-0244)

Bracco, F.V., "Modeling of engine sprays", SAE (1985)

Brinckman, K.W., Hosangandi, A., Ahuja, V., Dash, S.M., and Feldman, G.M., "A CFD methodology for liquid jet breakup and vaporization predictions in compressible flows", 46th AIAA Aerospace Sciences Meeting and Exhibit, Reno, Nevada (2008)

Cavaliere, A., Ragucci, R., and Noviello, C., "Bending and Break-up of a Liquid Jet in a High Pressure Airflow", Experimental Thermal and Fluid Science, 27(4), pp. 449-454 (2003)

Chelko L.J., "Penetration of Liquid Jets into a High-Velocity Air Stream", NACA Report RM E50F21 (1950)

Chin, J.S., Freeman, W.G. and Lefebvre, A.H., "Evaporation Histories of Fuel Sprays Injected Across a Flowing Air Stream," Atomisation and Spray Technology, Vol. 2, No. 2, pp. 135-149 (1986)

D*ä*if, A., Bouaziz, M., Chesneau, X., Ch*é*rif, A. Ali , "Comparison of multicomponent fuel droplet vaporization experiments in forced convection with the Sirignano model", Experimental Thermal and Fluid Science 18 (1999) 282–290.

Dagaut, P., Gaïl, S., "Chemical kinetic study of the effect of a biofuel additive on jet-A1 combustion", The journal of physical chemistry. A, Volume 111, Issue 19, p. 3992-4000, 2007.

Deprédurand, V., Castanet, G., and Lemoine, F., "Heat and mass transfer in evaporating droplets in interaction: Influence of the fuel", Int. J. Heat Mass Transfer 53 (17-18) (2010) 3495–3502.

Desjardins, O., Moureau, V., Pitsch, H., "An accurate conservative level set/ghost fluid method for simulating turbulent atomization", Journal of Computational Physics, Volume 227, Issue 18, p. 8395-8416 (2008)

De Villiers, E., Gosman, A.D.,Weller, H.G., "Large eddy simulation of primary diesel spray atomization", SAE Tech. Pap. (2004-01-0100)

Estrade, J.-P., Carentz, H., Lavergne, G., Biscos, Y., "Experimental investigation of dynamic binary collision of ethanol droplets: a model for droplet coalescence and bouncing", International Journal of Heat and Fluid Flow, Volume 20, Issue 5, p. 486-491 (1999)

Faeth, G.M., "Current status of droplet and liquid combustion", Progress in Energy and Combustion Science, Vol.9, pp.293-354 (1977)

Faeth, G.M., "Evaporation and combustion of sprays", Prog. Energy Combust. Sci.9 (1983) 1–76.

Faeth, G.M., "Mixing, transport and combustion in sprays", Prog. Energy Combust. Sci. 13 (1987) 293–345.

Faeth, G.M., "Spray combustion phenomena", in: Twenty-sixth Symposium (international) on Combustion, The Combustion Institute, 1996, pp. 1593–612.

Georjon, T.L., Reitz, R., “A drop-shattering collision model for multidimensional spray computations”, Atomization and Sprays, vol.9, pp.231-254 (1999).

Gorokhovski, M., Herrmann, M., “Modeling Primary Atomization”, Annual Review of Fluid Mechanics, vol. 40, Issue 1, pp.343-366 (2008)

Gu, X., Basu, S., Kumar, R., “Dispersion and vaporization of biofuels and conventional fuels in a crossflow pre-mixer”, Int. J. Heat Mass Transfer vol. 55, Issue 1-3, pp.336-346 (2012)

Hill, J., Nelson, E., Tilman, D., Polasky, S., Tiffany, D., “Environmental, economic, and energetic costs and benefits of biodiesel and ethanol biofuels”, Proceedings of the National Academy of Science, vol. 103, Issue 30, p.11206-11210 (2006)

Hirt, C.W., and Nichols, B.D., "Volume of fluid (VOF) method for the dynamics of free boundaries", Journal of Computational Physics, 39, 201-225 (1981)

Imaoka, R.T., Sirignano, W.A., “Transient vaporization and burning in dense droplet arrays,” Int. J. Heat Mass Transfer 48 (2005) 4354–4366.

Jiang, Y.J., Umemura, A. and Law, C.K., “An experimental investigation on the collision behavior of hydrocarbon droplets”, J. Fluid Mech., vol. 234, (1992). 171-190.

Khosla, S., and Crocker, D.S., “A Boundary Layer Stripping CFD Model for Shear Regime Atomization of Plain Liquid Jets in Cross Flow”, Proc. ILASS-Americas Conference, Arlington, VA, USA (2004)

Law, C.K., “Recent advances in droplet vaporization and combustion”, Prog. Energy Combust. Sci. 8 (1982) 171–201.

Lebas, R., Menard, T., Beau, P.A., Berlemont, A., Demoulin, F.X., “Numerical simulation of primary break-up and atomization: DNS and modeling study”, International Journal of Multiphase Flow, Volume 35, Issue 3, pp. 247-260 (2009)

Leong, M.Y., McDonell, V.G., Samuelsen, G.S., “Mixing of an airblast-atomized fuel spray injected into a crossflow of air”, NASA/CR-2000-210467 (2000)

Linne, M.A., Paciaroni, M., Gord, J. R., Meyer, T.R., “Ballistic imaging of the liquid core for a steady jet in crossflow”, Applied Optics, Vol. 44, Issue 31, pp. 6627-6634 (2005)

Linne, M.A., Paciaroni, Berrocal, E., Sedarsky, D., “Ballistic imaging of liquid breakup processes in dense sprays”, Proceedings of the Combustion Institute Vol. 32, Issue 2, pp. 2147-2161 (2009)

Liu, A. B., Mather D., and Reitz R. D.. “Modeling the Effects of Drop Drag and Breakup on Fuel Sprays”, SAE Technical Paper 930072, SAE (1993)

Madabhushi, R.K., “A Model for Numerical Simulation of Breakup of a Liquid Jet in Crossflow”, Atomization and Sprays, 13(4), pp. 413-424 (2003)

MENARD, T., TANGUY, S., BERLEMONT, A., "Coupling level set/VOF/ghost fluid methods: Validation and application to 3D simulation of the primary break-up of a liquid jet", International journal of multiphase flow, vol. 33, pp. 510-524 (2007)

Miller, R.S., Harstad, K., Bellan, J., “Evaluation of equilibrium and non-equilibrium evaporation models for many-droplet gas-liquid flow simulations,” International Journal of Multiphase Flow 24 (1998) 1025-1055.

Nijdam, J. J., Guo, B., Fletcher, D.F. and Langrish, T. A. G., “Challenges of Simulating Droplet Coalescence within a Spray”, Drying Technology, 22, (2004) 1463-1488.

Ohnesorge, W., “Formation of drops by nozzles and the breakup of liquid jets”, Z. Angew. Math. Mech., Vol. 16, pp. 355-358 (1936)

O'Rourke, P. J., and Amsden A. A., “The TAB Method for Numerical Calculation of Spray Droplet Breakup”, SAE Technical Paper 872089, SAE (1987)

O’Rourke, P.J., “Collective drop effects on vaporizing liquid sprays”, Ph.D. Thesis, Princeton University (1981)

Patterson, M.A., and Reitz, R.D., “Modeling the effects of fuel spray characteristics on diesel engine combustion and emissions”, SAE Paper 980131, Society of Automotive Engineers, Warrendale, PA (1998)

Phillips, J.C. and Miller, P.C.H., “Field and Wind Tunnel Measurements of the Airborne Spray Volume Downwind of Single Flat-Fan Nozzles,” Journal of Agricultural Engineering Research, Vol. 72, No. 2, pp. 161-170 (1999)

Phillips, J.C., Miller, P.C.H., and Thomas, N.H., “Air Flow and Droplet Motions Produced by the Interaction of Flat-Fan Sprays and Cross Flows,” Atomization and Sprays, Vol. 10, No. 1, pp. 83-103 (2000)

Post, S.L., Abraham, J., “Modeling the outcome of drop-drop collisions in diesel sprays”, Int. J. Multiphase Flow 28, 997-1019 (2002)

Powell, C.F., Yue, Y., Poola, R., Wang, J., Lai, M.C., and Schaller, J., “X-ray measurements of high pressure diesel sprays”, SAE Technical Paper 2001-01-0531 (2001)

Qian, J., Law, C.K., “Regimes of coalescence and separation in droplet collision”, J. Fluid Mech., 331, pp. 59-80 (1997).

Rachner, M., Becker, J., Hassa, C., Doerr, T., "Modelling of the Atomization of a Plain Liquid Fuel Jet in Crossflow at Gas Turbine Conditions", Aerospace Science and Technology, 6(7), pp. 495-506 (2002)

Ramotowski, M.J., Klassen, M.S., Eskin, L.D., and Roby, R.J., "Burn biofuels in gas turbines with improved heat rate and natural gas level emissions", PowerGen International, Orlando, FL, Dec 2-4 (2008)

Rayleigh, J.W.S., "On the instability of jets", Proc. Lond. Math. Soc., Vol. 10, No. 4 (1878)

Reitz, R. D., "Modeling atomization process in high-pressure vaporizing sprays", Atomization and Spray Technology, Vol. 3, pp. 309-337 (1987)

Reitz, R. D., and Bracco, F. V., "Mechanism of atomization of a liquid jet", Physics of Fluids, Vol. 25, pp. 1730-1742 (1982)

Reitz, R. D., and Bracco, F. V., "Mechanism of breakup of round liquid jets", The Encyclopedia of Fluid Mechanics, N. Cheremisnoff, Ed., Gulf Publishing, NJ, Vol. 3, Chapter 10, pp. 233-249 (1986)

Reitz, R. D., and Diwakar, R., "Structure of high pressure fuel sprays", SAE Paper 870598 (1987)

Renksizbulut, M., Yuen, M.C., "Numerical study of droplet evaporation in a high temperature stream", J. Heat Transfer 105 (1983) 389–397.

Saha, A., Dubas, B., Kumar, R., Basu, S., "Vaporization characteristics of pure and blended bio-fuel droplets injected into hot stream of air", Proceedings of the 6th U.S. National Combustion Meeting (2009)

Saha, A., Kumar, R., and Basu, S., “Infrared thermography and numerical study of vaporization characteristics of pure and blended bio-fuel droplets”, Int. J. Heat Mass Transfer 53 (19-20) (2010) 3862–3873.

Schmidt, D.P., Rutland, C.J., “Reducing grid dependency in droplet collision modeling”, J. Eng. Gas Turbines Power, Volume 126, Issue 2, (2004) 227-233.

Schmidt, D.P., Rutland, C.J., “A new droplet collision algorithm”, Journal of Computational Physics, Volume 164, Issue 1, pp. 62-80 (2000).

Sedarsky, D., Paciaroni1, M., Berrocal1, E., Petterson, P., Zelina, J., Gord, J., and Linne, M., “Model validation image data for breakup of a liquid jet in crossflow: part I”, Experiments in Fluids (2010)

Sirignano, W.A., “Theory of multi-component fuel droplet vaporization”, Arch Thermodyn. Combust. 9 (2) (1978) 231–247.

Sirignano, W.A., “Fluid Dynamics and Transport of Droplets and Sprays”, Cambridge University press, 1999.

Sirignano, W.A., Wu, G., “Multicomponent-liquid–fuel vaporization with complex configuration,” Int. J. Heat Mass Transfer 51 (2008) 4759–4774.

Sommerfeld, M., Qiu, H.H., “Experimental studies of spray evaporation in turbulent flow,” Int. J. Heat Fluid Flow 19 (1998) 10–22.

Spalding, D.B., “The combustion of liquid fuels”, in: Fourth Symposium (international) on Combustion, Springer, Baltimore, 1953, pp. 847–864.

Subramaniam, S., and O'Rourke, P.J., "Numerical Convergence of the KIVA--3 code and its Implications for Modeling", Los Alamos Unclassified Report LAUR 98-5465 (1998). Savart, F., "Ann. Chim. Phys.", Vol. 53, pp. 337-386 (1833)

Sussman, M., Smereka, P., Osher, S., "A level set approach for computing solutions to incompressible two-phase flow", Journal of Computational Physics, Vol. 114, pp. 146-159 (1994)

Sterling, A.M., and Sleicher, C.A., "The instability of capillary jets", Journal of Fluid Mechanics, Vol. 68, No. 3, pp. 477-495 (1975)

Strakey, P., Talley, D., Fluent News, Fall (2004)

Taylor, G. I., "The Shape and Acceleration of a Drop in a High Speed Air Stream", Technical report, In the Scientic Papers of G. I. Taylor, ed., G. K. Batchelor, 1963.

Tinaut, F.V., "Performance of vegetable derived fuels in diesel engine vehicles", Silniki Spanilowe, No. 2, p. 121 (2005)

Torres, D.J., O'Rourke, P.J., Amsden, A.A., "Efficient multicomponent fuel algorithm," Combustion Theory and Modelling 7 (2003) 67-86.

Torres, D.J., "KIVA-4 manual", Los Alamos National Laboratory (2007)

Tyler, F., "Instability of liquid jets", Philos. Mag. (London), Vol. 16, pp. 504-518 (1933)

Wang, S.C., Lin, A.C., "Internal temperature distributions of droplets vaporizing in high-temperature convective flows," J. Fluid Mech., (1992), Vol. 237, pp. 671-687.

Weber, C., Zum Zerfall eines Flussigkeitsstrahles, Z. Angew. Math. Mech., Vol. 11, pp. 138-245 (1931)

Willams, F.A., “Combustion theory”, 2nd Ed., Addison-Wesley Publishing Co., Reading, MA (1985)